

Measurement of the Diffractive
Proton Structure Function
and Calibration of the
Forward Muon Detector
at H1

Andrew Mehta

December 1994

A thesis submitted to the University of Manchester for the degree of
Doctor of Philosophy in the Department of Physics in the Faculty of
Science.

Contents

1	Electron-proton Scattering at HERA	15
1.1	Introduction	15
1.2	Electron-proton Scattering	15
1.3	Kinematics of Electron-proton Scattering	16
1.4	Structure of the Proton	18
2	The H1 Detector	21
2.1	The HERA Electron Proton Collider	21
2.2	Overview of the H1 Detector	21
2.3	Calorimetry	22
2.4	Tracking	27
2.5	Muon Detectors	29
2.6	Electron Tagger and Photon Detector	29
2.7	Scintillation Detectors	30
2.8	Triggering	30
3	The Forward Muon Detector	33
3.1	The Role of the Forward Muon Detector	33
3.1.1	Muon Identification	33
3.1.2	Proton Remnant Measurements	35
3.2	Spacial Arrangement of the FMD	35

3.3	Operation of the Forward Muon Detector	38
3.4	The Drift Chamber	38
3.4.1	Structure	38
3.4.2	Operation	39
3.4.3	Choice of Gas and Operating Voltages	41
3.5	Reconstruction	42
3.5.1	QT	42
3.5.2	Space Point Reconstruction	43
3.5.3	Muon Track Reconstruction	44
3.5.4	Momentum Measurement	45
3.5.5	Calibration Reconstruction	45
4	Calibration of the Forward Muon Detector	47
4.1	Introduction	47
4.2	Timing Corrections	47
4.2.1	Time of Flight Correction	48
4.2.2	Cable and Wire Corrections	49
4.2.3	Complete Correction	50
4.3	Determination of T_0	50
4.3.1	Time Distribution Method	51
4.3.2	Checksum Method	54
4.3.3	Error Treatment	56
4.4	Results	58
4.5	Calculation of the Drift Velocity	58
4.5.1	Time Distribution Method	58
4.5.2	Checksum Method	59
4.5.3	Error Treatment	59

	5
4.5.4	61
4.6	62
5 Alignment of the Forward Muon Detector	65
5.1	65
5.2	65
5.2.1	66
5.2.2	70
5.3	71
5.4	72
6 Performance of the Forward Muon Detector	75
6.1	75
6.2	75
6.3	77
6.3.1	77
6.3.2	78
7 Diffractive DIS at H1	81
7.1	81
7.2	82
7.3	82
7.4	83
7.5	84
7.6	85
7.7	87
7.7.1	87
7.7.2	89

7.7.3	Direct Models	89
7.8	Monte Carlos	89
8	Selection of DIS Events	91
8.1	Introduction	91
8.2	Event Shape	91
8.3	Reconstruction of x , y and Q^2	92
8.4	Event Selection	93
8.4.1	Detector Cuts	94
8.4.2	Kinematic Cuts	94
9	Selection of Diffractive Events	97
9.1	Introduction	97
9.2	Tagging Diffractive Events Experimentally	98
9.3	Detection of High Rapidity Particles using the Forward Detectors	99
9.3.1	Reconstruction of Signals in the Forward Detectors	101
9.3.2	Determination of Residual Noise	102
9.4	Monte Carlo Comparison	104
9.4.1	Forward Beampipe Region Simulation	104
9.4.2	DIS Models	105
9.4.3	Control Plots	105
9.4.4	Detector Efficiencies	105
9.5	Final Selection	108
10	Measurement of the Diffractive Proton Structure Function	111
10.1	Introduction	111
10.2	Kinematic Variable Reconstruction	112
10.3	Bin Selection	112

10.4 Monte Carlo Selection	117
10.5 Determination of $F_2^D(\beta, x_P, Q^2)$	117
10.5.1 N — Number of Diffractive Candidates	120
10.5.2 N_{BAC} — Non Diffractive Background	120
10.5.3 ACC — Smeared Acceptance	121
10.5.4 PDI — Proton Dissociation Correction	121
10.5.5 BVO — Corrected Bin Volume	121
10.5.6 ε — Trigger Inefficiencies	122
10.5.7 δ — Radiative Corrections	122
10.6 Systematic Errors	122
10.7 The Diffractive Proton Structure Function	125
Summary	133
A Forward Detector Efficiencies	135
A.1 Introduction	135
A.2 Method	135
A.3 Results	137

Abstract

A measurement is presented of the diffractive proton structure function $F_2^D(x, Q^2, x_{\mathcal{P}})$ over the range $0.00024 < x < 0.133$, $8.5 \text{ GeV}^2 < Q^2 < 50 \text{ GeV}^2$ and $0.0003 < x_{\mathcal{P}} < 0.1$, using the H1 detector situated at the HERA electron-proton collider. The measurement was made using data taken in 1993 running for an integrated luminosity of 271 nb^{-1} . The data were selected using a class of deep inelastic scattering events that showed no energy flow in a region of pseudorapidity close to the proton beam direction. The results are consistent with an $x_{\mathcal{P}}$ dependence of $x_{\mathcal{P}}^{-1.11 \pm 0.05 \pm 0.12}$ independent of Q^2 or $\beta = x/x_{\mathcal{P}}$. This result is in good agreement with factorisable diffractive models.

A new method of selecting diffractive events is presented based upon the reconstruction of signals using detectors close to the beam pipe. This method results in a large improvement in the acceptance of diffractive events, compared with the previous method which used information solely from the main calorimeter, and so allows measurements to be made in new kinematic regions.

The forward muon detector is described in detail. Included is a full description of the calibration and alignment of the detector. Results are given for a measurement of the drift velocity, T_0 and spacial resolution of the chambers of the system. A Monte Carlo prediction of the momentum resolution is provided.

No portion of the work referred to in this thesis has been submitted in support of an application for another degree or qualification of this or any other institute of learning.

Copyright in text of this thesis rests with the author. Copies (by any process) either in full, or of extracts, may be made **only** in accordance with instructions given by the author and lodged in the John Rylands University Library of Manchester. Details may be obtained from the librarian. This page must form part of any such copies made. Further copies (by any process) of copies made in accordance with such instructions may not be made without the permission (in writing) of the author.

The ownership of any intellectual property rights which may be described in this thesis is vested in the University of Manchester, subject to any prior agreement to the contrary, and may not be made available for use by third parties without the written permission of the University, which will prescribe the terms and conditions of any such agreement.

Further information on the conditions under which disclosures and exploitation may take place is available from the Head of Department of Physics and Astronomy.

This work was supported financially by the Science and Engineering Research Council (S.E.R.C.), latterly the Particle Physics and Astronomy Research Council (P.P.A.R.C.) between October 1991 and October 1994.

Introduction

The understanding of diffractive processes can be greatly enhanced by making measurements in Deep Inelastic Scattering (DIS). Just as the structure of the proton was determined in earlier DIS experiments so the structure of the pomeron (the mediator of diffractive processes) can now be measured. HERA is the first DIS experiment that reaches the very low Bjorken x needed to produce diffractive events across a wide kinematic range. The proton structure was largely determined by measuring the proton structure function, $F_2^P(x, Q^2)$. Analogously it is expected that a similar understanding of the pomeron structure should be gained by measuring the diffractive proton structure function, $F_2^D(x, Q^2; x_P, t)$. In chapter 10 of this thesis is presented a measurement of a slightly limited form of the full diffractive structure function, namely $F_2^D(x, Q^2, x_P)$. This is the first such measurement ever made. This thesis is primarily concerned with the experimental extraction of the structure function from the data and not with a theoretical interpretation of the results. The few conclusions that are drawn are used to justify the method of extraction. The method of extraction and the results obtained are presented in chapter 10.

The sample of diffractive events used for the structure function measurement were selected using parts of the detector situated close to the beam in the proton (forward) direction. This ‘forward’ selection differs from the one used previously, which used information solely from the main calorimeter [1]. It resulted in an increase in statistics and allowed the structure function measurement to be made over a much greater kinematic range. The utilisation of the forward detectors was far from straight forward. Certain detectors (such as the forward muon detector) were not originally designed for this purpose. New reconstruction techniques were needed and detailed Monte Carlo comparisons were made to ensure that acceptances and backgrounds could be reliably determined. The details of this analysis can be found in chapter 9.

The forward muon detector was used in the structure function measurement as a diffractive event tagger. It can (as its name suggests) also be used to detect and measure the momentum of forward going muons. Described in chapters 3-6

are the details of the measurements made to calibrate the detector for its role as a muon detector. For good momentum reconstruction it was necessary to have spacial resolutions of $\simeq 200 \mu\text{m}$ in the drift chambers of the system. This involved not only understanding the factors that affected the resolution of an individual drift cell (described in chapter 4), but also required a procedure to align the separate layers of drift chambers with respect to each other (described in chapter 5). The spacial resolutions achieved with the calibration procedure and the effects of misalignments on the momentum resolution are given in chapter 6.

Other topics included in this thesis are: an overview of electron-proton scattering at HERA in chapter 1; a description of the H1 detector in chapter 2; an outline of diffractive DIS physics in chapter 7 and the method of DIS event selection at H1 in chapter 8.

Chapter 1

Electron-proton Scattering at HERA

1.1 Introduction

One of the primary purposes of the HERA electron-proton collider is to extend the existing measurements of the structure of the proton. The electron is (up to the precision experiments will allow) a point like particle whilst the proton is composite. Thus in an electron-proton scattering experiment it is only the proton that breaks up. The electron is, therefore, a very ‘clean’ probe with which to measure the proton’s structure. HERA is a colliding beam experiment, which is in marked contrast to all other electron-proton scattering experiments in which the proton is at rest (fixed target). This enables HERA to reach a centre of mass energy a factor of 10 higher than previously possible, allowing measurements to be made in unexplored kinematic domains.

This chapter gives a brief overview of electron-proton scattering and how the structure of the proton is measured at HERA. For a more comprehensive review of HERA physics see [2].

1.2 Electron-proton Scattering

The dominant reaction in electron-proton scattering is neutral current (NC) scattering:

$$e^- + p \rightarrow e^- + X \tag{1.1}$$

where X is a mainly hadronic system. The reaction is mediated by a virtual photon (or sometimes by a Z^0) and so can be interpreted as photon-proton scattering:

$$\gamma^* + p \rightarrow X \quad (1.2)$$

with the electron as a virtual photon source.

The other reaction allowed within the standard model of particle interactions is charged current (CC) scattering:

$$e^- + p \rightarrow \nu_e + X \quad (1.3)$$

In this case a charged W^- boson is exchanged rather than a photon. Such events have been sighted at HERA [3] and show results in agreement with the electroweak model.

Other processes might be seen at HERA such as the lepton flavour changing neutral current reaction:

$$e^- + p \rightarrow \mu^- + X, \quad (1.4)$$

for which lepton number is violated or heavy lepton production:

$$e^- + p \rightarrow e^{*-} + X, \quad (1.5)$$

which results in a particle with the quantum numbers of the electron but an increased mass. Such processes cannot be explained within the standard model and have not yet been observed.

1.3 Kinematics of Electron-proton Scattering

Figure 1.1 shows a diagram of an example NC event¹. Momentum and energy conservation require the condition:

$$p + k = p' + k' \quad (1.6)$$

so by knowledge of the 4-vectors of the incoming particles and the scattered electron that of the hadronic final state is completely determined. The kinematics of the reaction can be fully described by the square of the centre of mass energy:

$$s = 2p \cdot k \quad (1.7)$$

¹The results of this section can readily be generalised to include CC scattering by replacing the scattered electron 4-momentum (k') with that of the neutrino. Non standard model reactions can be treated similarly.

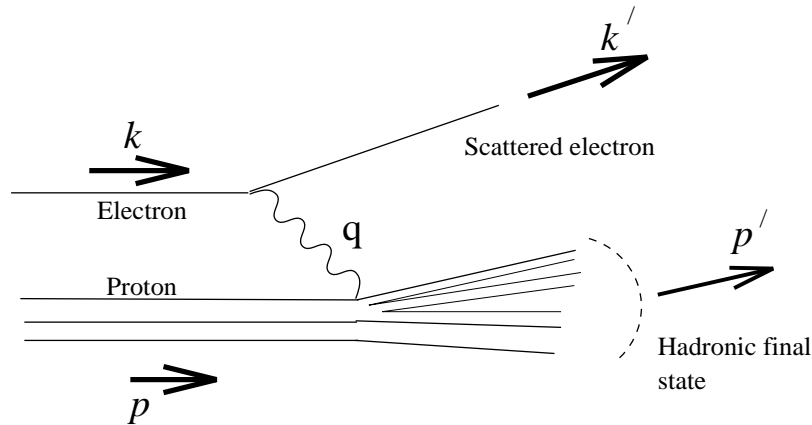


Figure 1.1: The 4-vectors used to define the kinematic quantities.

and the two Lorentz invariant variables:

$$Q^2 = -(k - k')^2 \quad (1.8)$$

and

$$x = \frac{Q^2}{2p \cdot (k - k')} \quad (1.9)$$

Q^2 is the virtuality of the virtual photon. It can be viewed as a measure of the spacial resolving power of the interaction. The greater Q^2 the smaller the structure within the proton that can be measured. x is the Bjorken scaling variable. It is the fraction of the proton's momentum carried by the object struck by the virtual photon [4].

Other useful quantities are:

$$y = \frac{2p \cdot (k - k')}{s} = \frac{Q^2}{sx}, \quad (1.10)$$

and

$$W^2 = p'^2 \quad (1.11)$$

the invariant mass of the hadronic final state

The kinematics of the reaction are complicated, however, if there is electromagnetic radiation from the initial state particles or the final state electron. In this case the relationship of equation 1.6 no longer holds and the kinematic variables depend on whether they are reconstructed from the hadrons or scattered electron. A detailed study of the effects of radiation on the measurements made at HERA is given in [5].

Electron-proton scattering data is usually divided into two classes of events: photoproduction (γp) and Deep Inelastic Scattering (DIS). γp are those events with very small Q^2 ($\ll 1 \text{ GeV}^2$) i.e. the exchanged photon is almost on mass shell. DIS covers the region of high Q^2 (typically $Q^2 > 1 \text{ GeV}^2$). The reason for the distinction is that only when Q^2 is large (i.e. in the DIS region) can the interaction be treated using perturbative Quantum ChromoDynamics (pQCD). Many of the results of γp can be understood only with non perturbative and phenomenological models.

1.4 Structure of the Proton

The virtual photon in electron-proton scattering generally interacts not with the proton as a whole but with a constituent (called a parton). Thus by measuring the cross section as a function of the kinematic variables and investigating the properties of the hadronic final state (X) a detailed survey of the partons within the proton can be made. Electron-proton scattering is different to the other reactions such as proton-proton scattering in which it is usual for both protons to fragment making isolation of the nature of the interaction difficult.

HERA, having a much larger centre of mass energy than previous fixed target electron-proton experiments, allows the survey of the proton to extend into unexplored kinematic regions. Q^2 can reach values a factor of 100 greater, meaning processes that occur at rates a factor of 10 faster in the proton can be resolved. x can reach values a factor of 100 smaller than previous experiments, so the density of constituents carrying down to 10^{-4} of the proton's momentum can be measured for the first time.

The principal method of determining the structure of the proton is by measurement of the proton structure functions in DIS. These are defined (for neutral current) as:

$$\frac{d^2\sigma}{dx dQ^2} = \frac{4\pi\alpha^2}{xQ^4} \left(\left(1 - y + \frac{y^2}{2}\right) F_2^P - \frac{y^2}{2} F_L^P + \left(y - \frac{y^2}{2}\right) F_3^P \right), \quad (1.12)$$

where the structure functions F_2^P , F_L^P and F_3^P are functions of x and Q^2 . F_2^P is the dominant contribution to the cross section, F_L^P is the contribution due to longitudinally polarised photons and F_3^P due to Z_0 exchange and so only becomes important when Q^2 is close to the Z_0 mass. The variation of the structure functions in x and Q^2 allows the structure of the proton to be determined and also provides a test of pQCD [4]. A measurement of F_2^P has been made at H1 [6] and measurements of the other structure functions should be possible in the future by changing the beam energies and running with positrons [7].

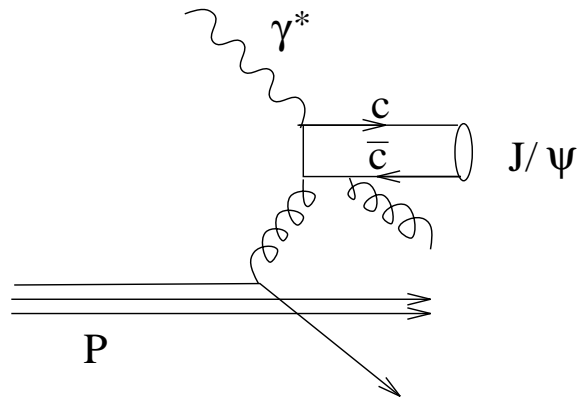


Figure 1.2: Inelastic production of J/ψ mesons via $\gamma - g$ fusion.

Certain measurements of the structure of the proton are also possible in γp . An example of this is the measurement of the gluon density via an analysis of the J/ψ cross section. J/ψ s can be produced by photon-gluon fusion (see figure 1.2). Since there is no corresponding quark induced diagram, identification of this J/ψ production mechanism leads to a clean method to measure the gluon density [8].

Chapter 2

The H1 Detector

2.1 The HERA Electron Proton Collider

HERA (the Hadron Electron Ring Accelerator) is composed of two concentric, near circular, evacuated beam-pipes of 6.3 km circumference. Electrons are accelerated to 26.7 GeV clockwise in one and protons anticlockwise to 820 GeV in the other. The beam-pipes are made to cross at two points on the ring, so that electron and proton beams overlap and collisions may take place. The beams are split into short pulses (called bunches) separated by 28.8 m (or 96 ns between interactions). Some bunches are left empty so that a filled electron or proton bunch might arrive at the interaction point without a colliding partner. These ‘pilot’ bunches are useful for measuring backgrounds due to the collision of an electron or proton with residual gas in the beam-pipe (beam-gas interactions) or with the beam-pipe wall (beam-wall interactions). Two detectors, H1 and ZEUS, have been built around the interaction points.

2.2 Overview of the H1 Detector

The H1 detector is stationed around the northern interaction point of HERA. It is designed to measure the angles, energies and identify particles produced in the interaction with a near 4π solid angle coverage. The main limitation on the angular coverage comes from space taken up by the beam-pipe itself. Points within the detector are described with a right handed Cartesian coordinate system (x, y, z) in which the nominal interaction point defines the origin, z is in the direction of the proton beam and y is vertically upwards. A spherical coordinate system (r, θ, ϕ) is defined in the conventional way with reference to the Cartesian, so that $\theta = 0^\circ$

corresponds to the proton direction and $\theta = 180^\circ$ to that of the electron. The terms ‘forward’ and ‘backward’ refer to the regions of $\theta < 90^\circ$ and $\theta > 90^\circ$ respectively.

To reflect the asymmetric nature of the collisions the H1 detector is in turn very asymmetric. The backward region is almost entirely devoted to identification of the scattered electron, whereas the forward region has a much larger number of detector components to cope with the high density of particles that travel forward in a typical event.

The two main particle detection techniques used at H1 are tracking and calorimetry. A tracking detector aims to reconstruct the paths traversed by any charged particles that passed through the detector. Most of the trackers at H1 are positioned in a magnetic field or else there is a magnetic field between them and the interaction point. Thus by measuring the radius of curvature of the tracks the momentum of the particle that gave rise to the track is determined. Uncharged particles cannot be identified by most of the trackers at H1.

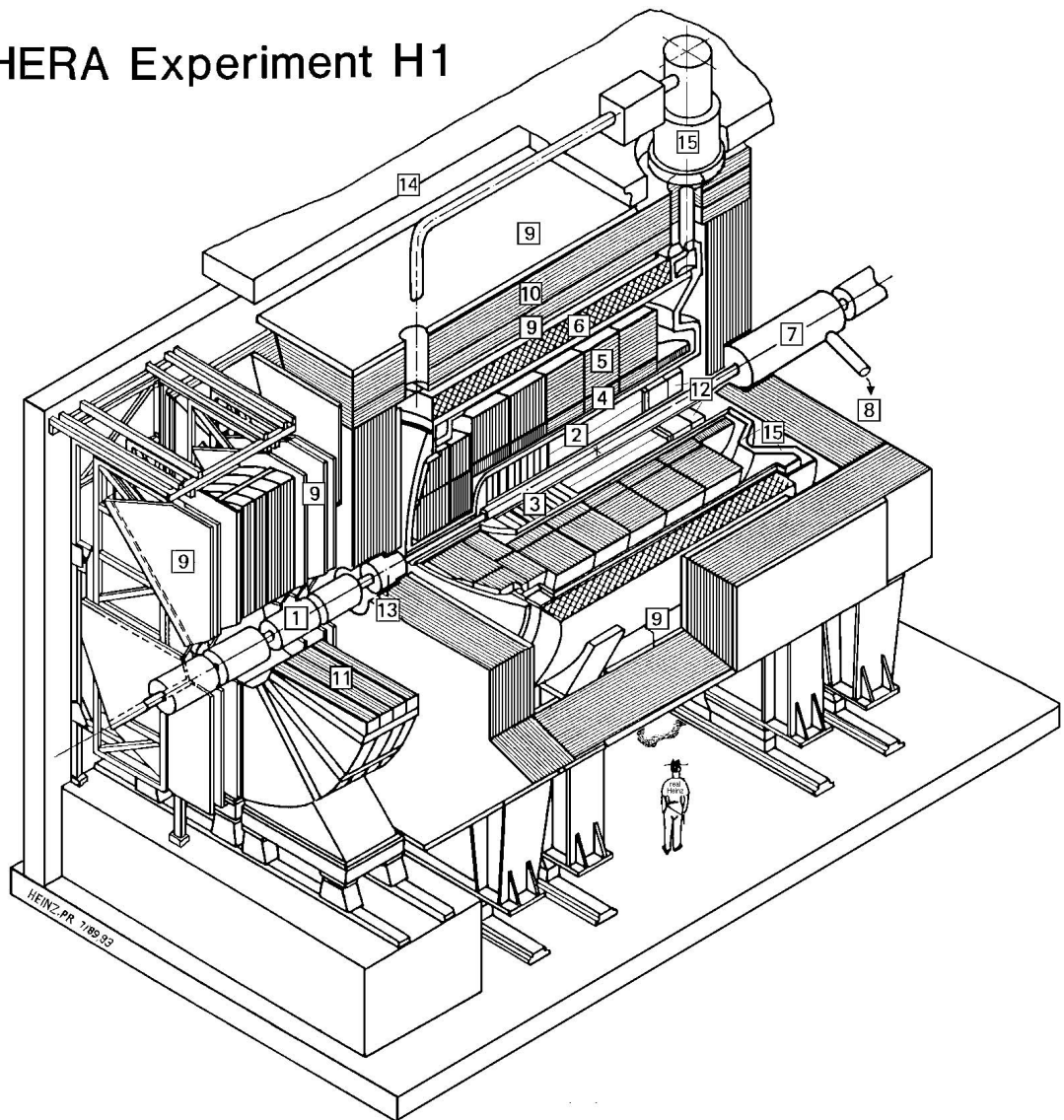
A calorimeter absorbs nearly all incident particles and converts their energy into a measurable signal. The energy resolution is thus very good especially for high energy deposits. The calorimeters are finely segmented but generally not such that individual particles can be resolved. Instead the energy of groups of particles (clusters) or isolated particles (such as the scattered electron in DIS) is found. Calorimeters have the advantages over trackers in that they can detect neutral particles and distinguish between electrons or photons and hadrons.

The H1 detector is pictured in figure 2.1. It consists of a cylindrical arrangement of trackers about the beam-pipe, with an outer layer of calorimeters, surrounded by a solenoid producing a magnetic field of magnitude 1.2 T in the z direction. The detector is enclosed in iron consisting of a barrel and a forward and backward endcap, which acts as the return yoke for the magnetic field. Forward of the iron is a forward muon spectrometer and the proton remnant tagger. Backward of the iron are the electron tagger and photon detector.

2.3 Calorimetry

The H1 calorimeter system is pictured in figure 2.2. It is composed of four physically separate units: the Liquid Argon Calorimeter (LAC); the Backward ElectroMagnetic Calorimeter (BEMC); the plug calorimeter (PLUG); and the tail catcher (TC) situated within the iron return yoke.

HERA Experiment H1



- | | | | |
|---|------------------------------|----|--------------------------------------|
| 1 | Beam pipe and beam magnets | 9 | Forward muon chambers |
| 2 | Central track detector | 10 | Instrumented iron |
| 3 | Forward track detector | 11 | Forward muon toroid magnet |
| 4 | Electromagnetic calorimeter | 12 | Backward electromagnetic calorimeter |
| 5 | Hadronic calorimeter | 13 | Plug calorimeter |
| 6 | Super conducting coil (1.2T) | 14 | Concrete shielding |
| 7 | Compensating magnet | 15 | Liquid argon cryostat |
| 8 | Helium cryogenics | | |

Figure 2.1: The H1 detector. The proton remnant tagger (at $z = 26$ m), the electron tagger (at $z = -33$ m) and the photon detector (at $z = -103$ m) are not included on this diagram.

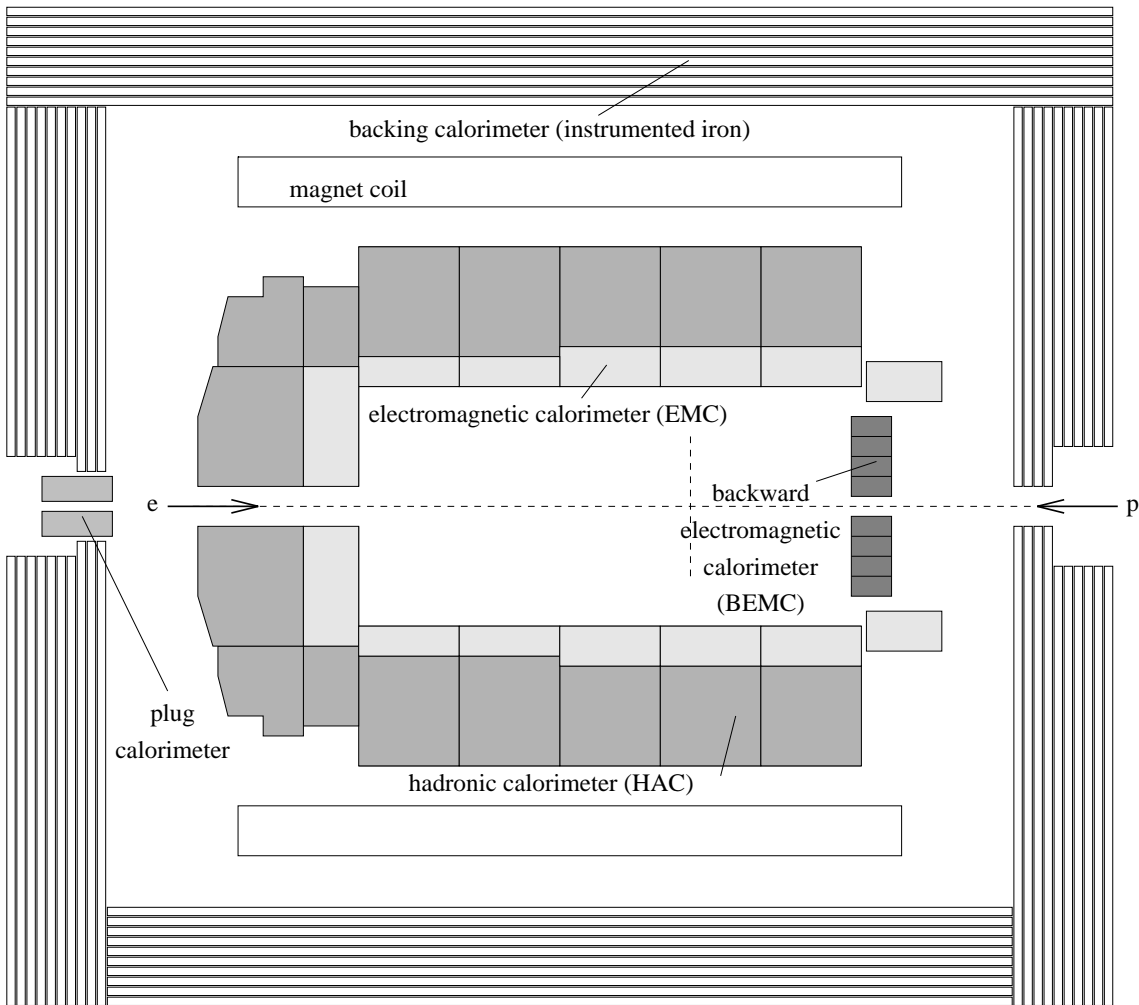


Figure 2.2: The H1 calorimeters.

All the calorimeters at H1 work on the same principle. They are constructed from layers of absorber material with gaps filled with a sampling component. Particles pass into the absorber material, where they undergo multiple collisions with the atoms of the absorber. Electrons and photons interact with the electrons of the atom producing electron-positron pairs and photons by the processes of bremsstrahlung and pair production. Hadrons interact with the nuclei of the atoms of the absorber producing secondary hadrons and nuclear fragments. The secondary particles will interact with further atoms producing yet more particles, until eventually a shower of variously charged particles is produced. In this way all of the energy of the incident particles is lost to the shower. The showering process continues as the particles move into the sampling layer. The material used in the sampling layer is specific to each particular calorimeter, but all have been chosen so as to maximise the conversion of the energy of the shower into an electrical signal that can be passed on to the readout part of the experiment.

LAC is the main calorimeter at H1. Its large solid angle coverage ($0^\circ < \phi < 360^\circ$, $4^\circ < \theta < 153^\circ$) makes it the principal calorimeter used in the detection of the hadronic final state and the scattered electron in high Q^2 events. It is constructed from layers of metal absorber interleaved with an active volume consisting of liquid argon. A high voltage is placed across the gap, with the electrodes divided into rectangles, each having the size of a few cm. The active volume defined by the gap and each rectangular electrode is known as a ‘cell’. Each cell gives an independent energy measurement so the angular energy distribution of an event can be determined.

The energy of the shower is converted into a measurable signal by the ionisation of argon atoms caused by collisions with particles from the shower. The argon ions and liberated electrons move towards the electrodes and produce a signal in the readout system. The number of ionised particles will be proportional to the energy of the shower and so the integrated charge as recorded by the readout system can be converted into the total energy. Liquid argon is chosen over other possible sampling materials because of its high atomic density, thus increasing the number of ions produced, and because the liberated electrons and ions will not interact inelastically with further atoms (since argon is a noble gas), so the observed signal is produced over a small period of time, which is essential for triggering.

LAC is divided into two sections, the electromagnetic inner part (EMC) and outer hadronic part (HAC) to allow separation between electrons or photons and hadrons. EMC has layers of thin (2.4 mm) lead absorber plates, compared to the much thicker (19 mm) steel absorber layers of HAC. The cross sections for the processes of energy loss of incident electrons or photons are much greater than those for the hadrons. This means electrons and photons lose virtually all their energy in the thin layers of EMC, whilst hadrons pass through and are not absorbed until they reach the thick layers of HAC. Thus clusters found in EMC have a good chance of arising from electrons or photons and those in HAC from hadrons.

The energy resolution of LAC has been measured in test beams to be $\sigma_E/E = 0.12/\sqrt{E} \oplus 0.01$ (with E in GeV) for electrons and $\sigma_E/E = 0.50/\sqrt{E} \oplus 0.02$ for pions [9].

The two particle types that are generally not stopped by LAC are muons and neutrinos. LAC can help in muon identification if a track reconstructed in a tracker or muon detector points to a region of the calorimeter where there is little energy deposit, then there is a good chance that the particle was a muon. Neutrinos can only be identified by reconstructing the total transverse momentum of an event, which would be zero if all particles are detected and non zero if a neutrino were

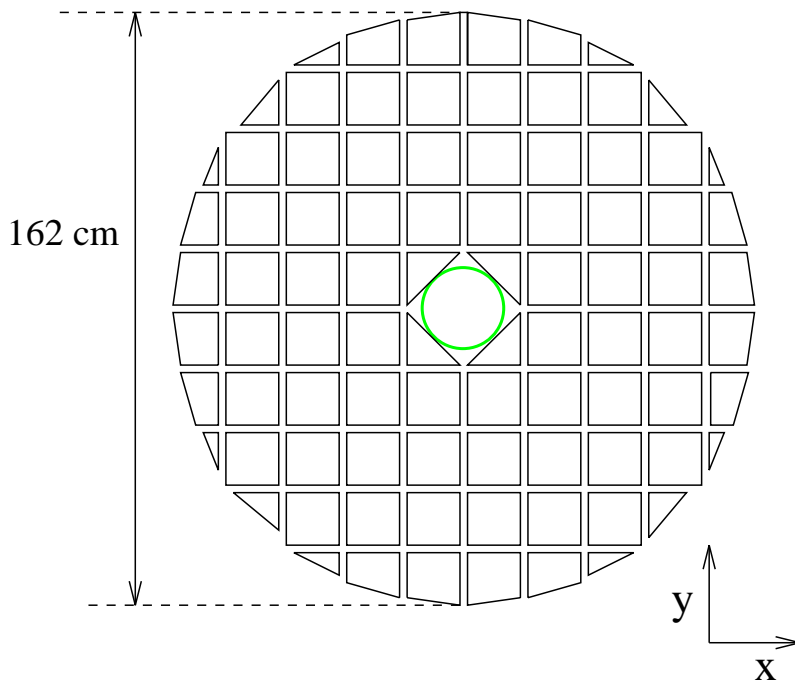


Figure 2.3: Transverse view of the backward electromagnetic calorimeter. The beam-pipe hole is shown in the centre.

present.

BEMC, having an angular coverage of $156^\circ < \theta < 173^\circ$, is the calorimeter used to identify the scattered electron in low Q^2 DIS events. It is relatively transparent to hadrons, with a containment of only about 30 % of hadronic energy. It is composed of 88 stacks, most of which are rectangular ($16 \text{ cm} \times 16 \text{ cm} \times 44 \text{ cm}$) arranged as shown in figure 2.3, with their major axis parallel to the beam-line. Each stack is made up of alternate layers of 2.5 mm lead as the absorber and 4 mm scintillator as the sampler. Wavelength shifter bars run down the long sides of the stacks. Photodiodes are connected to the back ends of the wavelength shifter bars.

BEMC operates by conversion of the energy of the shower, induced in the lead absorber plates, into photons within the scintillator by the process of atomic excitation. The photons are piped to the photodiodes by the wavelength shifters, where they are converted into an electrical signal, which is sent to the readout.

Test beams studies [9] have shown the energy resolution of BEMC for incident electrons to be $\sigma_E/E = 0.10/\sqrt{E} \oplus 0.01$ and the overall scale uncertainty is estimated to be 1.6%.

PLUG covers the region $0.6^\circ < \theta < 3^\circ$. Its principal purpose is to allow mea-

measurements of the hadronic final state at angles more forward than those reached by LAC. It consists of nine alternate layers of 7.5 cm copper absorber and readout boards containing a 400 μm layer of silicon as the sampler. The silicon layer is split into 42 mainly square (5 cm \times 5 cm) sections. The energy resolution is $1.5/\sqrt{E}$ [9].

The iron return yoke is laminated, with the gaps filled with instrumented layers. Part of this instrumentation is used as the tail catcher calorimeter. The purpose of TC is to measure any hadronic energy that escapes LAC or BEMC. This is particularly important in the region of BEMC which has little hadronic capability.

TC uses the iron of the return yoke as absorber material. On the inner and outer sides and within the nine gaps of the iron are positioned 16 layers of Limited Streamer Tube (LST) chambers. Eleven of the layers have calorimetric capabilities with a layer of readout pads of dimensions 30 cm \times 30 cm (in the endcaps) and 50 cm \times 40 cm (in the barrel). The limited streamers induced by the passage of charged particles through the chambers (see section 2.5) give rise to a current in the readout pad. The energy resolution is $\sigma_E/E \simeq 1.0/\sqrt{E}$ [9].

2.4 Tracking

Figure 2.4 shows the inner tracking detectors of the H1 detector. All the trackers are of two basic types: drift chambers and Multi Wire Proportional Chambers (MWPCs). A drift chamber consists of a sealed box filled with gas. One or more sense wires, kept at high positive voltage, run along the interior of the chamber. A region surrounding the sense wire is kept at uniform \mathbf{E} field. This is usually achieved by the placement of cathode wires a few cm away from the sense wires and field shaping wires close to the sense wires, or else by the addition of strips kept at high voltage on the chamber wall. The net result is a region within the chamber of near uniform \mathbf{E} field, except very close (< 1 mm) to the sense wire where the field increases very rapidly.

Charged particles that pass through a drift chamber induce ionisation in the gas along the path of the particle. The liberated electrons ‘drift’ towards the sense wire under the influence of the \mathbf{E} field. On reaching the region of increasing field, the magnitude of the field is such that collisions of the electrons with gas molecules causes secondary ionisation. The electrons released take part in further collisions until an avalanche of electrons and ions is formed. The movement of ions away from the sense wire causes an induced current in the sense wire that travels up the wire and is recorded by the readout system.

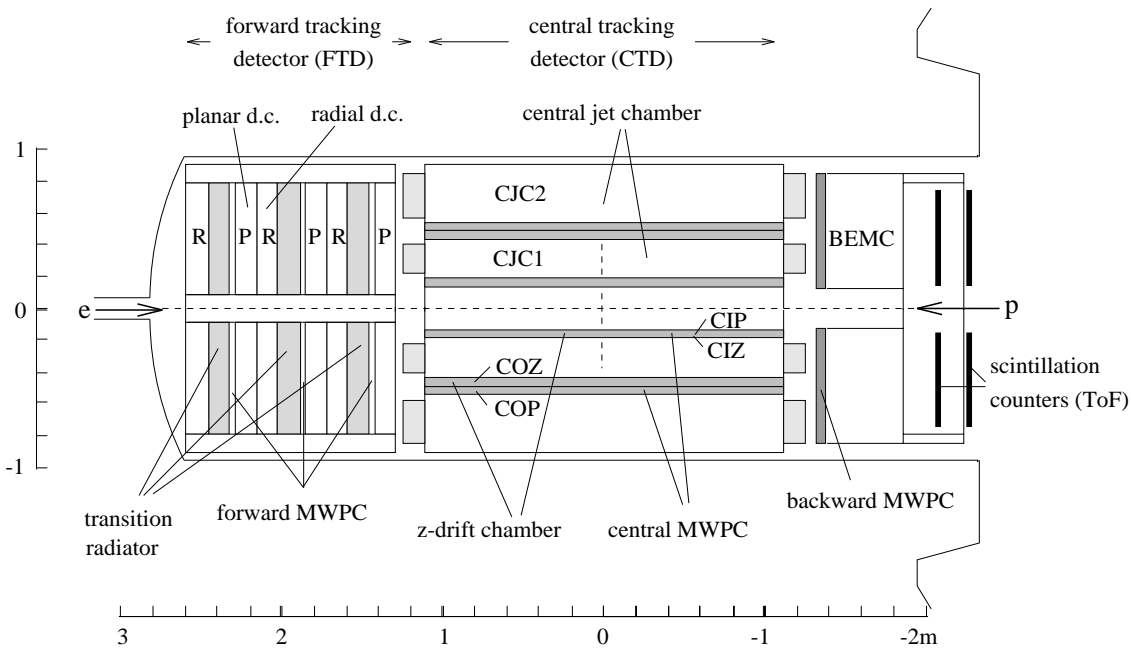


Figure 2.4: The H1 Tracking Detectors.

The time taken for the primary electrons to reach the sense wire is generally a very simple function of the distance they travelled. Hence the distance of closest approach of a particle track and the sense wire (the drift distance) can be determined from the time of the pulse, usually to an accuracy of a few hundred μm . The difference between the signals received at either wire end can be used to find the distance along the wire where the avalanche was induced by the method of charge division (see section 3.5). This measurement is generally only accurate to a few cm. Since the position of the sense wire itself is accurately known (to within $\approx 50 \mu\text{m}$) a three dimensional space point is taken for each wire that a particle passes close to. Thus the path taken by a particle can be reconstructed. The reconstructed path is called a track.

MWPC's work on the same principles as drift chambers, except that they do not contain any drift regions. Instead the wires are placed very close together so that the avalanche regions of adjacent wires overlap. Thus the chamber's resolution is limited by the wire separation (to a few mm). They have the advantage over drift chambers in that the signals can be read out very quickly making them very useful for triggering purposes.

The trackers at H1 are situated in a high magnetic field. The field causes charged particles to move in helical orbits. By measuring the curvature of the track the particle's momentum can be determined.

The H1 trackers are shown in figure 2.4. They are split into three physically separate components: the Forward Tracking Detector (FTD) covering an angular range $7^\circ < \theta < 30^\circ$; the Central Tracking Detector (CTD) ($22^\circ < \theta < 165^\circ$); and the Backward MWPC (BPC) ($155.5^\circ < \theta < 174.5^\circ$). In the overlap regions good track reconstruction is generally only possible if links between the track segments in the different detectors are made. The major difference between the detectors is in the orientation of the sense wires. In the CTD most wires run parallel to the beam-line, whereas in the FTD and BPC the wires run perpendicular. These orientations maximise the number of sense wires passed by a particle and so increase the number of hits per track.

2.5 Muon Detectors

The bulk of muon detection at H1 is provided by the limited streamer tubes situated within LST chambers of the iron return yoke. The LSTs are rectangular boxes of $1\text{ cm} \times 1\text{ cm}$ of varying length. A single wire runs along the centre of each tube. Three sides of the tube are made from a composite material with a low surface resistivity, onto which the high voltage is placed. The fourth side has a high surface resistivity. The wire is earthed. The \mathbf{E} field in the tube is of a magnitude such that an avalanche (or streamer) is produced across the whole cross section of the tube when a charged particle passes through. The high resistive plate stores charge and so prevents a complete breakdown of the cell. To make a measurement in the direction along the wire, long thin metal strips are placed perpendicular to the wires just above the high resistive plate for those chambers not equipped with calorimeter readout pads. The streamer induces a pulse on these strips. The spacial resolution is determined by the spacial size of the limited streamer giving about 4 mm from the LSTs and 15 mm from the strips.

Muon detection is further supplemented by the Forward Muon Detector (FMD). This measures the angles and momenta of muons produced in the forward region. It is described in detail in chapters 3-6.

2.6 Electron Tagger and Photon Detector

The electron tagger (ET) and photon detector (PD) are positioned close to the beam at $z = -33\text{ m}$ and $z = -103\text{ m}$ respectively. Their main purpose is to provide a luminosity measurement by detection of the electron and photon produced in the

bremsstrahlung reaction: $ep \rightarrow ep\gamma$. This reaction has a well known cross section, so along with the knowledge of the acceptance of the detectors (found from Monte Carlo) the luminosity can be measured. The electron tagger is also used to detect the scattered electron in photoproduction events.

The detectors are Čerenkov calorimeters, each made up of an array of rectangular crystals. They have an energy resolution of $\sigma_E/E = 0.1/\sqrt{E} \oplus 0.01$ and spacial resolution of less than 1 mm.

2.7 Scintillation Detectors

Scintillation detectors are placed on the backward side of the H1 detector with the main objective of vetoing proton beam-gas or beam-wall background events. The detectors consist of a plane (perpendicular to the beam) of scintillators situated around the beam-pipe. The Time Of Flight detector (TOF) is situated between BEMC and the backward iron endcap. The inner and outer veto walls are situated outside the iron return yoke at $z = -6.5$ m and $z = -8.1$ m respectively.

The scintillation detectors work on the principle that particles produced from an electron-proton collision will arrive at the scintillator at a different time to background interactions. Particles produced in proton background collisions upstream of H1 will arrive at the scintillator at approximately the same time as the proton bunch passes by. Particles from an electron-proton collision will arrive some time later (at about the time the electron bunch passes by). Upstream background will arrive later still, although of course background events produced near the interaction point cannot be vetoed using timing alone.

The use of the scintillation detectors results in a reduction of about 99 % in the background rate.

A further set of scintillators, the Proton remnant Tagger (PTAG), is placed forward of the rest of H1 at $z = 26$ m to detect particles very close to the proton beam direction.

2.8 Triggering

The purpose of the H1 trigger is to ensure that the data recorded by H1 contains as high a proportion of interesting ‘physics’ events and as low a proportion of non

colliding background events as possible. There are currently three levels to the H1 trigger: L1, L4 and L5.¹ The first two are ‘on line’ i.e. take place within a few ms of the collision and the third is ‘off line’ i.e. takes place after the data have been recorded on tape. The levels are ordered in increasing event reconstruction sophistication but decreasing speed of decision taking, with L1 the having the lowest reconstruction sophistication but taking decisions the fastest. At each level events consistent with no interaction or background are rejected. Thus the data flow is reduced as the trigger level increases.

A trigger element is a flag for a particular event that records whether or not a certain criterion has been fulfilled. This could be for instance energy above a certain threshold in a calorimeter or a hit in an MWPC. By analysis of all trigger elements a decision can be made as to whether the event is consistent with an electron-proton collision, a background interaction, or else no interaction at all. This decision is called an event trigger.

The major problem confronted by the first level trigger (L1) is the shortness in the bunch crossing time (96 ns) since signals from the detector can take an order of magnitude longer to be output. The problem is overcome by storing the information of the last 24 bunch crossings in a procedure known as ‘pipe-lining’. Thus only those trigger elements that can retrieve and process the required information from the detector within about 20 bunch crossings and assign the information to the correct bunch crossing can be used for the L1 trigger. This time limit means that only simple reconstruction tasks can take place. The trigger elements are sent once per bunch crossing to the central trigger. Here all those elements that correspond to the 24th bunch cross before are compared with a predetermined list. If there is any combination that would indicate a collision event then the event has passed the L1 trigger, a signal is sent to every readout channel and the event is read out.

The readout channels cannot input new information from the detector and output past information at the same time. Once an L1 trigger is received the readout channels cease to input new data and start to output the data stored in their buffer. After compression the data are transferred to the first stage of processing, which takes place in a device called the L4 filter farm (FARM). This procedure takes several ms, during which time no new events can be recorded (the experiment is said to be running in ‘dead-time’). Once the data reach the farm the readout channels are enabled and dead-time is over.

The FARM operates asynchronously to the rest of the data acquisition system

¹L2 and L3 are currently not yet available

and so does not contribute dead-time. The events are reconstructed to a very high level (tracks and clusters are found) and any events that are clearly consistent with background are rejected. The data of those saved events is compressed with low level data such as the pulse digitisations discarded. The data is then stored on tape.

At L5 the data is reconstructed, usually a few hours after the collision, with the highest level and most up to date reconstruction code. A final selection of physics event candidates is made and the events stored on the Data Summary Tapes (DSTs). The main purpose of L5 is to reduce the volume of data to a manageable size for physics analysis.

Chapter 3

The Forward Muon Detector

3.1 The Role of the Forward Muon Detector

3.1.1 Muon Identification

The FMD's primary purpose is to provide muon identification, momentum measurement and triggering in the forward region. The usual method of muon identification and measurement — identification of a track within the instrumented iron with a link back to the inner trackers where a momentum measurement is made — is not sufficient in the forward region. The high track density in the forward tracker makes linking difficult. With an added comparison of momentum there is a greater chance that the correct track in the forward tracker will be linked. The requirement of both an instrumented iron track and a forward muon track greatly reduces, especially for triggering, the number of non-muon background tracks due to secondaries from the proton remnant.

Momentum measurement is possible in the range $5 \text{ GeV} < p < 100 \text{ GeV}$, where the lower limit arises from absorption of low energy muons in the FMD toroid or in the material between the interaction point and the FMD and the upper limit from momentum resolution deterioration due to finite spacial point resolution of the chambers and misalignment effects (see chapter 5).

The detector can be used on its own (with an angular range of $4^\circ < \theta < 17^\circ$) or in conjunction with the instrumented iron and forward tracking detector ($7^\circ < \theta < 17^\circ$). A link to the forward tracker is desirable to improve momentum resolution.

In addition to muons produced as a result of a collision (physics muons) there are two other prolific sources of muons: cosmic and beam halo muons. Beam halo

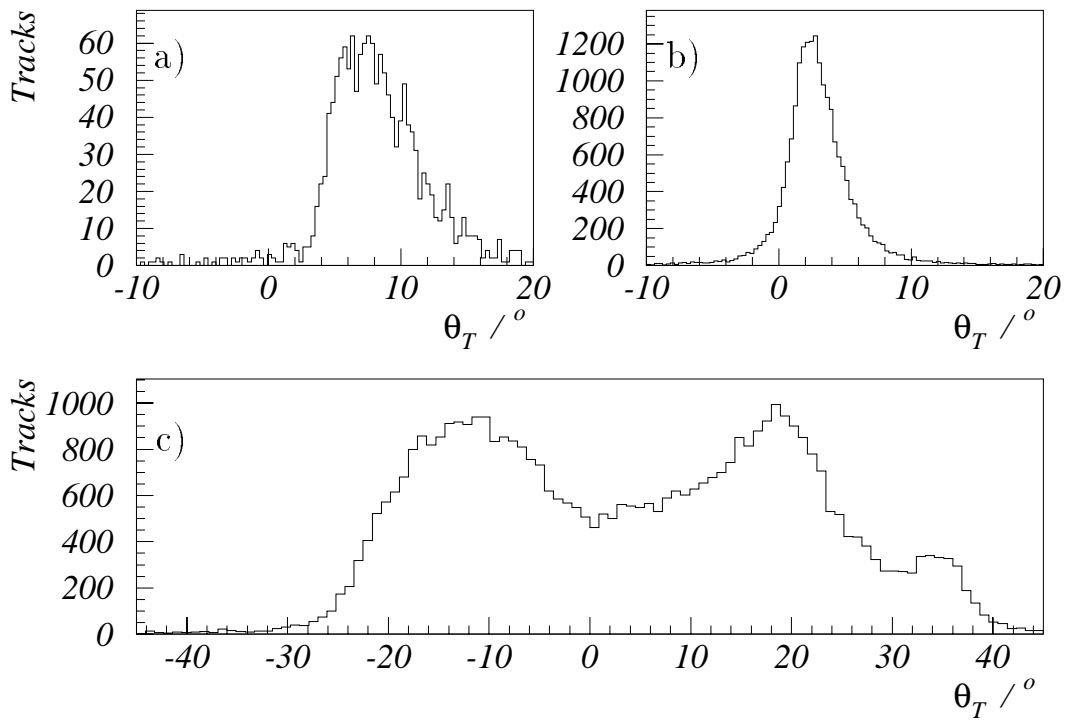


Figure 3.1: The θ_T distributions as determined by the FMD of a) physics muons, b) beam halo muons and c) cosmic muons. θ_T is the radial track angle defined as $\tan \theta_T = (R_2 - R_1)/(Z_2 - Z_1)$, where R_1, R_2 are the distances from the beam line and Z_1, Z_2 are the Z positions at two points along the (straight) track, with $Z_2 > Z_1$.

muons are the result of proton collisions with residual gas in the in the beam pipe or beam pipe wall. They are in time with the proton beam, are typically produced a long way behind the interaction point (Z as low as -40 m) and are at low θ_T ($\simeq 3^\circ$). The rate of electron-gas induced background muons is negligible. The large rate and different angular profiles (see figure 3.1) make cosmic and beam halo muons very useful for calibration and alignment of the FMD.

3.1.2 Proton Remnant Measurements

Particles produced in an e-p collision at very low angles to the direction of the proton beam have a chance of colliding with some ‘dead’ material, such as the beam pipe wall or a collimator, producing a shower of secondaries. These secondaries can have large angles w.r.t. the beam and so can enter the FMD. The average number of hits from secondaries for a typical (DIS) event is $\simeq 30$, with $\simeq 80\%$ of events having at least one hit. Reconstruction of these secondaries provide an effective method to probe the proton remnant and aids tagging of elastic events, where little activity in the forward region is expected. For muon identification, of course, these hits must be treated as background with any muon tracks ‘picked’ out by careful reconstruction. A detailed study of the forward muon detector in proton remnant mode is given in chapter 9.

3.2 Spacial Arrangement of the FMD

The forward muon spectrometer is pictured in figure 3.2. It consists of a toroidal magnet, producing a field of about 1.5 T, with three layers of drift chambers on either side. Each layer is made up of eight octants fixed alternately, to either side of a large aluminium support. A diagram of a complete layer is shown in figure 3.3.

A single octant is made up of an aluminium support sandwiched between two sublayers of drift chambers. The drift chambers in the two sublayers all have parallel wires, but are displaced from each other by a half chamber width, as can be seen in figure 3.6. The chambers are positioned on the octant with wires either perpendicular (for the θ layers) or parallel (for the ϕ layers) to the octant’s axis of symmetry. The naming convention of the layers (i.e. θ or ϕ) arises from the spherical coordinate which, when a vertex is assumed, is most accurately measured by the layer. The θ layers are labelled with Roman numerals: $I \rightarrow IV$, starting at the layer closest to the interaction point. Likewise the ϕ layers are labelled I and II . The θ sublayers are labelled $1 \rightarrow 8$ and the ϕ s $1 \rightarrow 4$, again starting with the sublayer closest to the

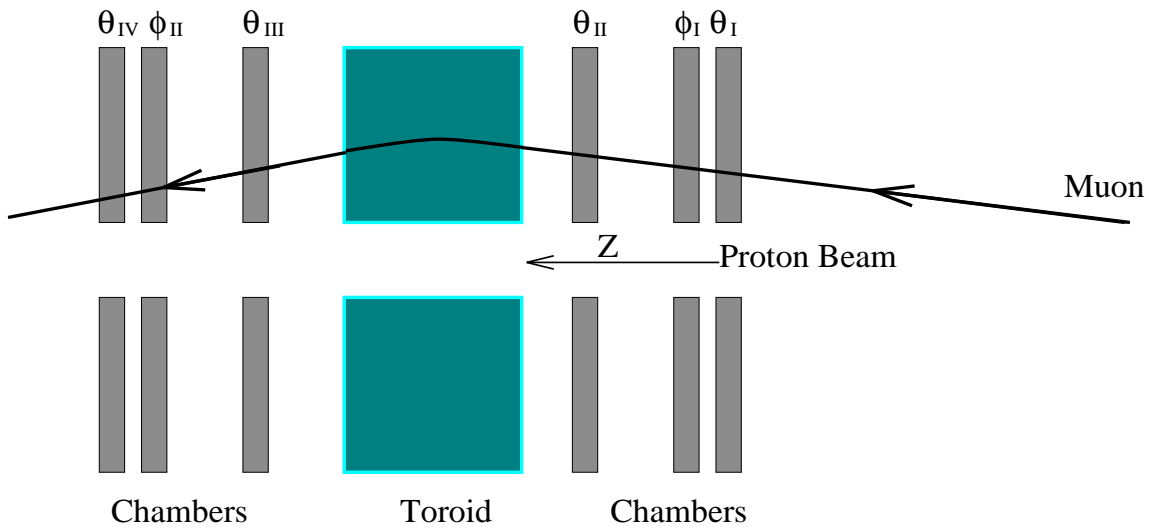


Figure 3.2: Section through the forward muon spectrometer, showing an example muon path.

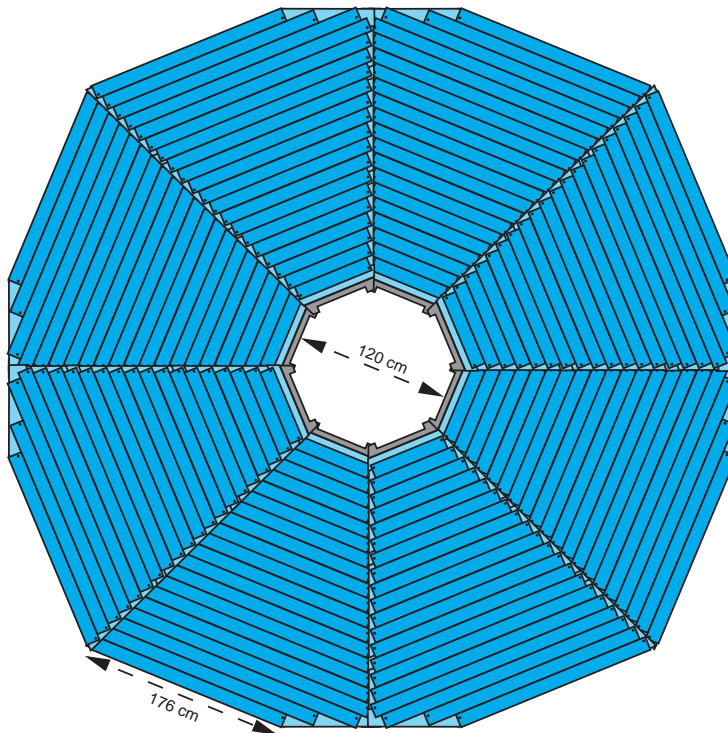


Figure 3.3: A complete theta layer showing all eight octants as viewed from the interaction point.

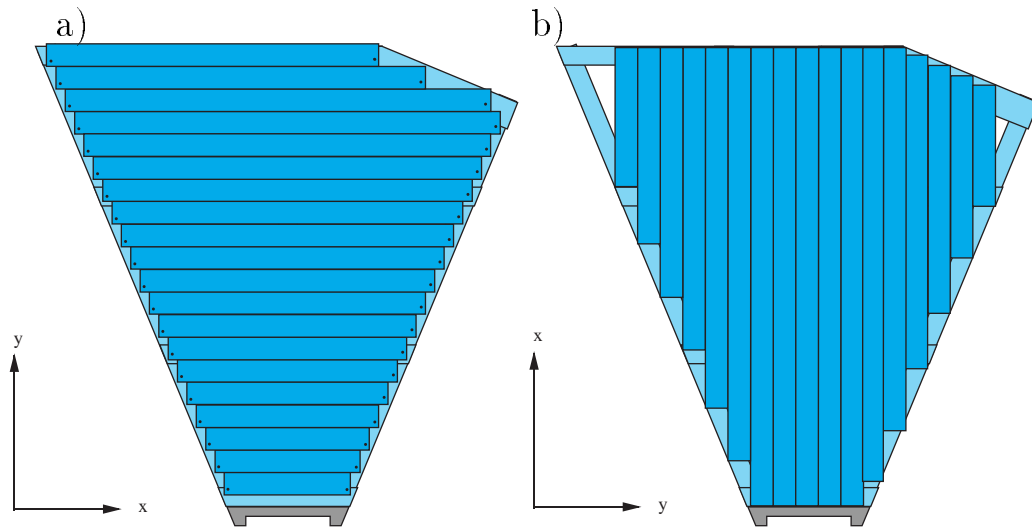


Figure 3.4: A θ octant a) and a ϕ octant b). Note the x coordinate always refers to the direction of the sense wire.

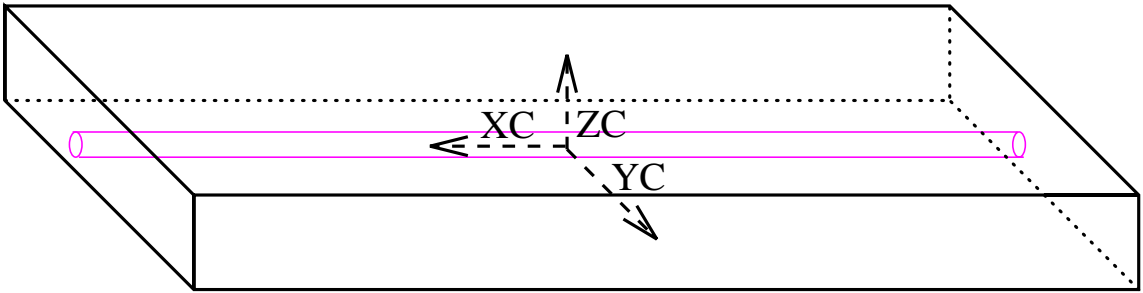


Figure 3.5: A 3 dimensional representation of a cell. The sense wire is shown along the centre. The local cell coordinate system is shown.

interaction point. Unless explicitly stated (usually with a superscript ϕ) it should be assumed that a θ layer or sublayer is referred to.

Besides the H1 coordinate system (see section 2.2) two additional systems are used to describe points within the FMD. The first is octant specific and the second cell specific. The octant coordinate system (X, Y, Z) has its origin (O_X, O_Y) at the beam pipe and O_Z midway between the wires of two sublayers. X always runs in the direction of the sense wires and Y perpendicular as shown in figure 3.4. The cell coordinate system is shown in figure 3.5. The geometric centre of the sense wire is used as the origin. XC is in the direction of the sense wire; YC is in the direction of the aluminium end plate; and ZC in the direction of the drift field strips.

3.3 Operation of the Forward Muon Detector

A muon from the interaction point passes through the first layers of chambers (θ_I , ϕ_I , θ_{II}), is bent in the toroid by an amount:

$$\Delta\theta_T \simeq \frac{0.58}{p}, \quad (3.1)$$

where p is the muon momentum in GeV and $\Delta\theta_T$ is measured in radians, and then through the final layers of chambers (θ_{III} , ϕ_{II} , θ_{IV}). The chambers provide accurate θ and ϕ measurements enabling $\Delta\theta_T$ and hence p to be determined. The main source of measurement error in p comes from multiple scattering off iron atoms in the toroid (estimated to be $\sigma^{ms}(p)/p \simeq 0.22$ [10]), although at high momentum octant misalignments have a comparable effect (see chapter 6).

3.4 The Drift Chamber

3.4.1 Structure

The cells are sealed rectangular boxes, with outer casings of PCB and aluminium. Etched on the inside of the PCB boards are 19 copper strips of uniform width, with the exception of the outer two which are smaller to partially compensate for end effects. A nichrome sense wire runs along the cell's major axis. One end of the sense wire is connected to a pre-amplifier, the other is 'z-linked' to the wire of an adjacent cell with a 330 Ω resistor. In this way there is only one pre-amplifier per cell but both ends of the wire are read out. To reduce over currents (in the shorter cells nearer the beam) whilst keeping a high efficiency (in the longer cells) two sense wire radii of 20 μm (in the short cells) and 25 μm (in the long cells) have been used. Details of the cells and their ordering within an octant and the coordinate labelling scheme is shown figure 3.6.

Voltages are placed on the copper strips, in such a way as to produce as uniform a field as possible, over as great a volume of the cell as possible, directed away from the wire in the YC direction. A high voltage is set on the mid strip, earth on the aluminium casings, with the intervening strips having the voltage $V = V_{centre}(1 - YC/Y_0)$, where Y_0 the distance to the aluminium ($\simeq 6$ cm). The sense wire is kept at a higher voltage than that on the centre pad (typically greater by 1.6 kV), so there is a region of extremely high field surrounding the wire as can be seen in figure 3.7 [15].

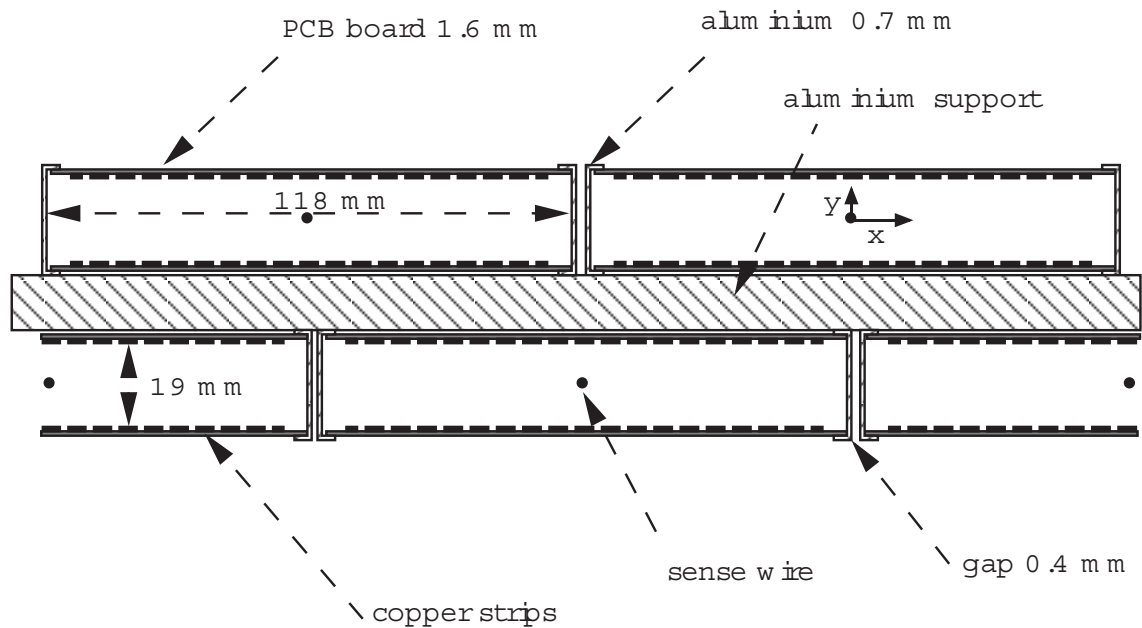


Figure 3.6: Cross-section through an octant, showing individual cells.

The chambers are filled with a carefully chosen gas, which is continually passed through at atmospheric pressure via two plastic tubes situated at each end near the wire.

3.4.2 Operation

As a muon passes through a chamber it causes primary ionisation of a few atoms of the gas by collisions with gas molecules. The electrons and positive ions will ‘drift’ in the ZY plane, in a direction determined by the electric field: the electrons towards the wire; the ions away from it. The charges move at constant velocity, rather than accelerate, because they continually undergo collisions with gas molecules (up to 30 per cm). Near the wire (\simeq few hundred μm) the electrons reach the region of high electric field, where they gain sufficient energy to cause secondary ionisation of the gas molecules with which they collide. These secondary electrons cause tertiary ionisation and so forth, until an ‘avalanche droplet’ containing up to 10^5 electron-ion pairs is formed. The liberated electrons move only a small distance before being absorbed at the sense wire, whereas the ions move up to $\simeq 6$ cm towards the cathode.

The movement of charge within the chamber induces a corresponding current in the sense wire. The primary charges are so few that they produce a negligible current. Only with the onset of avalanching is the beginning of the signal discernible. The electrons from the avalanche droplet account for typically less than 1% of the

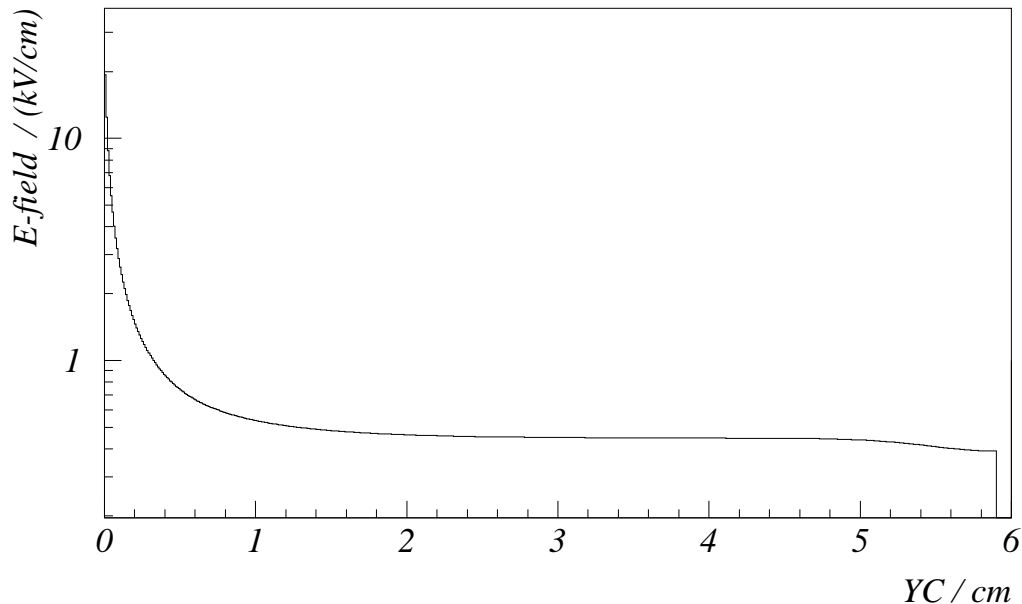


Figure 3.7: The E-field as a function of drift distance for $ZC=0$. The results were obtained using an electrostatic simulation of a cell.

energy of the pulse, the other 99% is accounted for by the movement of the ions since they move through a much greater potential difference. The majority of the pulse energy is developed over the first 50 ns or so, resulting in a sharp pulse with a small rise time.

The signal travels along the sense wire in both directions. One pulse passes through the z-link and down the adjacent wire. Both end up at a wire end, where they pass through a pre-amplifier and finally into an analogue to digital converter (FADC).

The FADC samples the pre-amplifier output once every time bin (9.61 ns). It has a memory of 256 time bins which is linearly shifted and overwritten once per time bin. Only when the FADC receives an external event trigger will the FADC be 'stopped' and its memory be transferred to the front end processors where the first stage of reconstruction (the QT analysis) takes place. Example FADC output is shown in figure 3.8.

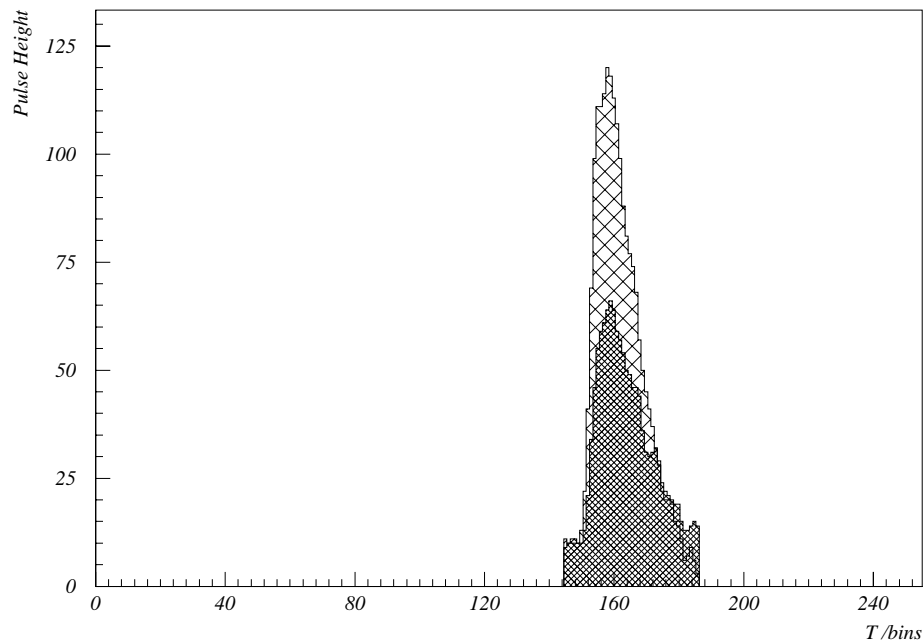


Figure 3.8: A typical FADC signal showing the pulses obtained from each wire end. The pulse height is measured in arbitrary units. $1\text{bin} \equiv 9.61\text{ ns}$.

3.4.3 Choice of Gas and Operating Voltages

The gas used in a drift chamber is typically a two or three component mixture. Its main component is usually a noble gas, since much higher fields are needed to induce ionisation for polyatomic gases which have other means of energy dissipation (rotation and vibration). Small quantities of an electro-negative polyatomic gas are, however, added to provide ‘quenching’. This is the process by which the electro-negative atoms absorb photons, and undergo charge exchange with the noble gas ions, without further ionisation; thus effectively taking energy out of the avalanche, and so limiting it. Without the quenching agent, charge multiplication would increase uncontrollably, eventually leading the cell to permanently discharge and so becoming inoperative. The chosen gas mixture for the FMD is 92.5% Ar —5.0% CO_2 —2.5% CH_4 .

The drift velocity (i.e. the speed with which the primary electrons move) of the gas depends both on its precise mixture and on the E-field and pressure¹. The magnitude of the drift velocity is important since a gas that is too fast gives a

¹Other quantities such as temperature and magnetic field also have smaller effects.

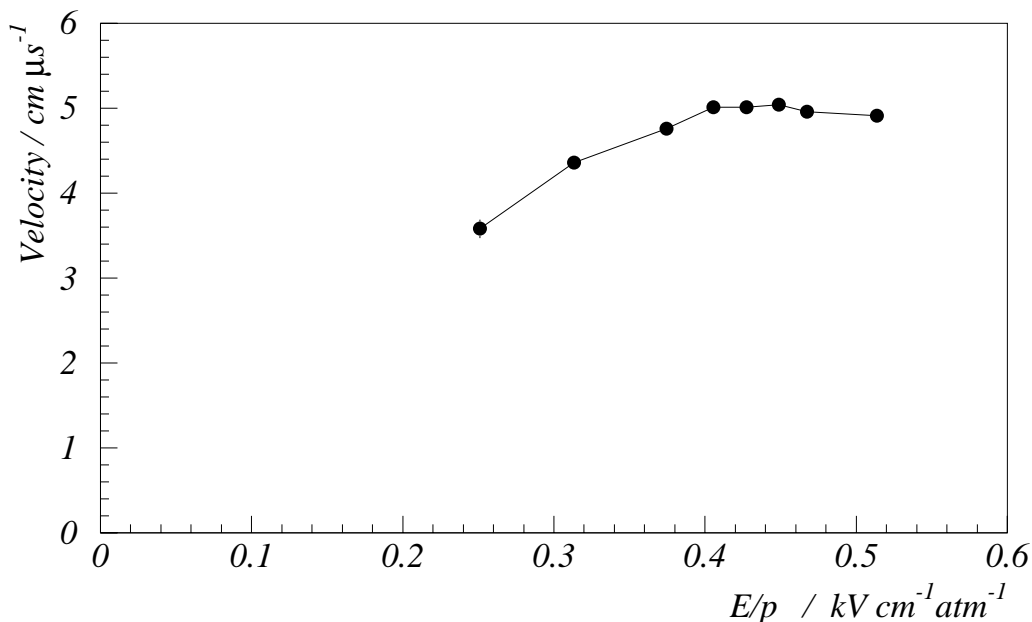


Figure 3.9: Variation of the drift velocity with E-field. The measurements were made using FMD cells in a cosmic test rig.

decrease in distance resolution, whereas one that is too slow will mean pulses with a large drift time will not be fast enough to be used for the trigger. Figure 3.9 (obtained from [11]) shows that for the FMD gas there is a large variation in drift velocity with E-field, but also a region of maximum drift velocity, which is fairly flat (the so called plateau). The drift field across the cell is set to the value at the centre of the plateau (0.45 kV/cm), so slight variations in E-field or pressure will not change the drift velocity greatly.

3.5 Reconstruction

3.5.1 QT

The raw data, consisting of pulses like those of figure 3.8, is translated into a form from which track coordinates can be reconstructed by the QT (charge-time) program. A hit is defined as any signal that rises above a set threshold level and continues above this level for a certain number of time bins. The time of the hit is found by fitting the leading edge of the pulse (for details see [12]). This procedure

enables the resolution on the time to be better by a factor of 2-3 than a bin width. To improve the resolution further an average of the times of the two pulses from each wire end is taken resulting in the quantity T .

A measure of the relative dispersion of the two pulses is found by adding up the charge (in arbitrary units) collected over the first few bins² of the signal from each wire end, with the resulting quantities Q_A and Q_B .

3.5.2 Space Point Reconstruction

As explained in the previous section, the output of QT is in the form of charges and times. The quantities actually required, however, are the XC and YC coordinate of the muon, as it passes through the $ZC = 0$ plane.

The XC coordinate is found by charge division. As the pulses pass along the sense wire they suffer a dispersion proportional to the resistance through which they travel. The larger the distance through which the pulse travels the smaller Q will be. The charge division quantity

$$C = \frac{Q_A - Q_B}{Q_A + Q_B} \quad (3.2)$$

has been shown, using a test set-up [12], to vary linearly with XC , with the constant of proportionality and intercept dependent on the resistance of the sense wires and z-link. The sign of C shows which of the cells of the pair the muon passed through. The resolution on XC is about 2% of the total cell pair length including the z-link, or of the order of a few centimeters. Any hit that has Q_A or Q_B zero (a single ended hit) is not used by the standard reconstruction since no charge division coordinate can be found.

The YC coordinate can be found using the drift time T_{drift} . The time interval between passage of the muon through the cell and the onset of avalanching will, assuming a constant drift velocity, be proportional to the distance travelled by the primary electrons and hence YC , so:

$$YC = v(T_{drift} - T_0) \quad (3.3)$$

where the v (the drift velocity) and T_0 (the tzero) are constant. Determination of these constants and further corrections to drift coordinate determination can be found in chapter 4. Since only the absolute distance from the wire (YC) is known each hit gives rise to two possible Y coordinates at $Y_{wire} \pm YC$. The drift wire

²usually eight, but dependent on the position of the peak in the pulse distribution.

ambiguity must be resolved at later stages of the reconstruction where the hits are associated into pairs or segments.

3.5.3 Muon Track Reconstruction

A muon that completely passes through the detector will produce up to 12 hits that must be linked together to form a track. Muon track reconstruction is a three stage process: the association of hits from both sublayers of a layer to form a ‘pair’; the linking together of pairs from the three layers before (after) the toroid to produce a pre-(post-) toroid segment; and the linking of a pre- and post-toroid segment to produce the complete muon track.

Pairing firstly associates those hits from the first layer with those from the second if the Y separation ($\Delta Y = |Y_2 - Y_1|$ for θ_I) is less than 1.5 cm (corresponding to a limit of 23° in angle). Any remaining hits with ΔY less than 6 cm (60°) are then paired, unless a different pair containing at least one of the hits can be made with a lower ΔY . One further cut is made on accepted pairs that ΔX must be less than 5 times the errors on the two coordinates summed in quadrature. All hits in the system have now been divided into pairs or singles (i.e. all hits that did not form a pair). Pairs and singles are labelled with a θ or ϕ following the naming convention of the layer they are contained in.

A segment is defined as any combination of pairs and singles with the criteria that: each segment may contain only one pair or single from any layer; it must contain either two θ pairs or a θ pair and a θ single; all hits must be contained within the same octant or from an adjacent octant; and it cannot contain hits from both sides of the toroid. A χ^2 per degree of freedom (χ^2/ndf) is now found independently in X and Y . The errors used are 250 μm for each Y coordinate and 1 % of the total wire length for each X coordinate. These are close to the measured resolutions (see section 6.2). All segments with either $\chi_X^2/ndf > 100$ or $\chi_Y^2/ndf > 100$ are rejected. All segments with both $\chi_X^2/ndf < 10$ and $\chi_Y^2/ndf < 10$ are kept. Any other segment is rejected if another exists made up of at least one common hit and has either χ_X^2/ndf or χ_Y^2/ndf less by a factor of 4.

A link between a pre- and post-toroid segment is made if the radial distance difference is < 20 cm and the ϕ difference is $< 30^\circ$, for a straight line extrapolation of the segments to the centre of the toroid. The sample is further cleaned up by performing a momentum scan. A full extrapolation of the pre-toroid segment³

³Unless there are more post- than pre-toroid segments in which case, to save reconstruction

through the toroid is performed with magnetic field bending and multiple scattering errors taken into account. The extrapolation is made using a range of momentum between 2.5 GeV and 200 GeV. The errors on the segment coordinate are fully propagated and a χ^2 representing the probability of a ‘match’ between the two segments of the track found for each momentum. The match is made in X , Y , θ and ϕ . The minimum χ^2 of the scan (χ_{min}^2) is recorded.

Tracks are rejected if: $\chi_{min}^2 > 75$; the momentum scan had no minimum; or there exists another track made from any of the same hits with a lower χ^2 .

3.5.4 Momentum Measurement

Two methods are used to find the momentum of a track. The first is simply to use the momentum that gave χ_{min}^2 . This is the ‘full fit method’. The second method is to perform a new scan, after the event has been identified as containing a muon by the full scan, but to use only a comparison of θ (i.e. information from X , Y and ϕ is ignored) to work out the χ^2 . This is the ‘angle only method’. This method can give better momentum resolutions for a partially misaligned detector (see chapter 6 for further details).

3.5.5 Calibration Reconstruction

A slightly different version of the reconstruction is used for calibration (i.e. cosmic and beam halo) data to ensure that all distributions produced are free from any reconstruction bias. All pairs with $\Delta Y < 9$ cm are kept since cosmic can have much larger angles than physics muons (see figure 3.1). Segments must contain exactly two θ pairs from within the same octant and only the pre- and post-toroid segment with the lowest χ_Y^2/ndf is kept. The only track finding cut is to ensure that the two selected segments lie within the same octant so no momentum scan is needed. One special reconstruction technique is required for cosmic, since they are not in time with the HERA clock and so have an event dependent T_0 . The T_0 is found independently for each segment using the checksum of equation 4.24:

$$T_0 = \frac{1}{2} \left(\frac{W}{v} + T5 + T6 \pm (Y8 + Y7 - Y5 - Y6) \frac{Z_S}{2vZ_L} \right) \quad (3.4)$$

It should be noted that this reconstruction technique has a lower reconstruction efficiency than the standard reconstruction and can only be used when the level of

time, the extrapolation is performed from the post-toroid segments

background tracks is low (which is the case for beam halo and cosmics). It is not suitable for physics muon reconstruction.

Chapter 4

Calibration of the Forward Muon Detector

4.1 Introduction

This chapter explains in detail how T as output by the QT program is converted into the spacial coordinate YC . It is shown how various corrections are made to T on a cell by cell basis, so bringing all times in ‘phase’; how v and T_0 are determined from the data; and how a final correction dependent upon the track angle is made.

4.2 Timing Corrections

A muon produced at the interaction point travels for a time $TF(n)$ before reaching a cell pair, labelled n . The muon causes ionisation of electrons which drift for a time T_{drift} before reaching the sense wire. Two pulses then propagate in opposite directions along the sense wire: the first travels along the wire, through a preamplifier, along a cable and is read out by FADC A. The other travels along the wire, through the z-link, along a second ‘paired’ wire, through a second preamplifier and out along a second cable to FADC B. The times taken for the pulses to travel along the sense wire to their respective FADC are $TC_A(n)$ and $TC_B(n)$. A diagram of the path taken of the signal from cell to FADC is shown in figure 4.1. TC_A and TC_B are a function of the cell pair number (n) since the cables and sense wires vary in length. All FADCs are ‘stopped’, by the event trigger, at the same time after a collision so if the times recorded at the FADCs are T_A and T_B then:

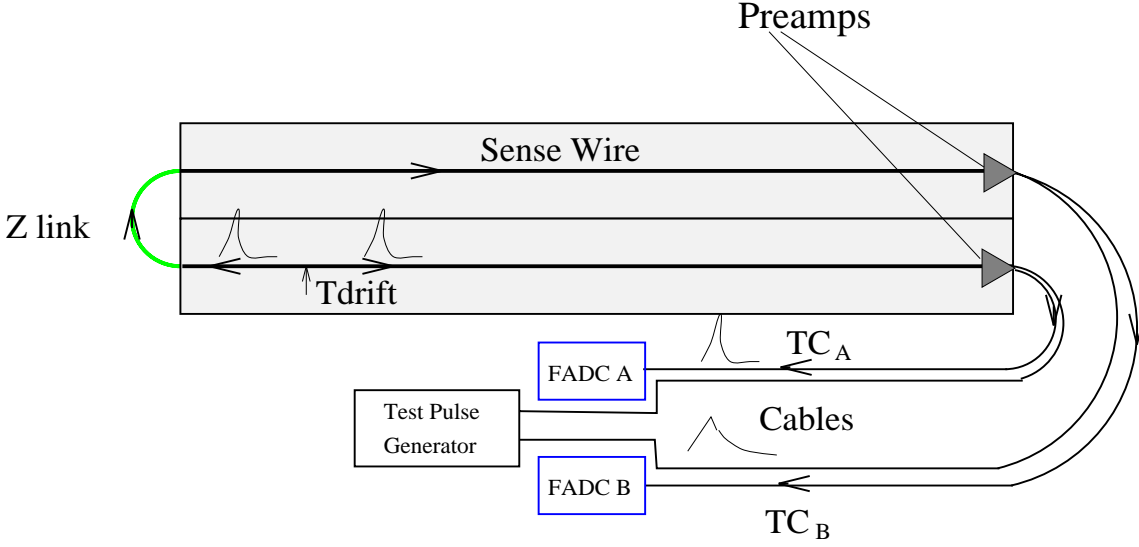


Figure 4.1: Diagram of a cell pair showing the path of the two pulses along the sense wires to the FADC.

$$T_A = TF(n) + Tdrift + TC_A(n) + TZ \quad (4.1)$$

$$T_B = TF(n) + Tdrift + TC_B(n) + TZ, \quad (4.2)$$

where TZ is a constant for all FADCs.

Measurement error on $Tdrift$ is reduced by taking the mean of T_A and T_B giving:

$$T = TF(n) + Tdrift + \frac{1}{2}(TC_A(n) + TC_B(n)) + TZ \quad (4.3)$$

or

$$T = TF(n) + Tdrift + TC(n) + TZ \quad (4.4)$$

setting $TC(n) = (TC_A(n) + TC_B(n))/2$.

To summarise: it is necessary to determine the three quantities of time of flight ($TF(n)$), wire and cable propagation time ($TC(n)$) and the constant TZ in order for the drift time ($Tdrift$) to be determined from the measured pulse time (T).

4.2.1 Time of Flight Correction

The time of flight ($TF(n)$) is simply worked out by taking the distance between the nominal interaction point and the geometric centre of the sense wire of the cell

through which the muon passed and dividing it by the speed of light. Effects such as the of the bending of the muon in magnetic fields, its multiple scattering, the z vertex for the event not being at its nominal value and the muon passing through the cell at a point away from the centre of the sense wire have all been calculated and found to be negligible compared to the resolution of YC .

4.2.2 Cable and Wire Corrections

The wire and cable propagation time ($TC(n)$) is equal to the time taken for a pulse to travel the total distance from FADC A to FADC B via cables, sense wires and z link. A measurement of this quantity was made using a test pulse system which is built into the readout of the FMD. A test pulse generator is connected by wires, which are contained within the same cable as the signal wire, to each sense wire at the pre-amp. A test pulse travels from the generator along the testpulse wire until it reaches the pre-amp, where one signal travels up the signal wire to FADC A and another up the sense wire, through the z-link up the second sense wire, through the second signal wire to FADC B. The time taken from generation to readout of this latter pulse is $TC(n)$.

A test pulse run was taken with conditions set up so that every other test pulse channel in the whole system was pulsed simultaneously i.e. there was exactly one pulse traveling in each wire pair for each event. On the next event the remaining channels were pulsed. After normal QT analysis the time of the later pulse was taken ($Tpulse(n)$).¹

The pulse generator is not precisely in time with the HERA clock but comes with a spread of about 100 ns. Each wire pair is, however, pulsed simultaneously so by taking a difference:

$$Tpulse(n) - Tpulse(0) = TC(n) - TC(0) \quad (4.5)$$

where channel 0 is arbitrarily chosen as the reference channel, the time of pulse generation cancels. To reduce random error many events are taken and a histogram of the L.H.S. of equation 4.5 produced for each cell pair n . Figure 4.2 shows some examples. The histograms are fitted with a Gaussian, the peak position being $TCcor(n)$. Hence

$$TC(n) = TCcor(n) + TC(0) \quad (4.6)$$

The complete list of cable corrections can be found in [14].

¹Since the QT pairs the pulses from the two sense wires and outputs $T = \frac{1}{2} \cdot (T1 + T2)$ and $Td = T1 - T2$ the time of the later pulse is $Tpulse = T + \frac{1}{2}|Td|$.

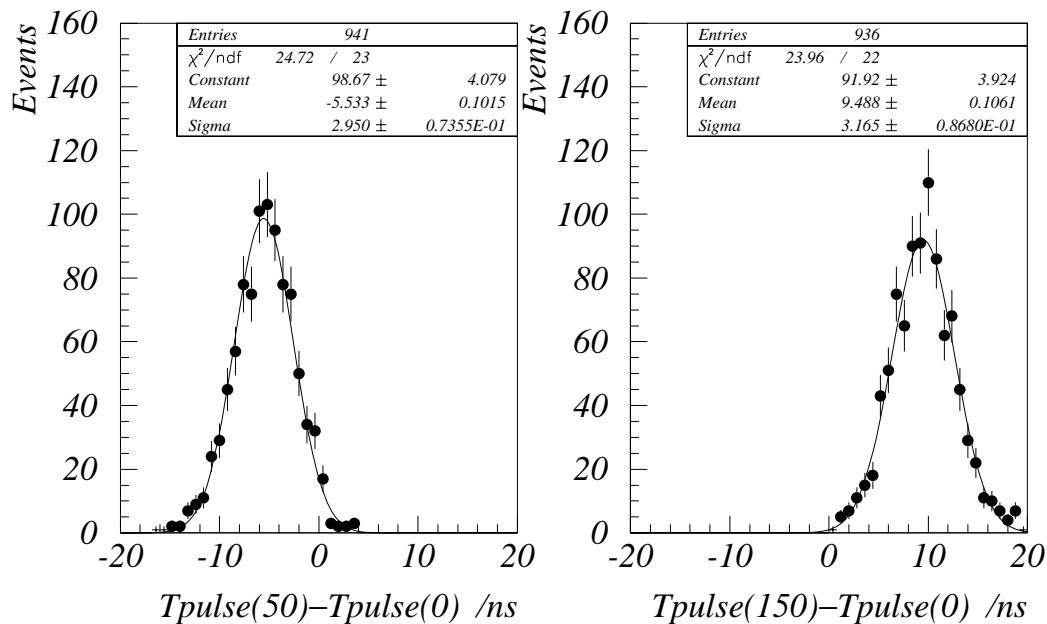


Figure 4.2: The cable corrections for two different cell pairs.

4.2.3 Complete Correction

Equation 4.4 can now be rewritten in terms of the measured or calculated quantities:

$$T_{\text{drift}} = T - TC_{\text{cor}}(n) - TF(n) - TZ - TC(0) \quad (4.7)$$

Combining the constant terms to the single constant T_0 :

$$T_{\text{drift}} = T - TC_{\text{cor}}(n) - TF_{\text{cor}}(n) - T_0 \quad (4.8)$$

and defining the corrected time as $T_{\text{cor}} = T - TC_{\text{cor}}(n) - TF_{\text{cor}}(n)$

$$T_{\text{drift}} = T_{\text{cor}} - T_0 \quad (4.9)$$

T_0 can now be explicitly defined as the corrected time obtained from a muon passing through any cell, very close to the sense wire.

4.3 Determination of T_0

Two methods were used to determine T_0 : the drift time distribution method and the checksum method. Both these methods require a large sample of muons, in time

with the HERA clock, triggered by the H1 central trigger, free from background and at low angles with respect to the beampipe (to limit angular corrections see section 4.6). For these reasons beam halo muons were used. Physics muons were not used due to their small rate and large background contamination. Cosmic muons were not used for being out of time with respect to the HERA clock.

For the data presented here a sample of 60,000 beam halo muons was used. The data were taken during normal e-p collisions, with the toroid field on, for the running period 01:07:94 \rightarrow 17:07:94. To ensure a completely unbiased trigger the forward muon trigger was not used. Instead the trigger required a track in both forward and backward iron endcaps plus a hit in the veto wall. 47% of the triggers were reconstructed using the beam halo calibration code as described in section 3.5.5.

It will be noticed from the following discussion that a precise measurement of T_0 and v can only be obtained if both these quantities are input accurately into the reconstruction code. For this reason the measurement procedure from reconstruction onwards was repeated several (> 5) times with values obtained from the previous iteration input into the next. All results presented here are from the final iteration.

4.3.1 Time Distribution Method

The mean of the corrected times, \bar{T} , obtained from a sample of muons passing through a chamber will be equal to the drift time obtained for a muon passing through the exact centre of the drift space, if the illumination of muons and the cell efficiency is uniform w.r.t. drift distance. Stated another way: with uniform illumination there are as many events before the centre of the drift space as after.

Uniform illumination of a single cell is not possible since beam halo has a strong radial ($\simeq Y$) dependence as can be seen in figure 4.3. A Monte Carlo study has shown, however, that uniform illumination can be approximated by combining the time distributions from the cells of both sublayers in a region of the layer where the illumination varies smoothly with Y . Figure 4.4 shows the distance distribution obtained from the study to be flat, indicating a very good approximation to uniform illumination.

The requirement of uniform efficiency across the cell can be seen to be nearly valid by examination of figure 4.6. The small decrease in efficiency near the sense wire is accounted for as a systematic error.

A correction must be made to \bar{T} due to a contamination of the data with events

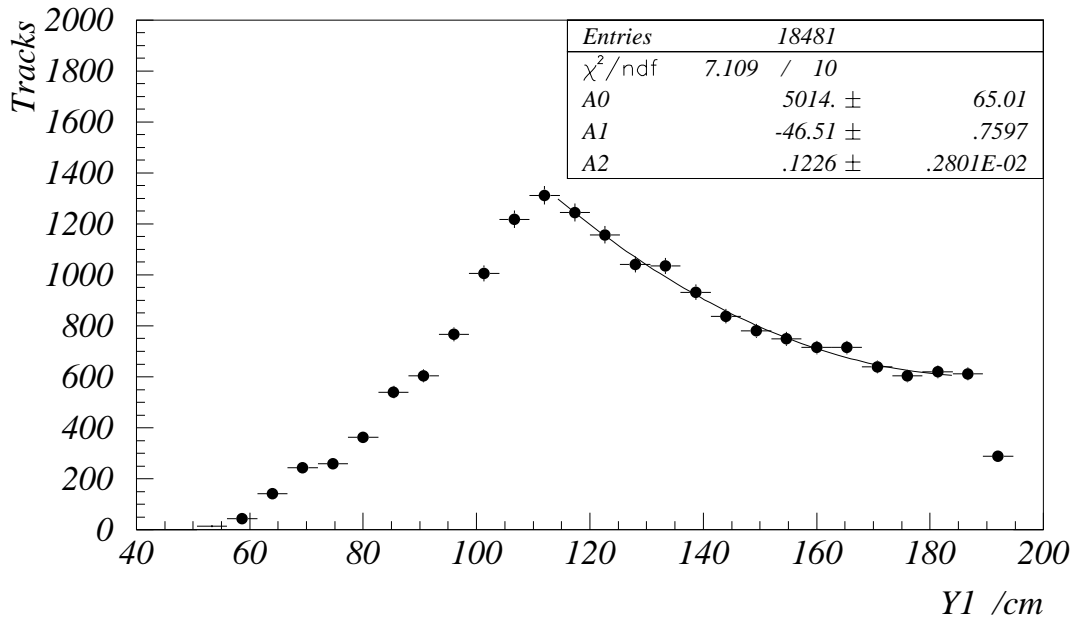


Figure 4.3: Variation of the distribution of reconstructed beam halo muons with Y for θ_I . The fit is a 2-D polynomial.

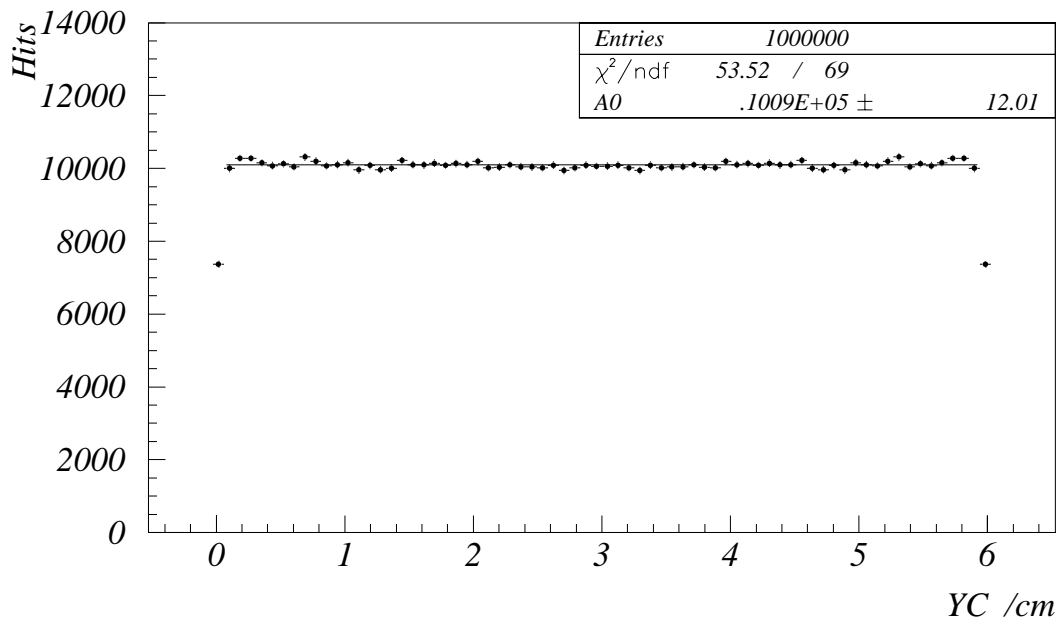


Figure 4.4: The drift distance distribution produced using Monte Carlo data with a Y dependence as shown in figure 4.3 and $Y > 120$ cm. The fit is to a constant.

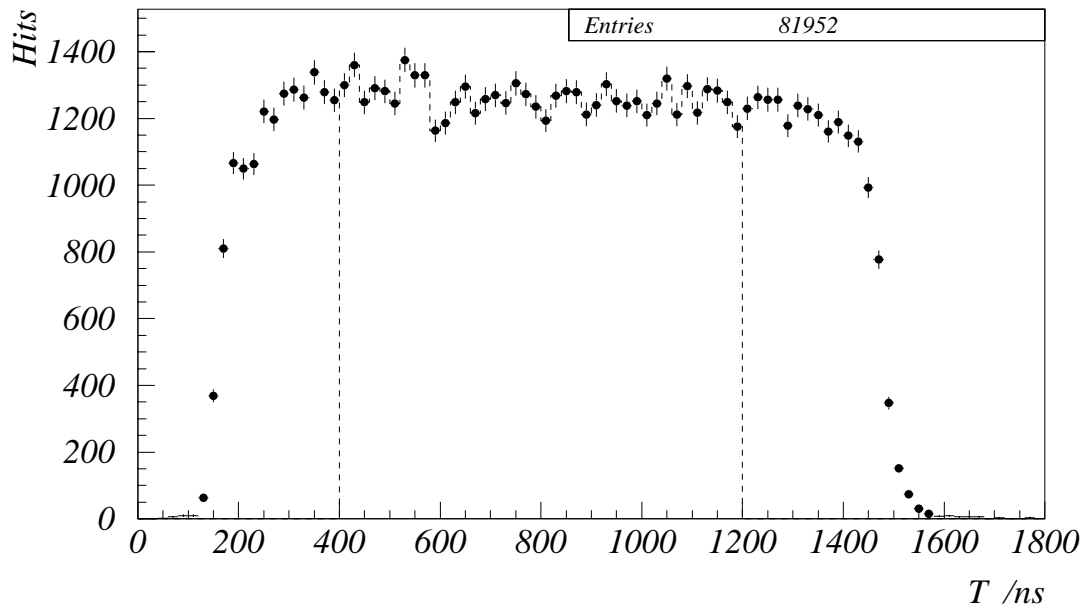


Figure 4.5: The time distribution. The selected mid range, used for the drift velocity determination, is shown with dashes. Beam halo events were selected with $Y1 > 120$ cm.

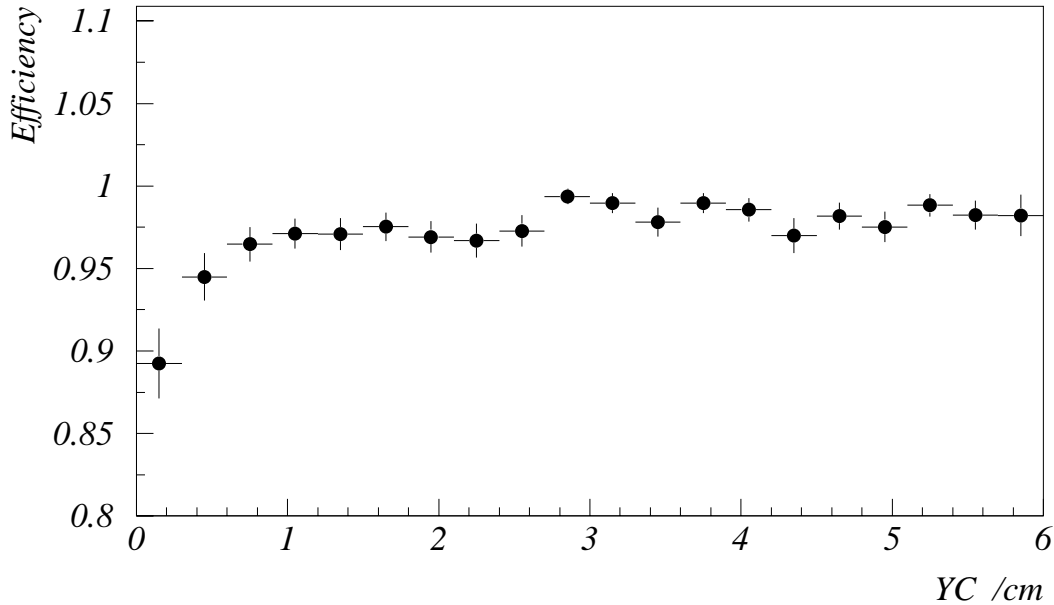


Figure 4.6: Hit efficiency as a function of drift distance. Data are taken from a test rig using cosmics.

arising from the proton satellite bunch that arrives 19.2 ns before the main proton bunch. These events produce beam halo muons with a T_0 shift of 19.2 ns and are estimated to contribute 10% of the total, leading to a correction of +1.92 ns. It should be noted that the filling of the satellite bunches varies on a run by run basis.

\bar{T} can be related to the T_0 , with knowledge of the drift velocity, by

$$T_0 = \bar{T} - \frac{D}{2v} \quad (4.10)$$

where D is the total drift distance of a cell (6.00 cm).

4.3.2 Checksum Method

For a straight line track the gradient as measured by the two sublayers of θ_I will be equal to the gradient as measured by the two sublayers of θ_{II} :

$$Y1 - Y2 - Y3 + Y4 = 0. \quad (4.11)$$

If the above is converted into cell coordinates then for most tracks two possibilities ensue, depending on the ‘stagger’ permutation of the cells (as shown in figure 4.7).

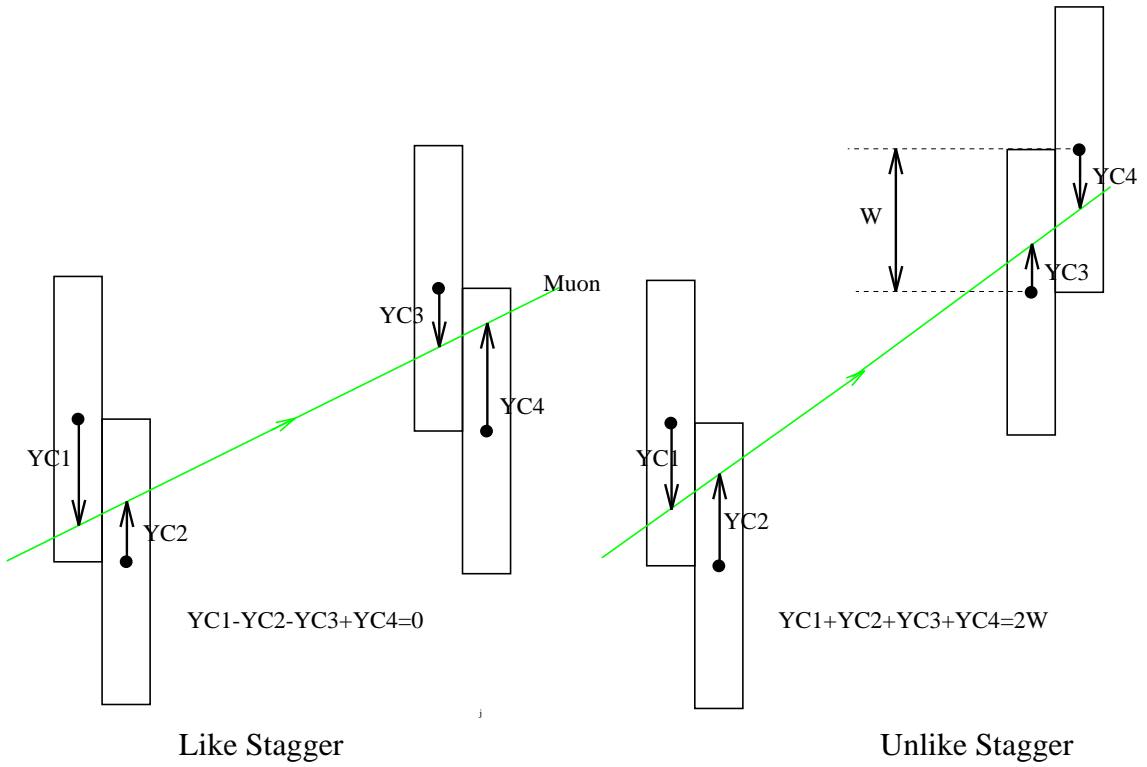


Figure 4.7: The two possible ‘stagger’ permutations with their corresponding check-sums. The ϕ layer has been omitted for clarity.

For like stagger:

$$YC1 + YC2 - YC3 - YC4 = 0 \quad (4.12)$$

For unlike stagger:

$$YC1 + YC2 + YC3 + YC4 = 2W \quad (4.13)$$

The unlike stagger checksum can be converted into a checksum involving corrected times² using equation 3.3 so:

$$T1 + T2 + T3 + T4 = \frac{2W}{v} + 4T_0 \quad (4.14)$$

To remove the dependence of the above checksum with drift velocity a new quantity is defined:

$$T_{mid} = \frac{W}{2v} + T_0 \quad (4.15)$$

²The suffix *cor* will be dropped from now on for reasons of brevity. All times should be assumed corrected unless otherwise stated.

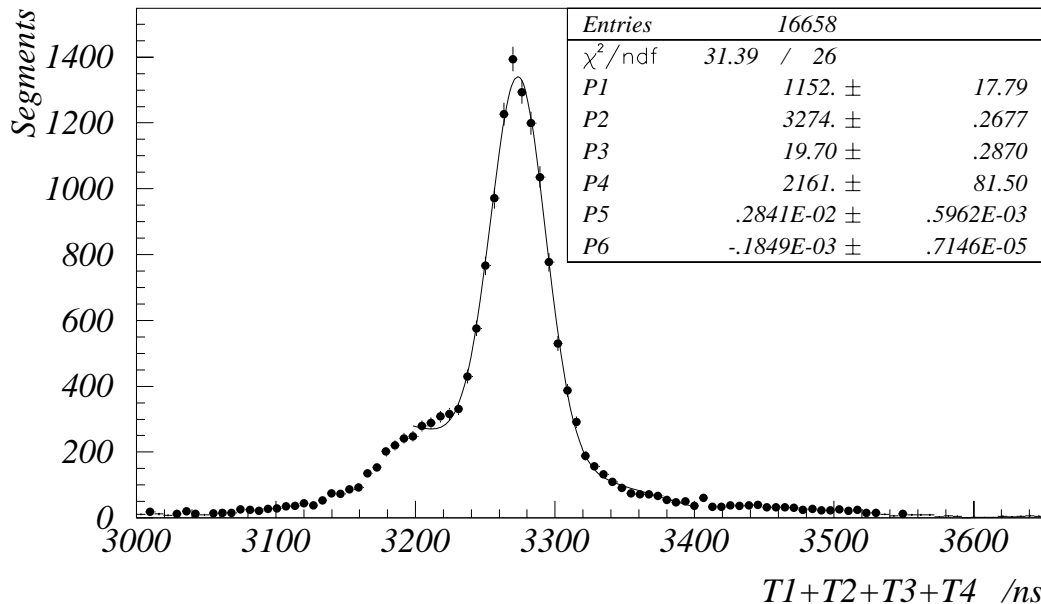


Figure 4.8: Checksum used to calculate T_{mid} . Only events passing through chambers with the unlike stagger permutation were chosen. The fit is a Gaussian plus a 2-D polynomial. The events from the proton satellite bunch at -76.8 ns from the main peak can clearly be seen.

so

$$YC = v(T - T_{mid}) + \frac{W}{2} \quad (4.16)$$

i.e. T_{mid} is the time obtained from a muon passing a distance $W/2$ (3 cm) from the sense wire and, since the cell's drift distance is equal to the wire separation ($W = D$), $T_{mid} \equiv \bar{T}$. Hence:

$$T1 + T2 + T3 + T4 = 4T_{mid} \quad (4.17)$$

A plot of the unlike stagger checksum is shown in figure 4.8.

4.3.3 Error Treatment

The statistical and systematic errors for the two methods used to calculate T_{mid} are shown in tables 4.1 and 4.2. The various contributions were estimated as follows:

- ALP – Possible rotations in α (see table 5.4) of 0.5° .

	Error /ns
ALP	1.7
WIR	1.9
ANG	2.0
DRI	2.5
EFF	0.3
SAT	1.0
SYS	4.2
STA	1.3

Table 4.1: The statistical error and relative contributions to the systematic error on T_{mid} , as determined by the time distribution method.

	Error /ns
ALP	1.7
WIR	1.9
ANG	1.0
SYS	2.7
STA	0.1

Table 4.2: The statistical error and relative contributions to the systematic error on T_{mid} , as determined by the checksum method.

- WIR – Wire by wire T_0 shifts due to uncertainties in the cable and wire correction (TC) and cell by cell misalignment. Calculated by comparing the T_0 obtained from isolated sets of 4 cells within the same octant.
- ANG – Shift due to angular corrections as described in section 4.6.
- DRI – Uncertainty in the total drift space ($D = 6.000 \pm 0.023$ cm).
- EFF – Deviation from uniform efficiency across cell.
- SAT – Uncertainty in the fraction of satellite bunch events ($10 \pm 5\%$).
- SYS – The total systematic error, determined by addition of all the contributing systematic errors in quadrature.
- STA – The statistical error.

4.4 Results

The results from the time distribution are:

$$\bar{T} \equiv T_{mid} = 819.9 \pm 1.3 \pm 4.2 \text{ ns}, \quad (4.18)$$

and from the checksum method:

$$T_{mid} = 818.5 \pm 0.05 \pm 2.7 \text{ ns} \quad (4.19)$$

Once the drift velocity is known T_0 can simply be determined using equation 4.15.

4.5 Calculation of the Drift Velocity

The drift velocity is calculated in two ways. The first uses the time distribution and the second uses a checksum method. The data selection and time distribution used are exactly the same as those used for the T_0 determination.

4.5.1 Time Distribution Method

An ideal drift cell with uniform illumination and efficiency and constant drift velocity would give a top-hat time distribution (with a small amount of smearing at the edges due to non zero spatial resolution). The first two criteria have been shown to be nearly true (see section 4.3) whereas a constant drift velocity is generally limited to certain regions of the drift space. A region where the time distribution is constant corresponds to a region of constant drift velocity. If such a region is chosen as in figure 4.5 then if the number of events within this region is N_{mid} , the length of the chosen region is D_{mid} , the total number of events N and the total drift length D then:

$$D_{mid} = \frac{N_{mid} \cdot D}{N}, \quad (4.20)$$

since v is constant $v = D_{mid}/\Delta T$ so:

$$v = \frac{N_{mid} D}{N \cdot \Delta T}. \quad (4.21)$$

Methods have been devised [11] to account for deviations from uniform drift velocity near the sense wire and outer edge of the cell (caused by the non uniform E-field). Studies have shown that for the present gas and voltage setting making this correction has little impact on the cell's spacial resolution. It is preferred, therefore, to retain the simple model of constant drift velocity across the cell.

4.5.2 Checksum Method

If the gradient of a track measured by the two coordinates of the single sublayer θ_{III} is compared to the gradient measured by the two layers θ_{III} and θ_{IV} the following checksum is obtained:

$$(Y8 + Y7 - Y5 - Y6 - 2\delta Y_{III}) \frac{Z_S}{2Z_L} = Y6 - Y5 \quad (4.22)$$

$$= \pm(W - YC6 - YC5) \quad (4.23)$$

$$= \pm v(T5 + T6 - 2T_{mid}) \quad (4.24)$$

where the value δY_{III} has been included to account for any misalignments in the Y direction between the two layers, the \pm depends on the stagger permutation of θ_{III} , Z_S is the Z separation between the two sublayers of θ_{III} and Z_L is the Z separation between the layers θ_{III} and θ_{IV} . Hence a graph of $T5 + T6 - 2T_{mid}$ versus $(Y8 + Y7 - Y5 - Y6)Z_S/(2Z_L)$ has a gradient of $1/v$ independent of T_{mid} and δY octant misalignments.

It is evident, by considering equation 4.22, that best results are obtained if the track gradient $(Y6 - Y5)$ has as large a range as possible. It is for this reason that only data from post toroid segments are used with the large gradient range arising from bending in the toroid.

Since this method explicitly requires tracks at large angles it is essential that the angular corrections (as described in section 4.6) are performed.

An example plot of the checksum is shown in figure 4.9.

4.5.3 Error Treatment

The statistical and systematic errors for the determination of the drift velocity for the time distribution method are shown in table 4.3. The various contributions were estimated as follows:

- ANG – Shift due angular corrections.
- DRI – Uncertainty in the total drift space ($D = 6.000 \pm 0.023$ cm).
- EFF – Deviation from uniform efficiency across cell.
- LIM – Shifts obtained by changing limits of the central region (by ± 100 ns).
- OCT – Shifts obtained by performing the procedure on isolated octants.

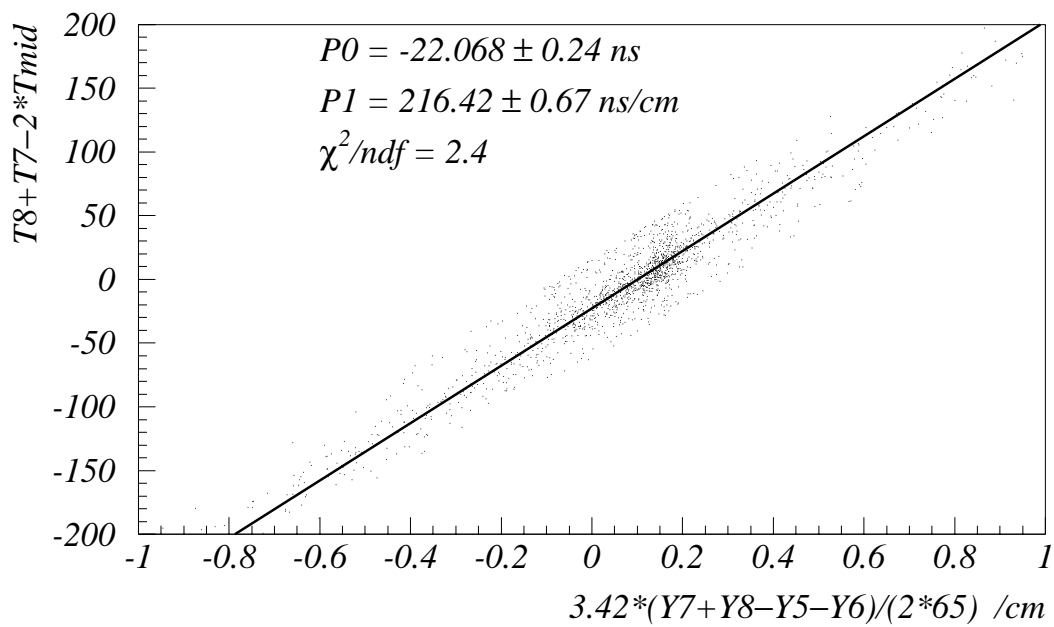


Figure 4.9: The velocity checksum left with angular corrections. Only events in one octant with one stagger permutation have been selected. Events greater than 4σ away from the fitted line have been discarded. Fit is a straight line.

	Fractional Error /%
ANG	0.1
DRI	0.7
EFF	0.1
LIM	0.2
OCT	0.9
SYS	1.3
STA	0.3

Table 4.3: The statistical error and relative contributions to the systematic error on v , as determined by the time distribution method.

- SYS – The total systematic error, determined by addition of all the contributing systematic errors in quadrature.
- STA – The statistical error.

The systematic error for the checksum method was calculated in a slightly different way. The checksum can be plotted for both stagger permutations, for both θ_{III} (equation 4.24) and θ_{IV} :

$$(Y8 + Y7 - Y5 - Y6 - 2\delta Y_{III}) \frac{Z_S}{2Z_L} = \pm v(T7 + T8 - 2T_{mid}) \quad (4.25)$$

and for each octant, leading to 32 possible measurements of v . The spread in the results gives a measurement of the total systematic error. Included in the systematic error are: errors due to the fitting method: wire by wire T_0 differences; Z misalignments; α rotations; and errors in the angular correction.

The systematic error due to the checksum method is:

$$\sigma(v)_{sys} = 1.1\% \quad (4.26)$$

4.5.4 Results

The result from the time distribution method is:

$$v = 4.619 \pm 0.012 \pm 0.058 \text{ cm}\mu\text{s}^{-1} \quad (4.27)$$

and from the checksum method

$$v = 4.582 \pm 0.009 \pm 0.050 \text{ cm}\mu\text{s}^{-1} \quad (4.28)$$

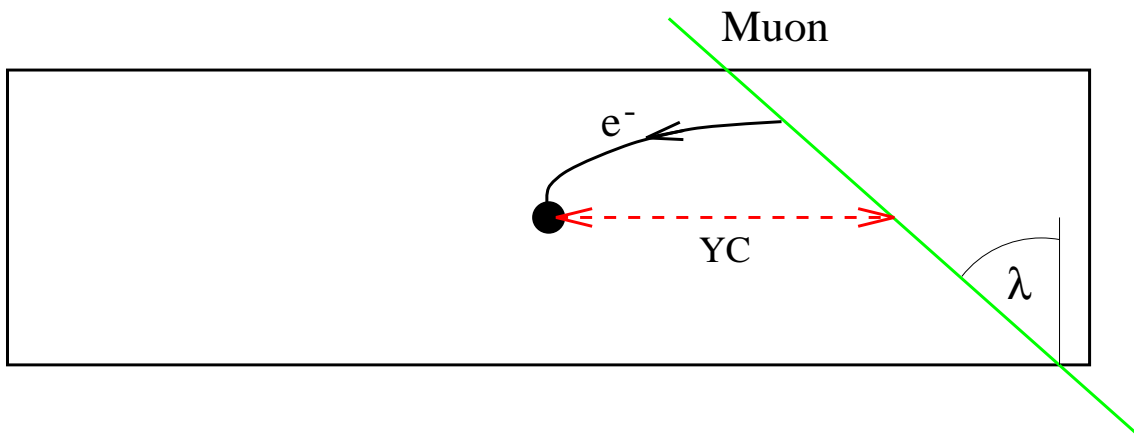


Figure 4.10: Diagram showing the path of the ionised electron that reaches the sense wire first. Its path length is generally less than YC for large λ .

4.6 Angular Corrections

This correction is made to account for the fact that for steep angled tracks the first electron to reach the sense wire will generally not arise from the $ZC = 0$ plane, but from another part of the cell as shown in figure 4.10. This leads to smaller drift times and hence smaller drift distances the steeper the track. To account for this difference a full electrostatic simulation of the cell was done using a modified version of MOPAL [15]. Tracks through the chamber were simulated at all possible angles and positions within the cell. For each angle-position combination all possible electron paths were simulated and the smallest one chosen. It was thus possible to correct the measured drift distance to the true YC . The complete set of angular corrections can be found in [16].

An isochrone map is shown in figure 4.11. Examples of the variation in correction with drift distance and angle are shown in figure 4.12. The effect of angular corrections on the real data is shown in figure 4.13. It can be seen that deviations from the straight line occur at large angles if the angular corrections are not made.

No systematic errors are quoted on this measurement, since the analytic calculation should give results much better than the resolution of the cell. However, if the physical characteristics of the cell are different to those assumed in the calculation then it would be expected that the true angular corrections will be different from those calculated. Since the possible differences are many and difficult to estimate, any errors arising are incorporated into the measured spacial resolution (see section 6.2). Figure 6.1 does indeed show a rise in resolution with angle implying that

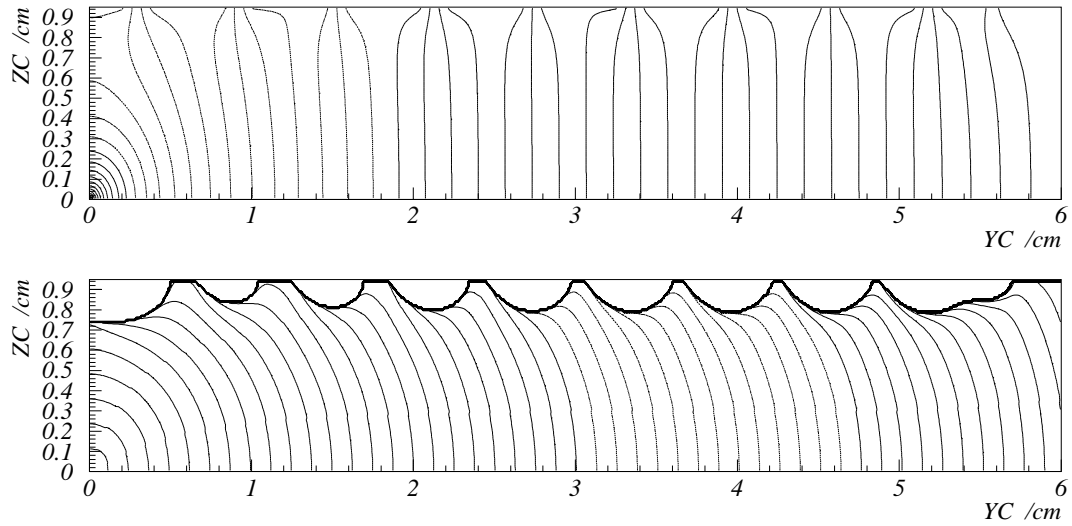


Figure 4.11: The isopotentials (top) and isochrones (bottom) of a quarter cell with sense wire at the origin.

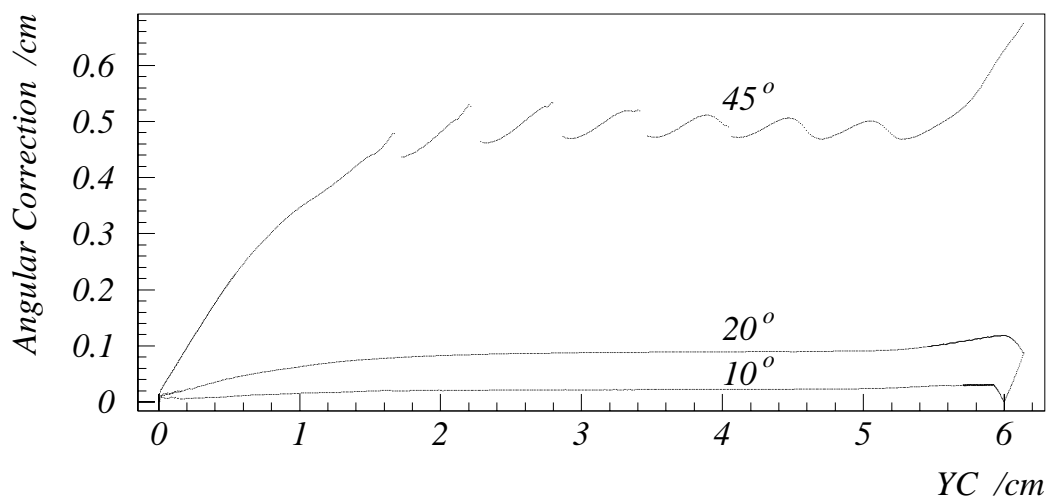


Figure 4.12: The angular corrections for three different angles. The effects of the discontinuous field near the anode strips can clearly be seen in the 45° case.

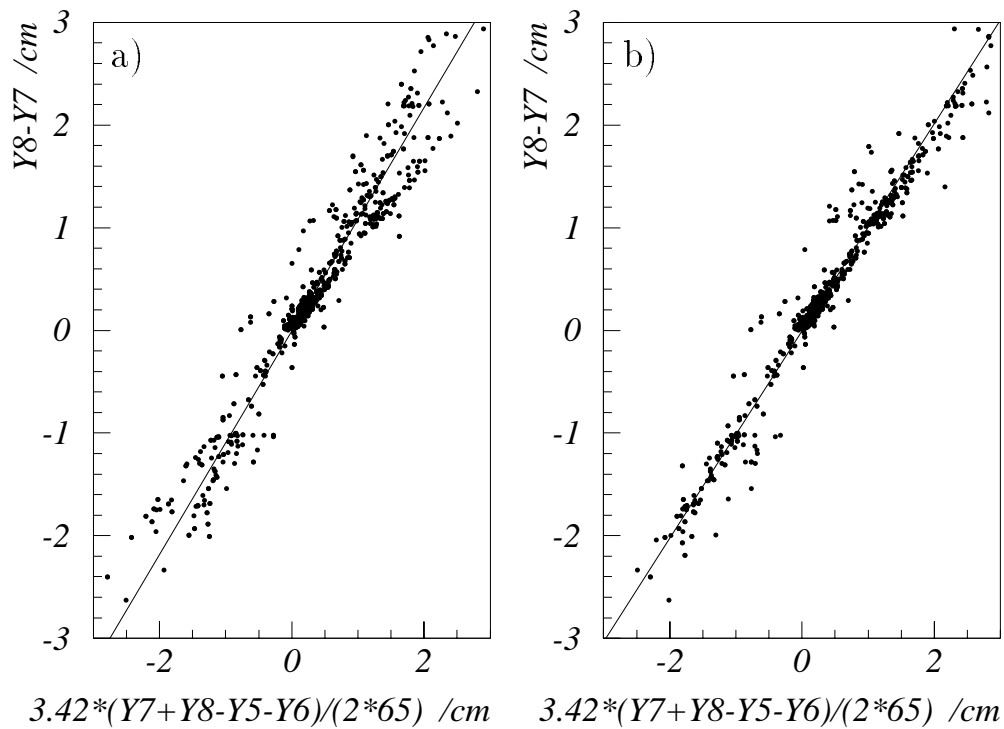


Figure 4.13: The velocity checksum a) without angular corrections and b) with. All octants and stagger permutations have been selected. Points greater than 8σ away from the line $y = x$ have been discarded. Fit is a straight line.

the assumptions that have gone into this calculation are too simplistic and a more detailed treatment could result in a reduction of the resolution at high angles.

Chapter 5

Alignment of the Forward Muon Detector

5.1 Introduction

The cells (and sense wires) are positioned on the octant frame to an accuracy $\simeq 50 \mu m$ [17]. A physical survey [18] has, however, shown that the octants themselves are displaced from their nominal values (i.e. values assumed by the reconstruction) by up to 3 cm. Furthermore, since the layers of the FMD must be moved periodically to provide access to H1, these octant misalignments will not remain constant for all running periods. Precise momentum measurement necessitates determination of the misalignments of the octants ideally to much better than the resolution of the detector. Estimates of the desired upper limit of the misalignments can be seen in figure 5.1 (updated from [19]).

Physical surveys have proved difficult due to the crowded environment of the FMD area. As yet no physical survey has yielded all alignment quantities and for certain running periods no physical survey was possible. It is thus necessary to have independent alignment procedure based upon muons traversing the system. The remainder of this chapter explains the techniques used, the results obtained and the limitations of the method.

5.2 Data Selection

The alignment procedure described here requires a large number (minimum 10,000) of muons, passing through the same octant of all layers of the system, with as large a range in θ as possible (to align in Z) and at large momentum (to reduce toroidal

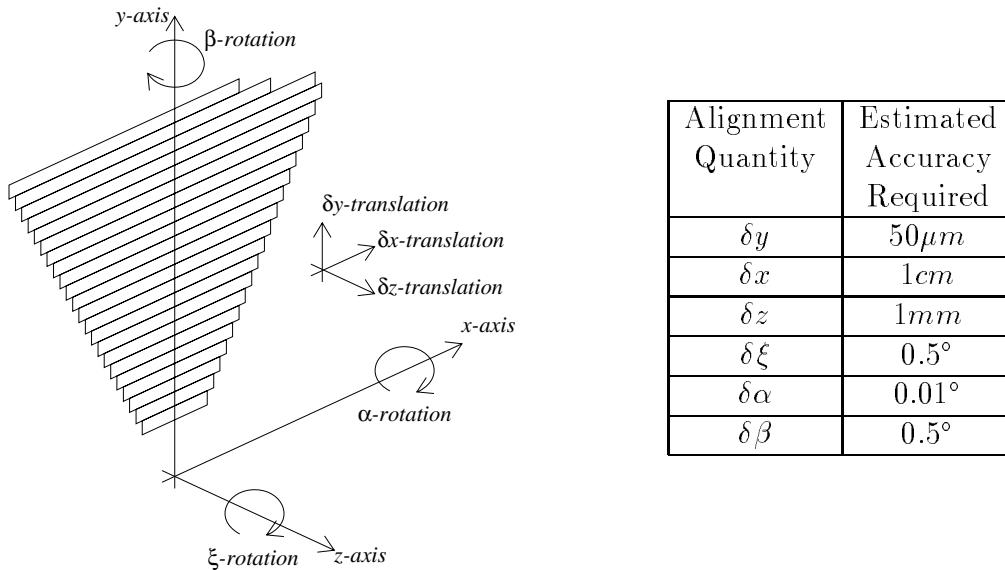


Figure 5.1: The Alignment requirements of the θ layer.

multiple scattering). Cosmic muons are ideally suited, having all of these properties. Physics muons were not used since e-p collision data are always taken with the toroid field on and beam halo were rejected due to their limited angular range.

For the results presented in here 50,000 cosmic muons were triggered using the forward muon trigger with a ‘cosmic load’ as described in [20]. Of these 88% were reconstructed using the cosmic calibration code as described in 3.5.5.

The toroid field was turned off for this run, so that layers from either side of the toroid could be compared.

5.2.1 Translational Alignment

The method used to extract the translational misalignments (following the approach of [19]) uses no information from individual sublayers, instead an average is taken so $Y_I = (Y1 + Y2)/2$, $X_{II} = (X3 + X4)/2$ etc. For a straight track passing through the system the 3-D points as measured by θ_I and θ_{IV} are (arbitrarily) chosen to define the straight line of the track. All other octants are translated so that their measured track points are forced to lie on the line. Resolution and smearing due to multiple scattering are compensated for by repeating the procedure with many events.

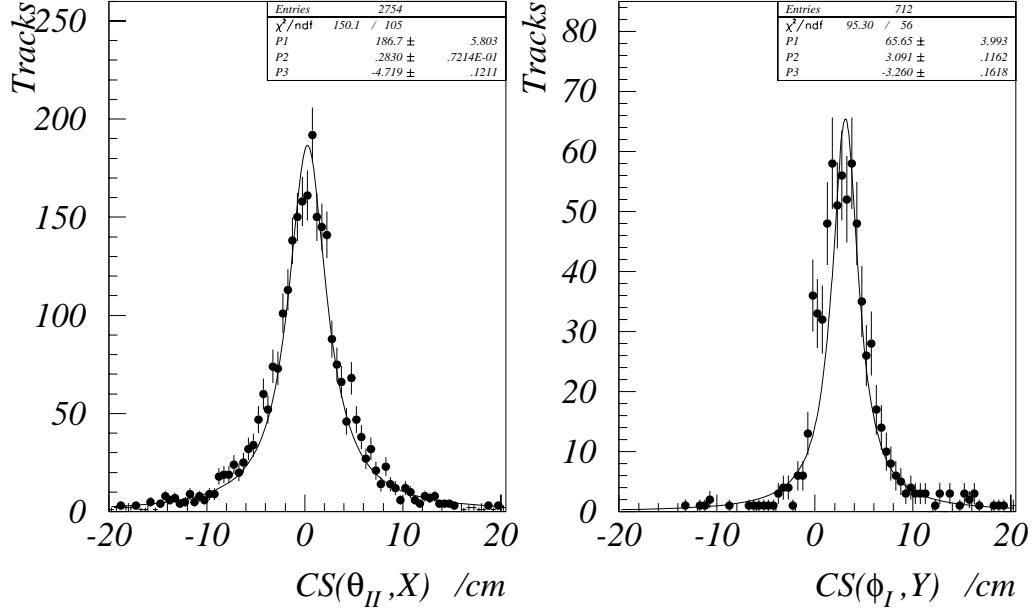


Figure 5.2: Two example alignment checksums. Data are for octant 7. The fit is a Breit-Wigner.

The misalignments (labelled with a prefix of ‘ δ ’) were determined by a checksum method. As an example the Y and Z misalignments of θ_{II} are considered. If all rotational misalignments are ignored then the gradient of a straight track, passing through all layers in the same octant, as measured by $\theta_I \rightarrow \theta_{II}$ should be equal to that measured by $\theta_I \rightarrow \theta_{IV}$:

$$\frac{Y_{II} + \delta Y_{II} - Y_I}{Z_L + \delta Z_{II}} = \frac{Y_{IV} - Y_I}{Z_T} \quad (5.1)$$

$$\frac{Z_L}{Z_T}(Y_{IV} - Y_I) - (Y_{II} - Y_I) = -\frac{\delta Z_{II}}{Z_T}(Y_{IV} - Y_I) + \delta Y_{II} \quad (5.2)$$

Hence a 2-D plot of the checksum, $(Z_L/Z_T)(Y_{IV} - Y_I) - (Y_{II} - Y_I)$, versus the track gradient, $Y_{IV} - Y_I$, has a gradient of $-\delta Z_{II}/Z_T$ and an intercept of δY_{II} . Similar results holds for the other layers, although for checksums involving X coordinates (including all ϕ layer misalignments) the resolution is much worse than any effects due to Z misalignments. So for instance δX_{II} is determined by a 1-D plot:

$$\delta X_{II} = \frac{Z_L}{Z_T}(X_{IV} - X_I) - (X_{II} - X_I) \quad (5.3)$$

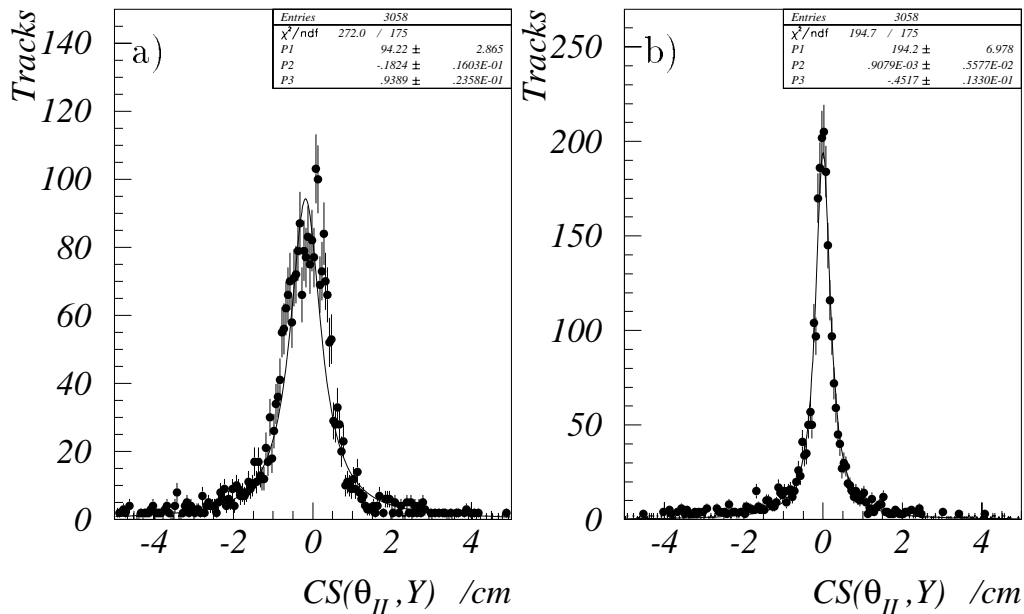


Figure 5.3: One dimensional plots of $CS(\theta_{II}, Y)$ after a) first iteration and b) after fifth iteration. Data are for octant 7. The fit is a Breit-Wigner.

$CS(\theta_{II}, X)$	$= (X_{IV} - X_I)Z_L/Z_T - (X_{II} - X_I)$
$CS(\theta_{II}, Y)$	$= (Y_{IV} - Y_I)Z_L/Z_T - (Y_{II} - Y_I)$
$CS(\theta_{III}, X)$	$= (X_{IV} - X_I)Z_L/Z_T - (X_{IV} - X_{III})$
$CS(\theta_{III}, Y)$	$= (Y_{IV} - Y_I)Z_L/Z_T - (Y_{IV} - Y_{III})$
$CS(\phi_I, X)$	$= (X_{IV} - X_I)Z_L^\phi/Z_T - (Y_I^\phi - X_I)$
$CS(\phi_I, Y)$	$= (Y_{IV} - Y_I)Z_L^\phi/Z_T - (X_I^\phi - Y_I)$
$CS(\phi_{II}, X)$	$= (X_{IV} - X_I)Z_L^\phi/Z_T - (X_{IV} - X_{II}^\phi)$
$CS(\phi_{II}, Y)$	$= (Y_{IV} - Y_I)Z_L^\phi/Z_T - (Y_{IV} - Y_{II}^\phi)$

Table 5.1: The alignment checksums. Coordinates obtained from the ϕ layers have a superscript ' ϕ '. Coordinates from the θ layers have no superscript. Z_L is the separation in Z between the misaligned layer and θ_I for pre-toroid layers or θ_{IV} for post-toroid layers. Z_T is the separation in Z between θ_I and θ_{IV} .

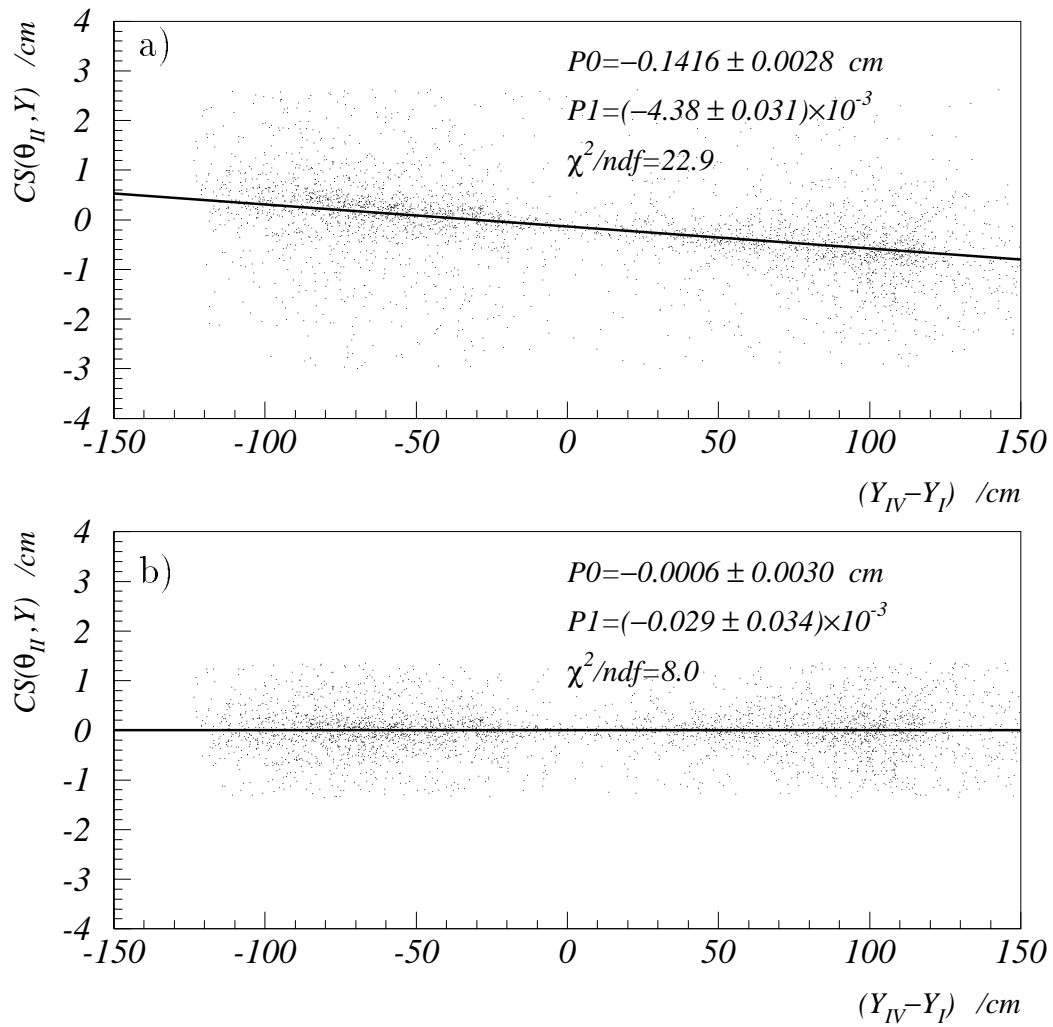


Figure 5.4: Two dimensional plots of $CS(\theta_{II}, Y)$ versus track angle after a) first iteration and b) after fifth iteration. Data are for octant 7.

A full list of the checksums used to align in X , Y and Z is shown in table 5.1.

It has been shown [19] that toroidal multiple scattering produces deviations from a straight line which follow a Breit-Wigner distribution. This inevitably leads to long tails in all alignment checksums. For the 1-D plots the tails are simply dealt with by fitting to a Breit-Wigner function as shown in figure 5.2.

The 2-D plots cannot be treated so simply. A simple least squares fit is inadequate since small statistical fluctuations in the number of events in the tails cause large fluctuations in the values of the fit. A more complex fit of a Breit-Wigner convoluted with a straight line could in principle be used. However, since both the height and width would vary along the line (and have sharp cut offs), the fit would become extremely complicated. Instead the tails of the distribution are cut, the checksum fitted using a least squares fit and an iterative procedure employed to ensure the final result is free from any bias introduced from the cut.

The full procedure is as follows. First the checksum is plotted in 1-D and fitted with a Breit-Wigner (an example is shown in figure 5.3.a). The checksum is now plotted versus the track gradient, with events greater than 3Γ (Γ being the full width half maximum) from the mean removed and a least squares fit performed (as shown in figure 5.4.a). The results are then used to align the octant in Y and Z and the whole procedure repeated several ($\simeq 5$) times until the straight line fit yields values for the gradient and intercept consistent, within errors, with zero (see figure 5.4.b). The misalignments are then taken as the sum of the values obtained after each iteration.

An estimate of the statistical error on the fitted variables is made by taking Γ obtained from the 1-D plot after the last iteration (figure 5.3.b) and assigning each ordinate coordinate of the 2-D plot an error of $\Gamma/2.35$ (the F.W.H.M. of a Gaussian being 2.35σ [21]).

5.2.2 Rotational Alignment

The rotational misalignments could in principle be found using a similar approach to that used in the translational case. This would need very precise translational alignment as a prerequisite and also involve rather complicated checksums involving all 3 spacial coordinates (rather than 2 in the translational case). Since the origin of certain systematics is uncertain no attempt has been made. It is possible, however, by using information from the sublayer coordinates to determine $\delta\alpha$ for the θ planes, but no alignment method has yet been developed for the other rotational quantities.

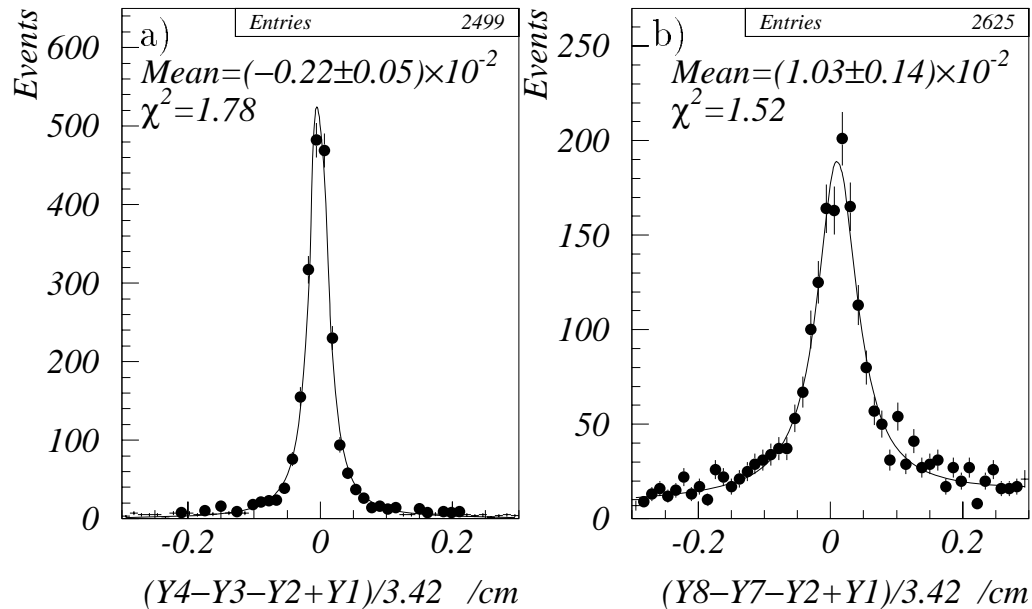


Figure 5.5: Example checksums used in $\delta\alpha$ determinate a) for θ_{II} and b) for θ_{IV} . Fit is a) a Breit-Wigner and b) a Breit-Wigner plus 2-D polynomial.

The gradient as determined by a sublayer $(Y2 - Y1)/Z_S$ should be the same for all layers the track passes through. Any difference will arise almost completely from α rotations. The θ_I is chosen as the reference so for example:

$$\delta\alpha_{III} = \frac{1}{Z_S}(Y5 - Y3 - Y2 + Y1). \quad (5.4)$$

As can be seen by the plots of this quantity (figure 5.5) there is large smearing due to multiple scattering when layers either side of the toroid are compared. The peak position is, however, still well defined.

5.3 Error Treatment

The statistical and systematic errors for the alignment quantities are given in tables 5.2, 5.3 and 5.4 with the following contributions:

- ZMI – Shifts due to Z misalignments (of ± 1 cm)

	$\sigma(\delta X) / \text{cm}$	$\sigma(\delta X^\phi) / \text{cm}$	$\sigma(\delta Y^\phi) / \text{cm}$
ZMI	0.024	0.30	0.10
LIM	0.040	0.22	0.08
SYS	0.047	0.37	0.13
STA	0.077	0.25	0.12

Table 5.2: The statistical error and the relative contributions to the systematic errors on δX for the θ and ϕ layers and on δY for the ϕ layers.

	$\sigma(\delta Y) / \text{cm}$	$\sigma(\delta Z) / \text{cm}$
ALP	0.019	0.13
BET	0.012	0.04
XIR	0.001	0.00
LIM	0.022	0.06
SYS	0.031	0.15
STA	0.003	0.01

Table 5.3: The statistical error and the relative contributions to the systematic error on δY and δZ for the θ layers.

- LIM – Shifts due to changing the cut-off on the tails of the fitted distribution (cut changed from 50 cm to 25 cm for the 1-D translational fits, 3Γ to 6Γ for the 2-D translational fits and from 0.3 rad to 0.5 rad for the $\delta\alpha$ fit.)
- ALP – Shifts due to α rotations (of 0.5°)
- BET – Shifts due to β rotations (of 0.5°)
- XIR – Shifts due to ξ rotations (of 0.5°)
- WIR – Shifts due to wire by wire T_0 differences (of 1.9 ns)
- SYS – The total systematic error, determined by addition of all the contributing systematic errors in quadrature.
- STA – The statistical error

5.4 Results

The misalignments can be found in tables 5.5 and 5.6

	$\sigma(\delta\alpha_{II})/^\circ$	$\sigma(\delta\alpha_{III})/^\circ$	$\sigma(\delta\alpha_{IV})/^\circ$
WIR	0.076	0.076	0.076
LIM	0.002	0.055	0.025
SYS	0.076	0.094	0.080
STA	0.032	0.070	0.068

Table 5.4: The statistical error and the relative contributions to the systematic error on $\delta\alpha$ for the θ layers.

Layer	Octant	δX /cm	δY /cm	δZ /cm
θ_{II}	1	-0.35	-0.282	0.70
θ_{II}	2	-0.84	-0.051	0.44
θ_{II}	3	0.81	-0.200	-0.75
θ_{II}	4	-0.16	-0.425	-1.49
θ_{II}	5	0.01	-0.315	-1.22
θ_{II}	6	0.00	-0.032	-2.10
θ_{II}	7	0.28	-0.126	1.57
θ_{II}	8	-0.34	-0.390	0.83
θ_{III}	1	0.93	1.761	-0.71
θ_{III}	2	-1.98	1.399	-0.99
θ_{III}	3	-1.29	0.380	-0.54
θ_{III}	4	-0.29	-0.640	-0.31
θ_{III}	5	-0.38	-1.269	-0.36
θ_{III}	6	1.11	-0.734	-1.27
θ_{III}	7	1.21	0.670	-0.44
θ_{III}	8	1.24	1.624	-0.88
ϕ_I	1	-0.45	3.45	–
ϕ_I	2	0.03	-4.08	–
ϕ_I	3	0.41	1.81	–
ϕ_I	4	2.17	-4.62	–
ϕ_I	5	1.60	3.99	–
ϕ_I	6	0.45	-0.19	–
ϕ_I	7	1.73	-3.09	–
ϕ_I	8	-1.16	-1.80	–
ϕ_{II}	1	-2.02	3.52	–
ϕ_{II}	2	0.10	-1.69	–
ϕ_{II}	3	-3.06	-1.13	–
ϕ_{II}	4	-4.32	-4.64	–
ϕ_{II}	5	-2.14	3.91	–
ϕ_{II}	6	-1.76	0.17	–
ϕ_{II}	7	-1.73	1.02	–
ϕ_{II}	8	-3.62	-3.46	–

Table 5.5: The translational misalignments.

Octant	$\delta\alpha_{II} / ^\circ$	$\delta\alpha_{III} / ^\circ$	$\delta\alpha_{IV} / ^\circ$
1	-0.22	0.76	0.70
2	0.03	0.73	0.70
3	0.20	-0.22	0.21
4	0.01	-0.63	-0.53
5	-0.39	-0.91	-0.94
6	-0.31	-0.22	-0.22
7	-0.12	0.32	0.16
8	-0.13	0.37	0.59

Table 5.6: The rotational misalignment, $\delta\alpha$.

Chapter 6

Performance of the Forward Muon Detector

6.1 Introduction

The focus of chapters 4 and 5 has been determination of the coordinates of a muon track to as great an accuracy as possible. Particular emphasis has been placed on reducing measurement error on $\Delta\theta_T$ ($\simeq (Y_{IV} - Y_{III} - Y_{II} + Y_I)/Z_L$), so prominence has been given to the Y coordinate of the θ layers. This chapter gives a detailed survey of the performance of the detector once all corrections of the preceding chapters have been taken into account. The first section gives measurements of misalignment free spacial resolutions as obtained from real data. The second section gives an estimate of the momentum resolution determined using a full Monte Carlo simulation of the detector. To take into account any possible inadequacies of the alignment method the layers of the detector are first misaligned and then realigned using the same procedure as for real data.

6.2 Spacial Resolution

The resolution for the drift coordinate ($\sigma(Y)$) is determined from the spread in the like stagger checksum (equation 4.12). This gives an estimate of the resolution free from translational octant alignment and uncertainties in drift velocity and event tzero. All other factors affecting the resolution (including cell misalignments, cell by cell tzero differences and rotational octant misalignments) are included. The checksum distribution is fitted to a Breit-Wigner and then converted to a standard deviation using the same approach as in 5.2.1. The results (shown in figure 6.1) can

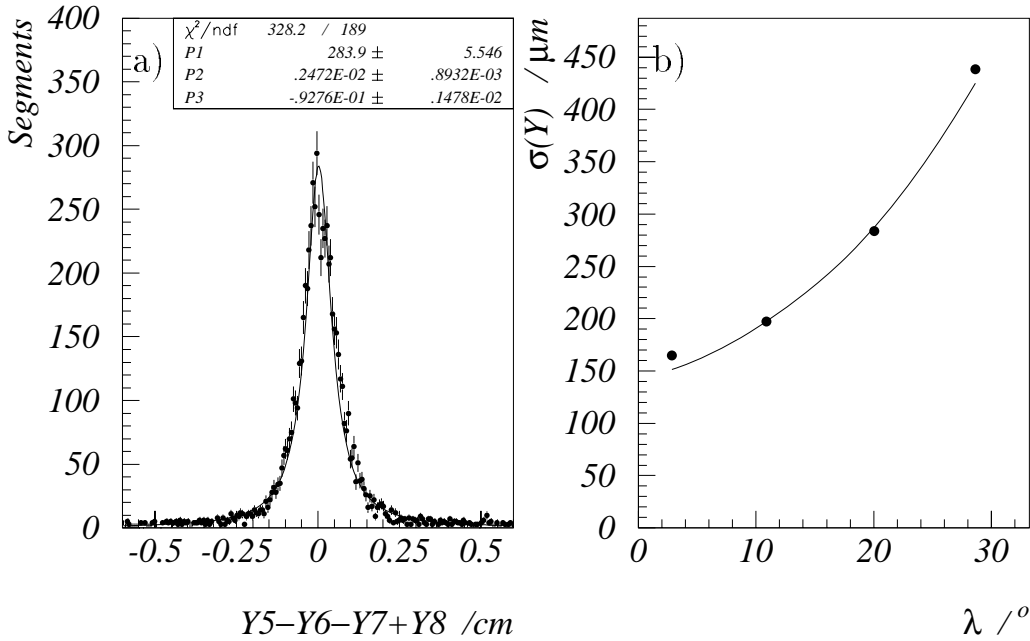


Figure 6.1: The resolution in Y : a) checksum used for resolution determination for muons at 12° . Only data with a like sign stagger permutation have been used. The fit is a Breit Wigner; b) resolution, defined as $\Gamma/4.7$ where Γ is the F.W.H.M. of the checksum, plotted as a function of track angle, λ . Cosmic data were used.

be seen to be strongly dependent on the track angle, λ (defined in figure 4.10).

The resolution in X is determined as a fraction of the total wire length of the cell pair, L . The resolution is determined using the X checksum corresponding to equation 4.12 and is plotted in figure 6.2. Again a Breit-Wigner is fitted to the distribution and a conversion made from the F.W.H.M. to a standard deviation. The result is:

$$\sigma\left(\frac{X}{L}\right) = 0.021 \quad (6.1)$$

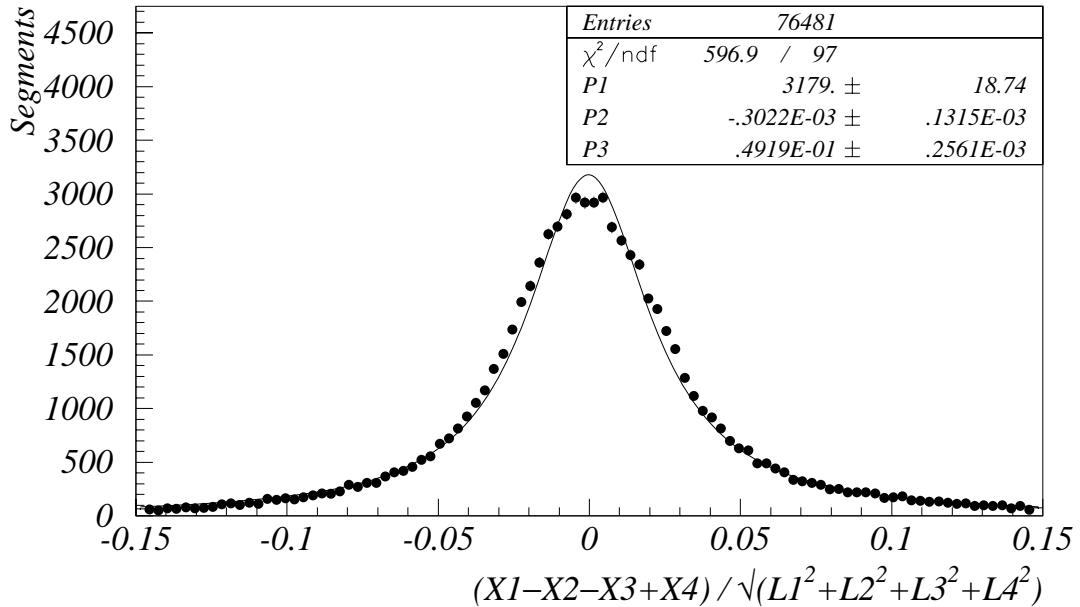


Figure 6.2: Checksum used to determine the resolution in X . The fit is a Breit Wigner. Cosmic data were used.

6.3 Momentum Resolution

6.3.1 Monte Carlo Simulation

Two Monte Carlo simulations of the misaligned FMD were performed. The first ‘cosmic’ simulation was used to produce alignment quantities and the second ‘physics’ simulation used to provide the momentum resolutions.

For the cosmic simulation single muons were produced with a momentum range of 5–50 GeV, a top hat θ distribution from 0–30°, uniform in ϕ with a nominal H1 vertex and extremely large (Gaussian) smearing in its vertex O_X and O_Y positions of ± 200 cm. The toroid field was off for this simulation. Using the results of 6.2 as a rough guide each Y coordinate was smeared using a Gaussian of $\sigma = 250 \mu\text{m}$ and each X coordinate by $\sigma = 1\%$ of the cell pair wire length. With reference to the results of chapter 5, each octant was individually translated and rotated from its nominal position using a random top hat function with limits of ± 2 cm in each of X , Y and Z and of $\pm 0.5^\circ$ in each of α , β and ξ . Out of a total of $\simeq 87,000$ simulated muons 12434 were reconstructed using the calibration code. The reason for the low

reconstruction efficiency was that the muons were not geometrically constrained to pass through all layers of the same octant as required by the reconstruction. The data were then put through the alignment procedure as described in chapter 5.

For the physics simulation single muons were simulated from the H1 vertex with a momentum range of 5–50 GeV, a top hat θ distribution from 2° to 20° and uniform in ϕ . The toroid field was on. The octants were misaligned to exactly those values used in the cosmic case. The simulated muons were reconstructed using the full forward muon reconstruction, including a realignment bank containing the quantities determined by the cosmic simulation.

6.3.2 Results

The fractional inverse momentum resolution is defined as the standard deviation of a distribution in $\delta_{1/p}/(1/p)$, where

$$\frac{\delta_{1/p}}{1/p} = \frac{|1/p_{rec} - 1/p_{gen}|}{1/p_{gen}} \quad (6.2)$$

with p_{gen} the generated momentum at the vertex and p_{rec} the momentum at the vertex as reconstructed by the FMD.

A resolution based on inverse momentum is used in preference to one in momentum since it generally gives a more Gaussian spread. The momentum resolution as a function of momentum, for various levels of misalignment and for both momentum reconstruction techniques (as described in section 3.5.4), can be seen in figure 6.3. It can be seen that without any alignment procedure the momentum resolution is only reasonable ($< 50\%$) for $p < 20$ GeV. After the alignment procedure, if the angular method is used, the momentum resolution is reasonable up to 100 GeV and substantial improvements have been made at lower values.

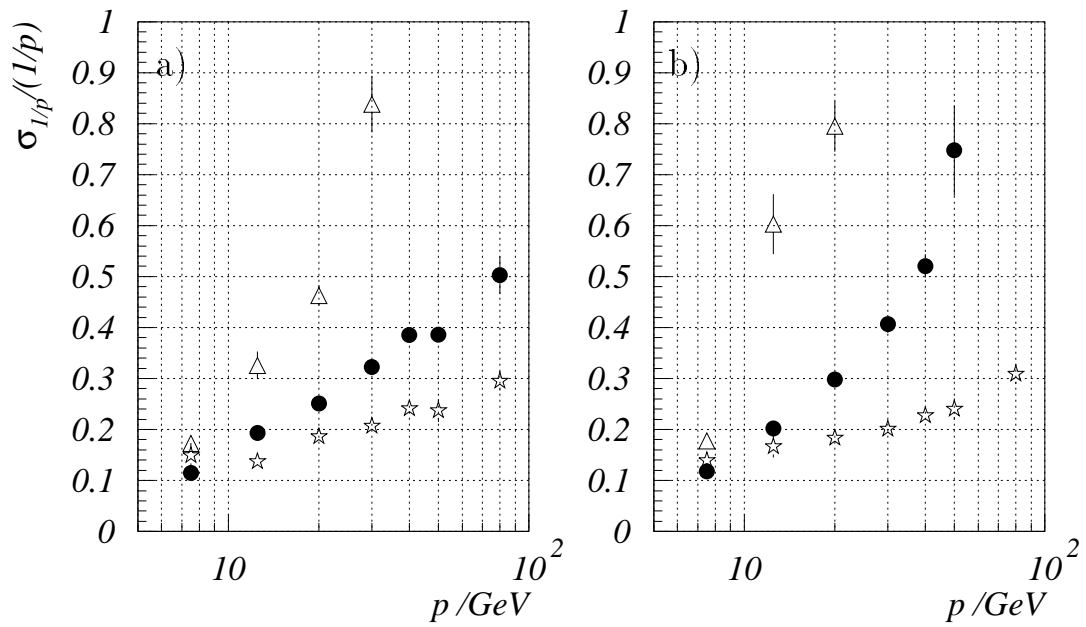


Figure 6.3: The momentum resolution as a function of momentum as determined a) by the angular method and b) by the full fit method. Open triangles are with no alignment, closed circles with alignment as described in text and open stars for perfect alignment. Monte Carlo data have been used.

Chapter 7

Diffractive DIS at H1

7.1 Introduction

Although diffractive processes have been observed since very early particle scattering experiments, there is still no clear understanding of the exact nature of the interaction. Diffraction is generally modelled by the exchange of a vacuum state Regge pole — the pomeron. The reasons for the existence of the pomeron and what specifically the pomeron is are questions that are far from resolved. DIS not only allows a measurement of the pomeron content of the proton (that can be compared with previous experiments) but also allows a unique opportunity to measure the structure of the pomeron itself. The kinematics of HERA (in particular the very low x reachable) make it the first DIS experiment where measurement of the pomeron structure is possible. Only direct processes (see section 7.7.3) have been observed in previous DIS experiments.

Diffractive events are characterised experimentally by a large region in the pseudorapidity, η^1 , distribution of the hadronic final state where no particles are observed. The ‘rapidity gap’ extends typically greater than 1 unit of pseudorapidity. Standard non diffractive models predict only a very small number of events to have such large rapidity gaps. It has been observed in many high energy collision experiments that in a large fraction ($\sim 70\%$) of events with a rapidity gap one of the incident hadrons remains intact after the collision. In these events the elastically scattered hadron marks one of the boundaries of the gap.

¹ $\eta = -\ln(\tan(\theta/2))$

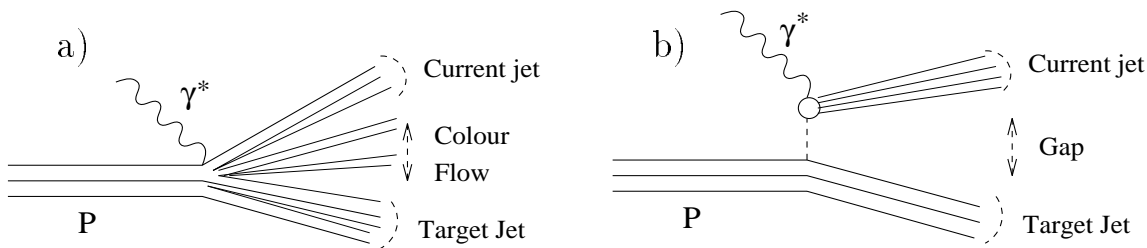


Figure 7.1: Diagrams a) of a standard DIS event with colour flow between the current and target jets and b) of a diffractive event where there is no colour flow.

7.2 Interpretation of Events with a Rapidity Gap in Terms of a Colourless Exchange

Figure 7.1.a shows a diagram of a standard DIS event, where the virtual photon interacts with one of the valence quarks. The reason for the absence of a gap is clear: there is a colour string between the target and current jet, since both the struck quark and the proton remnant are in a coloured state. To fulfil the requirement of colour confinement the region between the target and current jets must be filled with hadrons. Conversely, if the proton remains intact (or in a low mass colourless state) then there is no colour string between the target and current jets, no requirement of hadron production and so a gap may be produced (see figure 7.1.b). In this scenario the photon cannot interact directly with a valence quark or indeed any other parton from the proton all of which are coloured. Instead some colourless combination of quarks or gluons is thought to become separated from the proton and it is this object (or a parton from within it) which undergoes the hard collision with the virtual photon.

7.3 Identity of the Colourless Exchange

The model of colourless exchanges is the Regge theory. This model has been used to successfully predict many of the aspects of pp , $p\bar{p}$ collisions and photoproduction. The model interprets simple scattering processes as the virtual exchange of bound state hadrons. The scattering amplitude for a particular reaction (say $\pi^- + p \rightarrow \pi^0 + n$) can be calculated by summing over all possible hadron states that allow charge, isospin, spin, parity, G parity, strangeness etc. to be conserved. The path that links this set of particles in particle spin–mass space is called a Regge trajectory.

The partial wave amplitudes for each state is found by solving the Schrödinger equation with a Yukawa potential (see for example [22]). The theory gives results in very good agreement with data for simple inelastic reactions (such as $\pi^- + p \rightarrow \pi^0 + n$ or $\pi^- + p \rightarrow \rho^- + p$) although more complicated processes involving more than two hadrons in the final state need sophisticated Regge models (such as triple Regge exchange).

Applying Regge theory to elastic reactions such as $\pi^+ + p \rightarrow \pi^+ + p$ with the reaction mediated via Regge trajectories of known neutral particles would indicate a cross section that falls with centre of mass energy. What is experimentally observed, however, is a cross section that is slightly rising with centre of mass energy. In the Regge picture this would indicate an exchange of a set of particles with quantum numbers of the vacuum (zero charge, zero isospin, positive parity, zero baryon number) and even spin. The trajectory is known as the Pomeraňuk pole or pomeron (\mathbb{P}) for short. No recorded bound hadron (or other) states that possess both the vacuum quantum numbers and the correct spin-mass states as predicted by the theory have yet been observed i.e. the pomeron is not a bound state object. Processes that involve pomeron exchange are known as diffractive.

Regge theory predicts that quasi-elastic reactions at higher energy (such as $p + \bar{p} \rightarrow p + X$ or $e + p \rightarrow e + p + X$) are dominated by pomeron exchange, since the cross sections for other exchanges fall with centre of mass energy. Results from $p\bar{p}$, photoproduction and DIS (see chapter 10) show good agreement with predictions from Regge theory.

7.4 Kinematics of Diffraction

For a DIS diffractive event the presence of a gap leads to 3 experimentally observable 4-vectors in the final state rather than 2 in the standard DIS case. This leads to 4 independent kinematic variables: Q^2 and x , defined as for standard DIS:

$$Q^2 = -(k - k')^2 \quad (7.1)$$

$$x = \frac{Q^2}{2p \cdot (k - k')} \quad (7.2)$$

and the diffractive variables $x_{\mathbb{P}}$ and t :

$$t = (p - p')^2 \quad (7.3)$$

$$x_{\mathbb{P}} = \frac{(k - k') \cdot (p - p')}{(k - k') \cdot p} \quad (7.4)$$

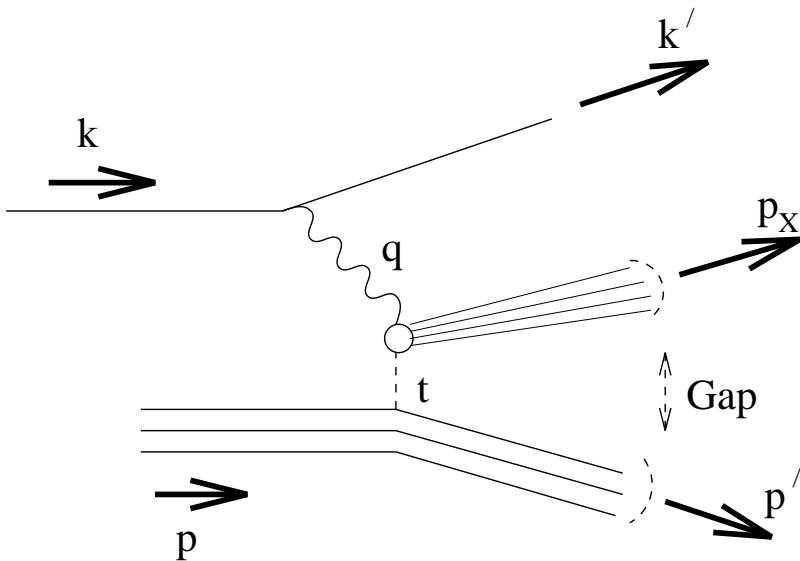


Figure 7.2: The 4-momentum vectors for a diffractive NC DIS process.

$$\simeq 1 - \frac{|\mathbf{p}'|}{|\mathbf{p}|}, \quad (7.5)$$

where the 4-vectors are defined in figure 7.2. t can be interpreted as the 4-momentum transfer at the pomeron-proton vertex and x_P as the fraction of the proton's momentum carried by the pomeron.

7.5 Factorisation of the Diffractive Structure Function

It is possible to define a diffractive proton structure function in analogy to the standard proton structure function (equation 1.12):

$$\frac{d^4\sigma(x_P, t, x, Q^2)}{dx_P dt dx dQ^2} = \frac{4\pi\alpha^2}{xQ^4} \left(1 - y + \frac{y^2}{2(1+R)}\right) F_2^D(x, Q^2; x_P, t), \quad (7.6)$$

where contributions from F_3^D have been neglected and $R = F_L^D/(F_2^D - F_L^D)$. F_2^D is the usual method of expressing the diffractive differential cross section.

There is much theoretical support (see for example [23]) for the ansatz of factorisation. This states that F_2^D can be written as the product of a flux factor, $f_{\mathbb{P}/p}$, and the pomeron structure function $F_2^{\mathbb{P}}$ such that:

$$F_2^D(x, Q^2; x_P, t) = f_{\mathbb{P}/p}(x_P, t) F_2^{\mathbb{P}}(\beta, Q^2) \quad (7.7)$$

where $\beta = x/x_P$ is the fraction of the pomeron's momentum carried by the object struck by virtual photon. In this picture the process of emission of a pomeron by the proton and the interaction of the virtual photon with the pomeron are independent. The reasoning behind the factorisation ansatz is due to the very different time scales of the two interactions. At the proton-pomeron vertex the momentum transfer, t ($< \sim 0.2 \text{ GeV}^2$), is generally much smaller than that at the photon-pomeron vertex, Q^2 ($> 5 \text{ GeV}^2$). The non perturbative part of the structure function is now distinct from the perturbative part, so whilst it must be admitted that pQCD cannot be used to explain $f_{P/p}$, F_2^P is a quantity that can be treated perturbatively. $F_2^P(\beta, Q^2)$ now gives all the information about the pomeron that $F_2(x, Q^2)$ gives about the proton. For example if the pomeron had no internal structure it would be expected that $F_2^P = \delta(\beta - 1)$ or if it had partonic structure then:

$$F_2^P(\beta, Q^2) = \sum_f e_f^2 [\beta q_f(\beta, Q^2) + \beta \bar{q}_f(\beta, Q^2)] \quad (7.8)$$

where βq_f and $\beta \bar{q}_f$ are the quark and antiquark momentum density functions for each quark flavour f .

7.6 Structure of the Pomeron

As previously explained no bound state pomeron has yet been observed. It's structure is therefore far from certain. It is natural to assume that the pomeron is composed of partons. If so then the simplest structure would be a colourless singlet of a quark antiquark pair (quark model) or a pair of gluons (gluon model). QCD pair production diagrams ($g \rightarrow q\bar{q}$ and $q \rightarrow gg$) would result in an admixture of quark and gluon states for both models. The precise composition and how it varies in β and Q^2 should be readily calculable with pQCD if the initial state is assumed. More complex models involving 3 or more initial (i.e. before QCD splitting) partons are also possible.

For both models the leading order QCD diagram is shown in figure 7.3.a, although for the gluon model, because of its higher gluon density, the next to leading order diagram of figure 7.3.b should contribute significantly.

Measurement of F_2^D and F_2^P and their evolution in β and Q^2 allows (in analogy with the proton) extraction of the quark and gluon densities and hence identification of the pomeron [23].

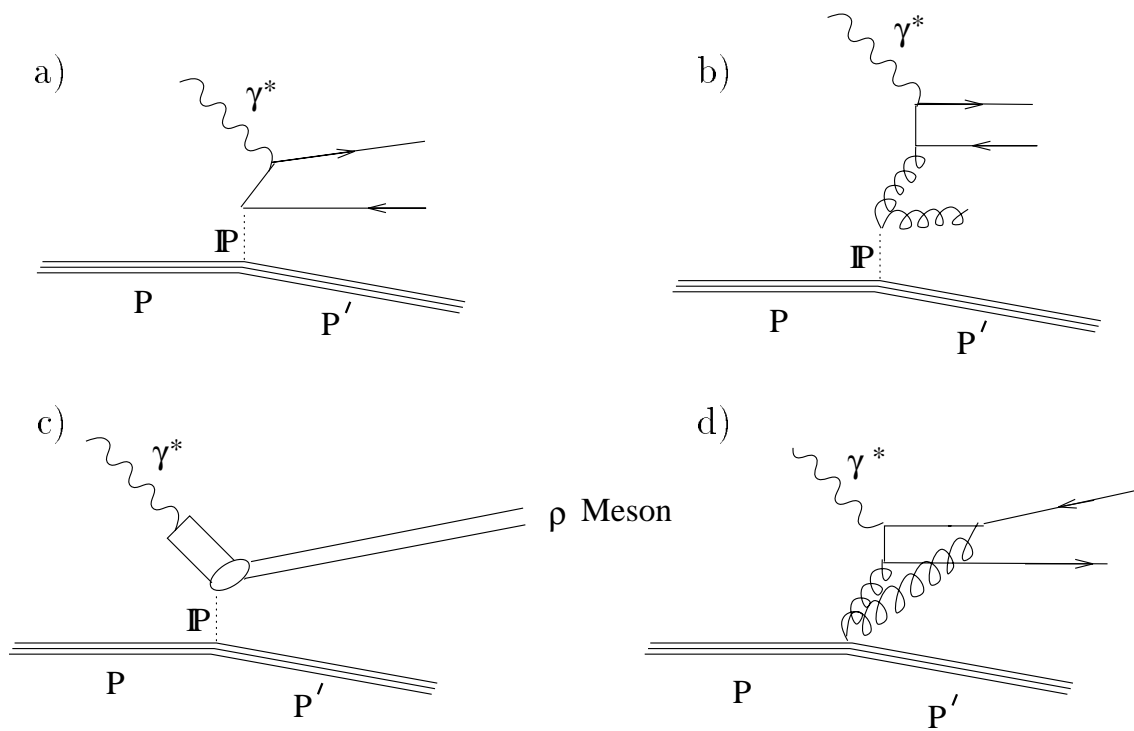


Figure 7.3: Diagrams of various possible pomeron interaction mechanisms. The virtual photon interact with: a) a quark from within the pomeron ; b) a gluon from within the pomeron; c) the pomeron directly producing a vector meson d) and higher order gluon interactions (Nicholaev-Zakharov model).

7.7 Modelling Diffraction

7.7.1 Factorisable Models

Most diffractive DIS models treat the perturbative and non perturbative vertices of the interaction separately i.e. they assume factorisation. The non perturbative part ($f_{\mathbb{P}/p}(x_{\mathbb{P}}, t)$) is then not peculiar to DIS and so it can take the form of a parameterisation of a fit to experimental (γp or pp etc.) data or a Regge Model prediction which is in agreement with data. The perturbative part ($F_2^{\mathbb{P}}(\beta, Q^2)$) is much more uncertain, with most models allowing a wide range of possibilities.

All factorisable models have similar predictions for the form of the pomeron flux: a steeply falling cross section with increasing $|t|$ and an $x_{\mathbb{P}}$ dependence such that $f_{\mathbb{P}/p} \sim 1/x_{\mathbb{P}}^n$, where n is equal to or slightly greater than 1 and very weakly dependent on t .

Berger et al. [24] and Streng [25] obtain a pomeron flux from a Regge analysis with certain parameters tuned to fit previous data. They obtained:

$$f_{\mathbb{P}/p}(x_{\mathbb{P}}, t) = 100 \frac{1}{16\pi} e^{-\frac{1}{2}4.7|t|} \frac{1}{x_{\mathbb{P}}^{1+\varepsilon-0.25|t|}}, \quad (7.9)$$

with $\varepsilon = 0.17$. Donnachie and Landshoff [27] use Regge theory and an elastic form factor for the proton to get:

$$f_{\mathbb{P}/p}(x_{\mathbb{P}}, t) = 3.5 \frac{9}{4\pi^2} \frac{4m_p^2 - 2.8t}{4m_p^2 - t} \frac{1}{(1 - t/0.7)^2} \frac{1}{x_{\mathbb{P}}^{1+\varepsilon-0.25|t|}}, \quad (7.10)$$

with the same value as Streng for ε . Ingelman and Schlein [26] use fits to data with Regge theory used only for the overall normalisation:

$$f_{\mathbb{P}/p}(x_{\mathbb{P}}, t) = \frac{1}{2.3} (6.38e^{-8|t|} + 0.424e^{-3|t|}) \frac{1}{x_{\mathbb{P}}}. \quad (7.11)$$

The pomeron structure function ($F_2^{\mathbb{P}}(\beta, Q^2)$) depends on the identity of the partonic constituents of the pomeron and how the pomeron's momentum is shared between them. All the models specify the partonic content and momentum distribution function, $G(x_p)$, at some low value of Q^2 and use pQCD evolution to predict the composition at higher Q^2 values.

Donnachie and Landshoff [27] propose the pomeron to be composed of quarks. Other models [26, 24, 25] propose a predominantly gluonic pomeron.

Many models assume that the sum of the momentum of the constituents of the pomeron adds up to the momentum of the pomeron itself i.e. the momentum sum

rule is fulfilled:

$$\int_0^1 x_p G(x_p) = 1, \quad (7.12)$$

with

$$G(x_p) = \sum_i f_i(x_p), \quad (7.13)$$

where f_i is the probability that the i^{th} parton within the pomeron carries a fraction x_p of the pomeron's momentum. It is, however, by no means clear that this relationship must hold. Indeed Donnachie and Landshoff suggest it does not [27].

If the pomeron were composed of two partons then a natural choice for a momentum distribution function that fulfilled the momentum sum rule would be a hard distribution of the form:

$$x_p G(x_p) = 6x_p(1 - x_p). \quad (7.14)$$

Donnachie and Landshoff propose a similar distribution function but take the overall normalisation from the quark densities of the proton such that:

$$x_p f(x_p) = \frac{1}{3} C \pi x_p (1 - x_p), \quad (7.15)$$

with $C=0.23$ and three quark flavours (plus three antiquark flavours) allowed, but s and \bar{s} contributing half strength so that:

$$x_p G(x_p) = \frac{5}{3} C \pi x_p (1 - x_p), \quad (7.16)$$

Berger suggests an alternative hard distribution:

$$x_p G(x_p) = (0.18 + 5.46x_p)(1 - x_p). \quad (7.17)$$

Streng argues [25] that equation 7.14 represents the hardest possible gluon density since the addition of further gluons would make the distribution softer i.e. decrease the average gluon momentum. He suggests the softest possible distribution to be similar to the gluon sea in the proton:

$$x_p G(x_p) = (1 - x_p)^5, \quad (7.18)$$

with the real distribution lying somewhere between these two limits.

7.7.2 Non Factorisable Models

Nicholaev and Zakharov suggest breaking of factorisation by higher order QCD diagrams such as 7.3.d or else by multiple pomeron exchanges [28]. They argue that the valence and sea quark distributions within the pomeron should have different x_P dependencies. The deviations are, however, small compared to the present errors of the data (see section 10.7). The model gives a maximum change in the slope of F_2^D of $\simeq x_P^{0.14}$.

7.7.3 Direct Models

Direct processes arise when the virtual photon does not resolve structure within the pomeron (i.e. interacts as a whole) and produces final states with $\beta \simeq 1$ and $M_x \simeq 0$ (see figure 7.3.c). The lowest mass final state that can be produced in a diffractive process, where the proton remains intact, is a single ρ^0 meson (π^0 production would violate spin/parity conservation). This places an upper limit on the value of β for any Q^2 . Diffractively produced ρ states along with other low mass vector mesons (ω , ϕ etc.) have been observed in high energy interactions including DIS [1].

The production of these states can be treated using pure Regge theory, since no pomeron structure is involved. The Regge theory predictions are incorporated into the Vector Meson Dominance model (VMD) [29].

7.8 Monte Carlos

Two programs are currently used by H1 that provide Monte Carlo implementation of the various diffractive models: RAPGAP [30] and DIFVM [29].

RAPGAP is used for factorisable models such as those discussed in section 7.7.1. It models the single pomeron exchange diagrams of figures 7.3.a and figure 7.3.b. Higher order gluon emission is simulated with the Colour Dipole Model (ARIADNE) [31] and hadronisation by the LUND string model [32]. So far there is no implementation of non factorisable exchanges or direct processes.

The program allows any pomeron flux factor and pomeron structure function to be chosen. Amongst the wide choice of structure functions available two have been selected that reproduce various aspects of the data well [1]. These are RAPGAP Hard Quark (RAPHQ) and RAPGAP Hard Gluon (RAPHG). Both Monte Carlos

use the Streng parameterisation of the pomeron flux (equation 7.9) and the hard pomeron structure function (equation 7.14). No QCD evolution has been used so the only diagram for the hard subprocess in RAPHQ is figure 7.3.a and that for RAPHG is the photon gluon fusion figure 7.3.b. It should be noted that the two Monte Carlos will lead to different measured structure functions. In RAPHQ the virtual photon interacts directly with one of the constituent quarks so $\beta \equiv x_p$. In RAPHG the gluon with momentum x_p must first split into a $q\bar{q}$ pair. The virtual photon interacts with one of these quarks. The momentum of the struck parton β is now less than x_p . Hence RAPHQ has $F_2^P \sim \beta(1 - \beta)$ whereas RAPHG has a softer distribution.

DIFVM is used to produce direct process (figure 7.3.c) resulting in a vector meson in the final state. The model produces an admixture of $\rho(770)$, $\omega(783)$ and $\phi(1020)$ vector meson states. The mixture along with the y and Q^2 dependence is taken from fits to data from other experiments. An overview of the model together with a comparison with H1 data is given in [1].

Monte Carlos of RAPHQ, RAPHG and DIFVM have been produced that include a full simulation of the events through the H1 detector.

Chapter 8

Selection of DIS Events

8.1 Introduction

The DIS events at H1 are classified into two groups depending on where the scattered electron was reconstructed. The low Q^2 ($7.5 \text{ GeV}^2 < Q^2 < 80 \text{ GeV}^2$) sample is defined as those events where the electron was found in the BEMC, the high Q^2 ($Q^2 > 100 \text{ GeV}^2$) sample in the LAC. All the data presented in chapters 9 and 10 are (because of the higher statistics) for the low Q^2 sample. It is the selection of these events that is described here.

8.2 Event Shape

The cross section for DIS is approximately proportional to y/Q^6 or $1/\cos^6(\theta_e/2)$, where θ_e is the scattered electron angle. Thus the scattered electron predominantly travels backwards in the detector with θ_e decreasing for increasing Q^2 .

The hadronic final state can be divided in two parts: the current jet and target¹ or remnant jet. The current jet is formed from hadronisation about the direction of the struck parton and the target jet from the hadronisation of the other partons from the proton. The term ‘jet’ is somewhat misleading, since the current jet is not always resolved by standard jet finding algorithms and, since there may be substantial activity in the region between the two jets, the boundary between the jets might not be well defined.

In the detector the large boost in the proton direction means that the target jet

¹The term target jet is an historical name derived from usual DIS experiments when the source of protons was a fixed target

travels down the beampipe and is not reconstructed in the main detector (although see chapter 9 for experimental methods of probing the target jet using the forward detectors). The current jet generally does pass into the main detector and is well reconstructed by the calorimeters.

8.3 Reconstruction of x , y and Q^2

At H1 the electron vector (k' in figure 1.1) and the hadronic final state (p') are well measured. It is thus possible to measure x and Q^2 solely from the hadrons, solely from the electron or from a combination of both. A large variety of combination methods are possible, many of which result in an improvement of the resolution in x or Q^2 . A detailed discussion of the electron only method, the hadron only method and various combination methods is given in [33]. Two of these methods are described here: the electron only method and the sigma method.

The kinematic variables for the electron only method can simply be obtained by converting equations 1.8– 1.10 into LAB coordinates:

$$y_e = 1 - \frac{E'}{E} \sin^2 \frac{\theta_e}{2} \quad (8.1)$$

$$Q_e^2 = 4EE' \cos^2 \frac{\theta_e}{2} \quad (8.2)$$

$$x_e = \frac{Q^2}{4y_e EP} \quad (8.3)$$

where E is the initial electron energy, E' the scattered electron energy, P the initial proton energy and θ_e the scattered electron angle.

The electron only method gives very good resolutions in Q^2 ($\simeq 10\%$) over the full acceptance range of the BEMC. The y resolution is good at high y but deteriorates rapidly as $y \rightarrow 0$, because of the y_e in the denominator:

$$\frac{\sigma(y_e)}{y_e} \simeq \frac{d\sigma(E')}{E'y_e}. \quad (8.4)$$

At high y the measurements are made difficult because of the effects of large Initial State Radiation (ISR). These limitations restrict the range over which reasonable structure functions can be measured to $0.05 < y < 0.6$ [34].

The sigma method combines hadronic and electron information in a way that not only improves the y resolution at low y but also substantially decreases the effects of ISR.

In the sigma method the initial state electron energy (E) in equations 8.2—8.3 is replaced a value (E_{rec}) reconstructed from the final state. From energy and p_z conservation:

$$2E_{rec} = \sum_h (E_h - p_{zh}) + E' - p_{ze} = \Sigma + E'(1 - \cos \frac{\theta_e}{2}), \quad (8.5)$$

where $\Sigma = \sum_h (E_h - p_{zh})$ is summed over all hadrons reconstructed in the main calorimeter. It should be noted that Σ is reconstructed rather well since those hadrons lost down the forward beam pipe have a small $E_h - p_{zh}$ and so do not contribute greatly. Replacing E with E_{rec} the kinematic variables become:

$$y_\Sigma = \frac{\Sigma}{\Sigma + E'(1 - \cos \theta_e)} \quad (8.6)$$

$$Q_\Sigma^2 = \frac{E'^2 \sin^2 \theta_e}{1 - y_\Sigma} \quad (8.7)$$

$$x_\Sigma = \frac{E' \cos^2 \frac{\theta_e}{2}}{P y_\Sigma} \quad (8.8)$$

The y resolution is now good even at low values since:

$$\frac{\sigma(y_\Sigma)}{y_\Sigma} \simeq y_\Sigma \frac{d\sigma(E')}{\Sigma}. \quad (8.9)$$

y now appears in the numerator rather than the denominator. The method allows reasonable measurements to be made in the range $0.01 < y < 0.7$ [35]. The upper limit is made to suppress photoproduction background, where an energetic hadron fakes an electron cluster in the BEMC.

In those events with ISR the radiated photon will almost always be lost down the backward beam pipe and so E_{rec} is the energy the electron has just before it interacts with the proton. Hence the reconstructed kinematic quantities (Q_Σ^2 and y_Σ) are nearer the ‘true’ values than those assuming the full electron energy (Q_e^2 and y_e). This leads to an overall reduction in radiative corrections from up to $\simeq 20\%$ using the electron only method to $\simeq 3\%$ for the sigma method [35].

8.4 Event Selection

A low Q^2 DIS event is selected on the basis of a coincidence of a well measured electromagnetic cluster in the BEMC and a hit in the BPC. Further cuts are introduced to remove backgrounds, which mainly arise from photoproduction and beam gas/wall events. Final cuts are made to restrict the data to regions where the DIS kinematic quantities (x , Q^2 and y) have reasonable resolutions.

8.4.1 Detector Cuts

- $DCLBP < 4$ cm — Cut placed on the distance between the centre of the cluster in the BEMC and extrapolation of the track defined by the BPC hit and the reconstructed vertex. This ensures that the cluster and BPC hit were due to the same particle.
- $ECRA < 4$ cm — An electron will produce a cluster in the BEMC over a localised region, unlike hadrons for which the cluster is generally more spread out. Thus to minimise the possibility that a hadron from other processes (mainly photoproduction) fakes an electron, a cut of 4 cm on the transverse size of the BEMC cluster is made.
- $|XCL| > 13$ cm AND $|YCL| > 13$ cm — This cut removes BEMC clusters whose centres lie near to the triangular shaped stacks close to the beam pipe (see figure 2.3). The ‘triangles’ have been shown [34] not to be well described by Monte Carlo.
- $RVTX < 3$ cm — A vertex must be reconstructed in the inner trackers within 3 cm of the nominal beam line. This cut therefore requires at least one well reconstructed track. Requirement of a vertex greatly reduces non collision background.
- -35 cm $< ZVTX < 25$ cm — The z position of the vertex at the distance of closest approach must lie within values of the nominal interaction point consistent with the spread in the vertex due to the length of the proton bunch. This requirement further reduces non collision background.
- $RVHIT > 0.16$ — RVHIT is the ratio of the total number of hits in vertex constrained tracks to the total number of hits in all tracks. This cut further reduces non collision background.

8.4.2 Kinematic Cuts

- $173^\circ < \theta_e < 156^\circ$ — Limits the reconstructed electron angle so that the whole electron cluster is within the BEMC.
- $Q^2 > 7.5$ GeV² — Limits the reconstructed Q^2 to values that are well reconstructed.
- $0.03(0.05) < y < 0.7(0.6)$ — Limits placed on the reconstructed y for the sigma method (electron method). The limits represent the range in which y is

well reconstructed and does not suffer from large photoproduction background or radiative corrections. It should be noted that the lower limit for the sigma method is higher than the value quoted in section 8.3. The reason for this is that some of the Monte Carlos used to compare and correct data presented in this thesis were simulated primarily for purposes that did not require low y data. Events with $y < 0.023$ were not simulated to save on computer time.

Chapter 9

Selection of Diffractive Events

9.1 Introduction

Diffractive events have traditionally been distinguished from their ‘standard’ non-diffractive counterparts by the observation either of an elastically scattered proton and/or of a rapidity gap characteristically larger than for standard events. The present H1 detector has no means of identifying the elastically scattered proton – it is almost always lost down the beampipe¹. The method chosen to select diffractive events, therefore, is to look for a rapidity gap between the proton remnant (which would of course be a single proton in the elastic case) and the current jet.

Diffractive events were originally sighted at ZEUS [36] and H1 [1] by examination of energy deposits in the main calorimeter. A plot of the rapidity of the most forward detected deposit of energy greater than 400 MeV, η_{max} , (as shown in figure 9.1), shows a long tail extending to smaller values than those expected for ‘standard’ non diffractive events. η_{max} represents the rapidity of the border between the current jet and the gap. Standard events generally have an η_{max} very close to the edge of the acceptance of LAC. Diffractive events are classified as those with $\eta_{max} < 1.8$.

The calorimeter η_{max} cut offers a useful method of selecting a clean sample of diffractive events (Monte Carlo estimates are that non diffractive background contribute $\simeq 7\%$) using very well understood detectors. It does, however, suffer from the drawback that many diffractive events are lost and furthermore these are not evenly distributed in the important diffractive kinematic variables as can be seen in figure 9.8. It was in an attempt to access the high x_P and high M_X region that a new diffractive event selection was devised. This involved extending the range

¹although the first station of a forward proton spectrometer (allowing tagging and energy measurements) is installed and taking data for 1994 running

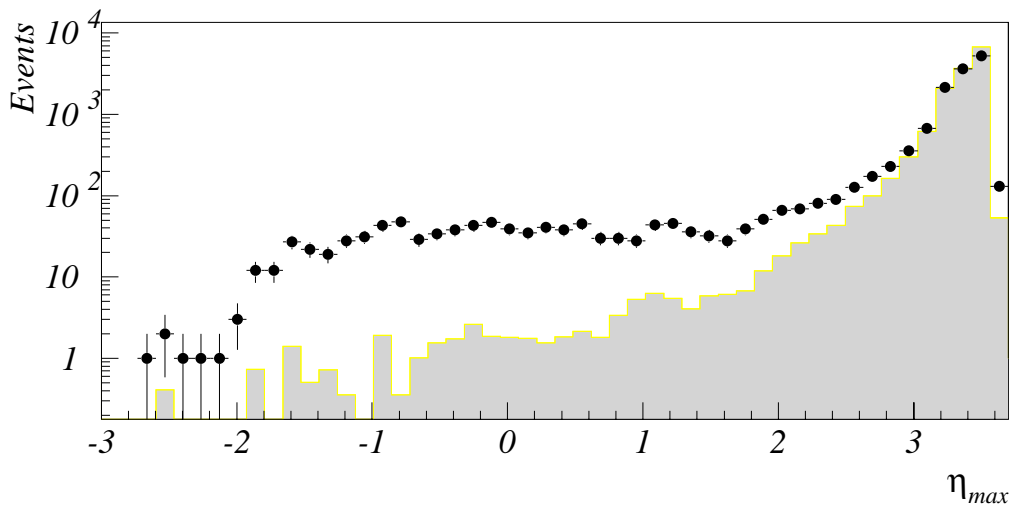


Figure 9.1: The η_{max} distribution for the data (closed circles) and for standard DIS Monte Carlo (CDM) shaded.

of particle detection to higher rapidity than the edge of LAC using the ‘forward detectors’ of PLUG, FMD, IRON (the instrumentation in the return yoke) and PTAG and so enabling diffractive events with much smaller gaps to be tagged. This chapter explains the operation of the forward detectors when used to tag diffractive events. Reconstruction techniques are described, a Monte Carlo comparison with the data is given and the cuts used in the final diffractive event selection with their acceptances and backgrounds are given.

9.2 Tagging Diffractive Events Experimentally

For an effective diffractive event selection by means of a rapidity gap two objectives must be pursued: the selection must have as large an efficiency as possible for accepting diffractive events and at the same time efficiently reject standard events. Optimisation can be achieved by varying not only the size of the rapidity gap, but also its position in pseudorapidity. As shown in figure 9.2 diffractive events with a proton remnant typically have a low particle multiplicity in the range $5 < \eta < 6$, those without a proton remnant have a low multiplicity in the range $5 < \eta < 8$, whereas the non diffractive events have large multiplicity for all $\eta < 8$.

The H1 detector has the capability of detecting particles up to a rapidity of 8 as

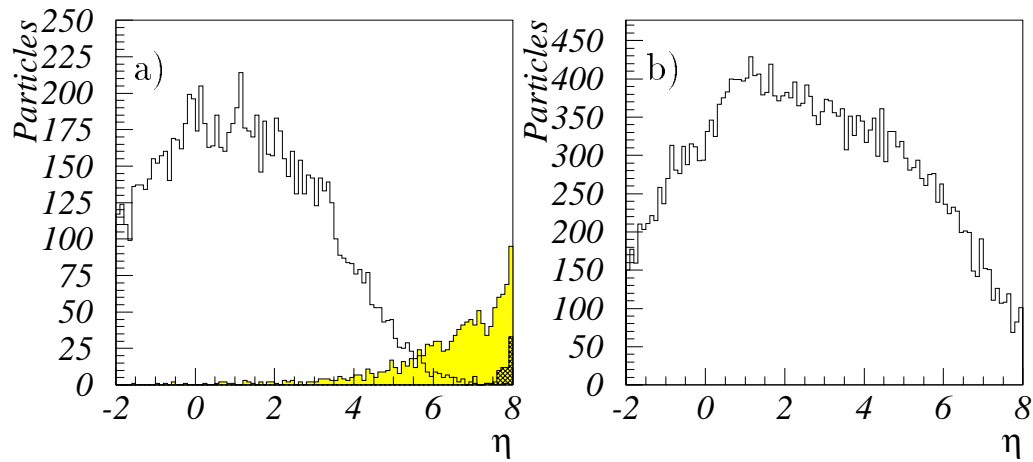


Figure 9.2: The distribution of particles as a function of pseudorapidity as obtained from: a) the diffractive Monte Carlo, with the solid line indicating particles from the current jet, dark shade the elastically scattered protons and light shade particles arising from dissociated protons; and b) the DIS Monte Carlo (CDM).

shown in figure 9.4. By use of the BEMC, LAC and the forward detectors (PLUG, FMD, IRON and PTAG) all of the rapidity interval from -2.8 (173°) to $+7$ (0.1°) is covered with a minimum single particle detection efficiency of 20%. It is evident therefore that the best possible event selection should include as many of the forward detectors as possible (with the possible exception of PTAG) and as large an η_{max} as possible.

9.3 Detection of High Rapidity Particles using the Forward Detectors

Figure 9.3.a shows a typical DIS event where there is no evidence of any rapidity gap. It can be seen that there is much forward activity, with energy deposits in the PLUG, IRON and the very forward parts of LAC along with hits in the FMD and IRON. The observed signals arise in two ways. Either a primary particle from the interaction passes into the detector or else the primary particle passes inside the beam pipe until it collides with some material (the beam pipe wall, a collimator, a quadrupole magnet etc.). This collision generally produces a shower of secondaries, some of which have large angles to the beam and so can pass into a detector. It is

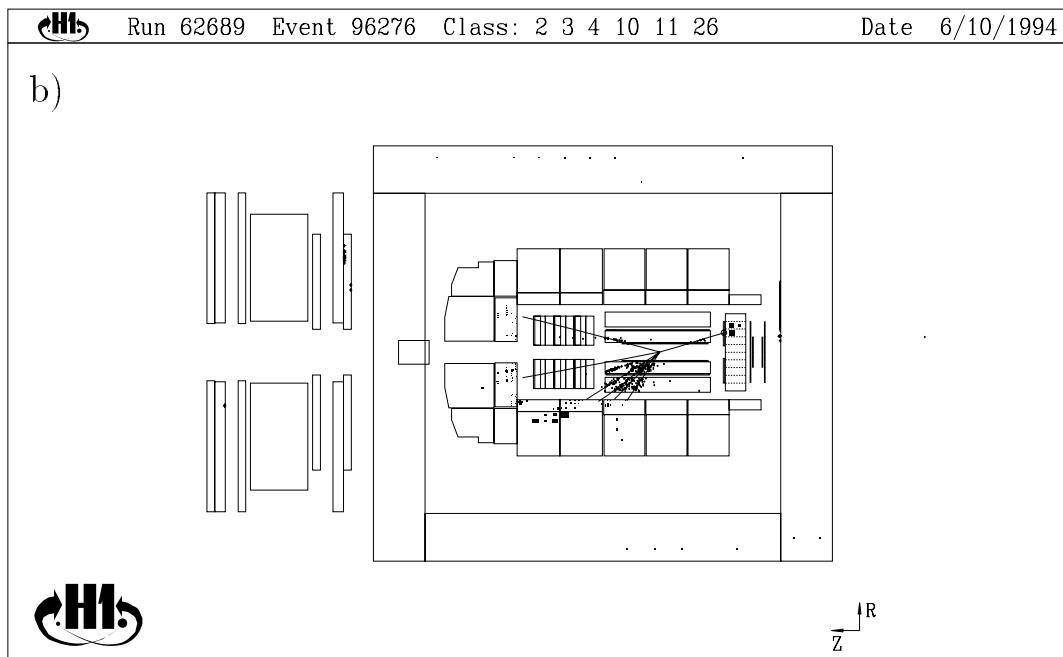
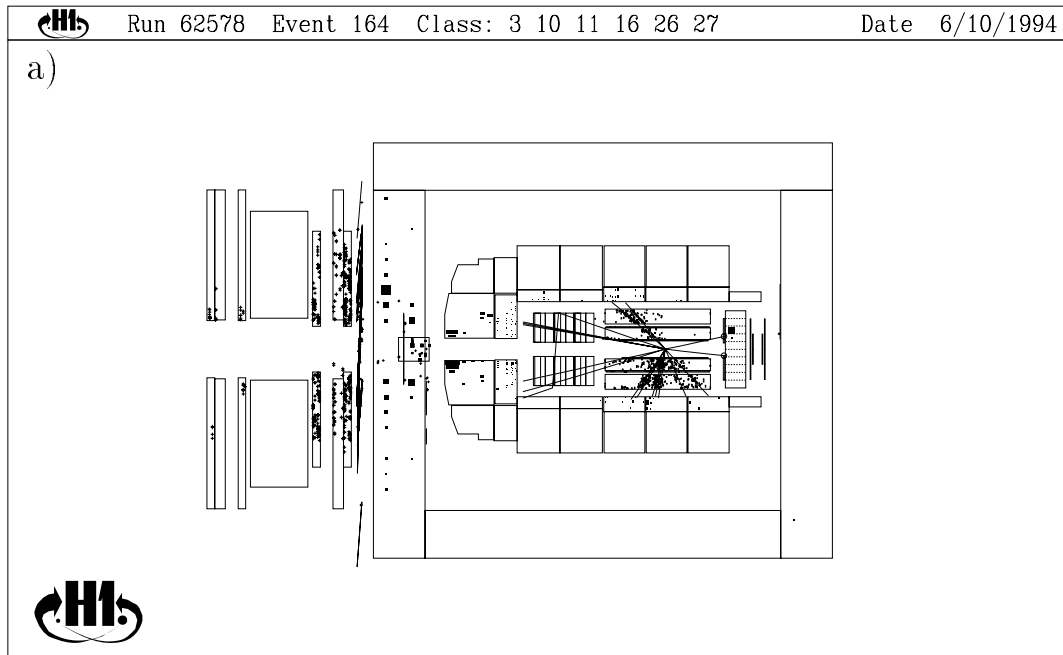


Figure 9.3: Two DIS events: a) shows large deposits of energy in the forward region, indicating a standard DIS event; b) shows little energy in the forward region and is thus selected as a diffractive candidate.

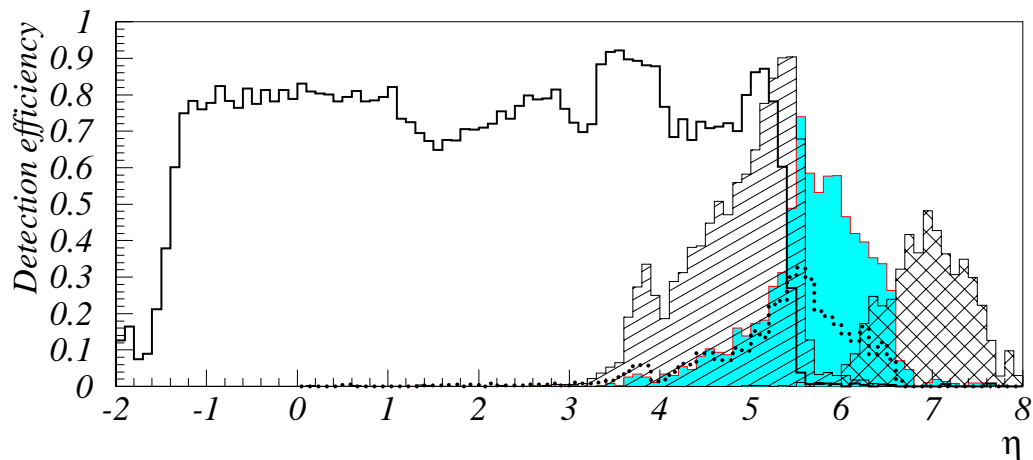


Figure 9.4: The single particle detection efficiency for various subdetectors as obtained from standard DIS Monte Carlo (MEPS): solid line is the LAC, diagonal lines is the PLUG, shaded is the FMD, dotted line is the IRON, cross hatched is the PTAG.

the detection of these secondaries that allows the forward detectors to probe very high rapidity.

By contrast a DIS diffractive candidate is shown in figure 9.3.b. In this case there is very little activity in all the forward detectors implying that there is a rapidity gap from the most forward LAC cluster ($\eta = 2.8$) to $\eta \simeq 7$.

9.3.1 Reconstruction of Signals in the Forward Detectors

The signals from the forward detectors must be reconstructed in such a way as to maximise the chances of detecting particles and minimise the possibilities of obtaining a fake signal caused by noise in the detectors.

The particle flux through the FMD is almost entirely from secondaries since it is well shielded by the IRON and LAC and the flux of muons is very small. The FMD suffers only slightly from noise ($\simeq 0.005$ hits per cell per event). The noise is thought to arise mainly inside the electronics of the readout system. Hits from a charged particle can easily be distinguished from noise hits since a charged particle will usually give a hit in both sublayers of a layer, whereas noise is randomly distributed. It has been found that reconstruction up to the pairing level is sufficient

to almost entirely get rid of noise hits. Pairs are defined as any two hits found in each sublayer of a layer that are separated by no more than 9 cm in the drift coordinate (Y)². Further constraints are that a hit cannot be used to make more than one pair and no more than one hit from each cell can be used. The latter constraint is introduced because a single pulse of irregular shape (which is not described by the Monte Carlo) can give rise to more than one reconstructed hit. There is little to be gained from attempting to use the separation of the layers in Z to access different regions of rapidity so the total number of FMD pairs is summed, N_{FMD} . It should be noted that reconstruction up to the segment level is also possible, but will necessarily reduce efficiency since particles are not geometrically constrained to pass through more than one layer.

No non standard reconstruction was found to be necessary for the PLUG. After noise suppression the signals are converted into an energy measurement per channel. Since the PLUG occupies a small bite in rapidity no attempt has been made to use the PLUG's segmentation. Instead the total PLUG energy is taken, E_{PLUG} .

The IRON has both tracking and calorimetric capabilities. It is the tracking that is of more use for the present purposes, since secondaries are found to have very low energies and so can produce a hit without significant energy deposits over background levels. No attempt has so far been made to reconstruct the hits in the muon chambers of the IRON into segments. Instead the total number of hits found in the forward iron endcap is summed, N_{IRON} .

PTAG suffers from almost no noise. It is therefore sufficient to sum the total number of scintillators that fire, N_{PTAG} .

9.3.2 Determination of Residual Noise

As explained in the previous section efforts have been made to ensure that the reconstructed quantities are as free from noise as possible. There will still, however, be a residual amount of noise left after reconstruction. This section explains how this residual level is determined and what lower limits placed on the reconstructed quantities to distinguish between a signal consistent with noise and one consistent with particle detection.

The amount of noise for each detector was found using a random trigger which coincided with a filled electron and proton bunch. The chance of a collision or beam

²This is a looser cut than that used for muon reconstruction (see section 3.5.3) since these secondaries can have much larger angles than muons from the interaction

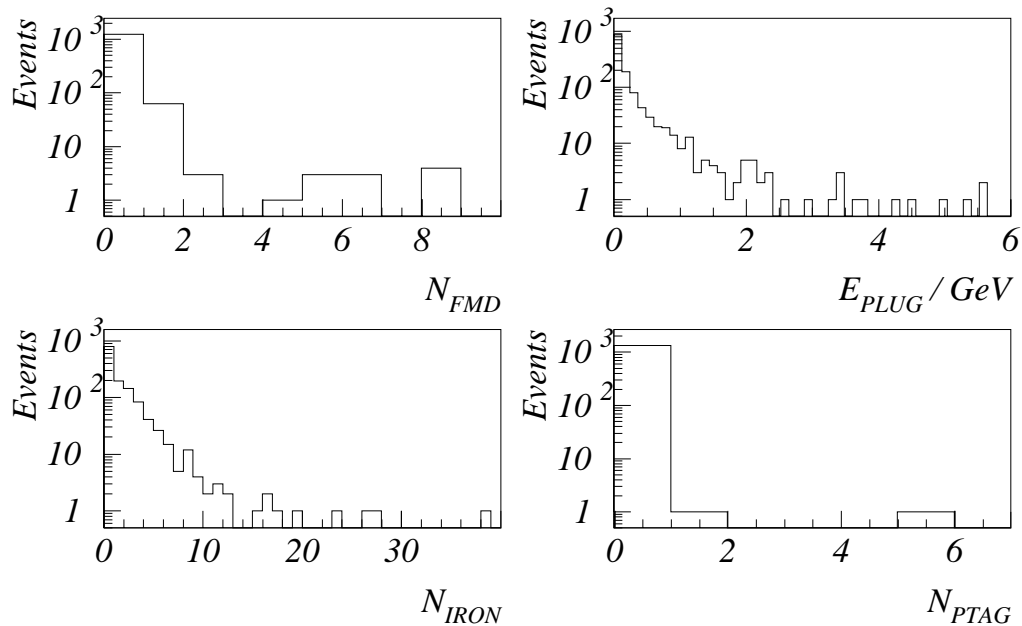


Figure 9.5: Signals as recorded by the forward detectors for 1329 random trigger events

gas event in this sample is very small. The results can be seen in figure 9.5. On the basis of these plots the following cuts were made to distinguish between a signal consistent with noise and a signal consistent with detection of particles from the interaction (secondary or primary). At least one particle is defined to be have been detected in an event if:

$$\begin{aligned}
 E_{PLUG} &> 1 \text{ GeV} && \text{OR} \\
 N_{IRON} &> 5 && \text{OR} \\
 N_{FMD} &> 1 && \text{OR} \\
 N_{PTAG} &> 0
 \end{aligned}$$

These cuts will not, however, completely remove noise. Table 9.1 shows the chance of misidentifying events of a sample consisting totally of events where no particle travelled in the forward region for each of the cuts.

Noise is added to Monte Carlos by adding the signal obtained from a random trigger real data event to the signal obtained from the Monte Carlo.

Cut	Fraction
$E_{PLUG} > 1 \text{ GeV}$	0.055
$N_{IRON} > 5$	0.040
$N_{FMD} > 1$	0.016
$N_{PTAG} > 0$	0.002

Table 9.1: The fraction of events in which a signal would be obtained from noise alone for each of the cuts given. Data used was a sample of 1329 random trigger events

9.4 Monte Carlo Comparison

It is important to check that the forward detectors are well described by the Monte Carlos, since any physics analysis will rely on Monte Carlos to unfold acceptances and backgrounds. Large signals are to be expected from standard DIS events so it is with this event class that Monte Carlos are compared. An inference that diffractive events are also well described is then made.

Discrepancies between the data and the standard DIS Monte Carlos can arise because of three main reasons: the simulation of the subdetector or surrounding region may be inadequate; the underlying physics of the Monte Carlo may not describe the data; or the background events (including diffractive events) have been treated incorrectly. An attempt has been made to quantify the effect of each of these possibilities by varying the sophistication of the simulation; using two independent DIS models; and substantially changing the diffractive-non diffractive Monte Carlo mix.

9.4.1 Forward Beampipe Region Simulation

There are two versions of the simulation code (H1SIM) considered here: versions 3.01 and 3.03. Version 3.03 is a better approximation to the actual beampipe than 3.01, with many omissions included. A comparison of results obtained with each version is useful to understand what effect non perfect simulation has on the efficiencies of the forward detectors.

Version 3.01 simulates the forward detectors and their very near surroundings very well. There are however several omissions. A collimator forward of the PLUG (C3), one inside the FMD (C2) and one forward of the FMD (C1) are not included. The collimators are pieces of metal inserted into the beampipe to protect the H1 de-

tector from synchrotron radiation from the electron beam. They include mechanics (to allow movement in and out of the beam) and are surrounded by lead shielding. A constriction in the beam pipe in the region of C3 is absent and the beampipe wall for a length of about 10 cm near C2 is missing (probably due to an error in the simulation code).

Version 3.03 includes descriptions of the collimators C2 and C3, their casings, the lead shielding and missing the beam pipe. Collimator C1 is, however, still not present.

9.4.2 DIS Models

The two main non diffractive DIS Monte Carlos used by H1 are compared in this analysis: the Colour Dipole Model (CDM) [37] and the Matrix Elements plus Parton Showers (MEPS) [38]. Both have been constrained to fit the structure function $F_2(x, Q^2)$ as measured by H1 from 1993 data (the MRSH' parameterisation) [39].

9.4.3 Control Plots

Plots of the reconstructed signals of each detector are shown in figures 9.6 and 9.7 for a sample of data where it is expected that there is little diffractive contribution. From these it can be seen that the FMD is well described by both models. The PLUG can be well described if a constant energy scale factor is introduced³ by the CDM Monte Carlo, but even with the scale factor MEPS shows too many events with low energy. This result is expected since energy flow measurements with the LAC [40] show that the MEPS Monte Carlo produces about 50 % too little energy in the forward region, whereas CDM describes the energy flows quite well. The IRON is not well described by the Monte Carlo: there are far more hits in data than in either Monte Carlo. PTAG shows a fairly large deviation from the data.

9.4.4 Detector Efficiencies

In an attempt to quantify the level of agreement between Monte Carlo and data an efficiency for the rejection of standard DIS events has been calculated for each detector, making use of correlations between detectors (i.e. comparisons of the rate at which one detector gives a signal compared to two detectors simultaneously giving

³This is to be expected since no test beam calibration has been performed on the PLUG so the energy scale used in the Monte Carlos is to some extent arbitrary.

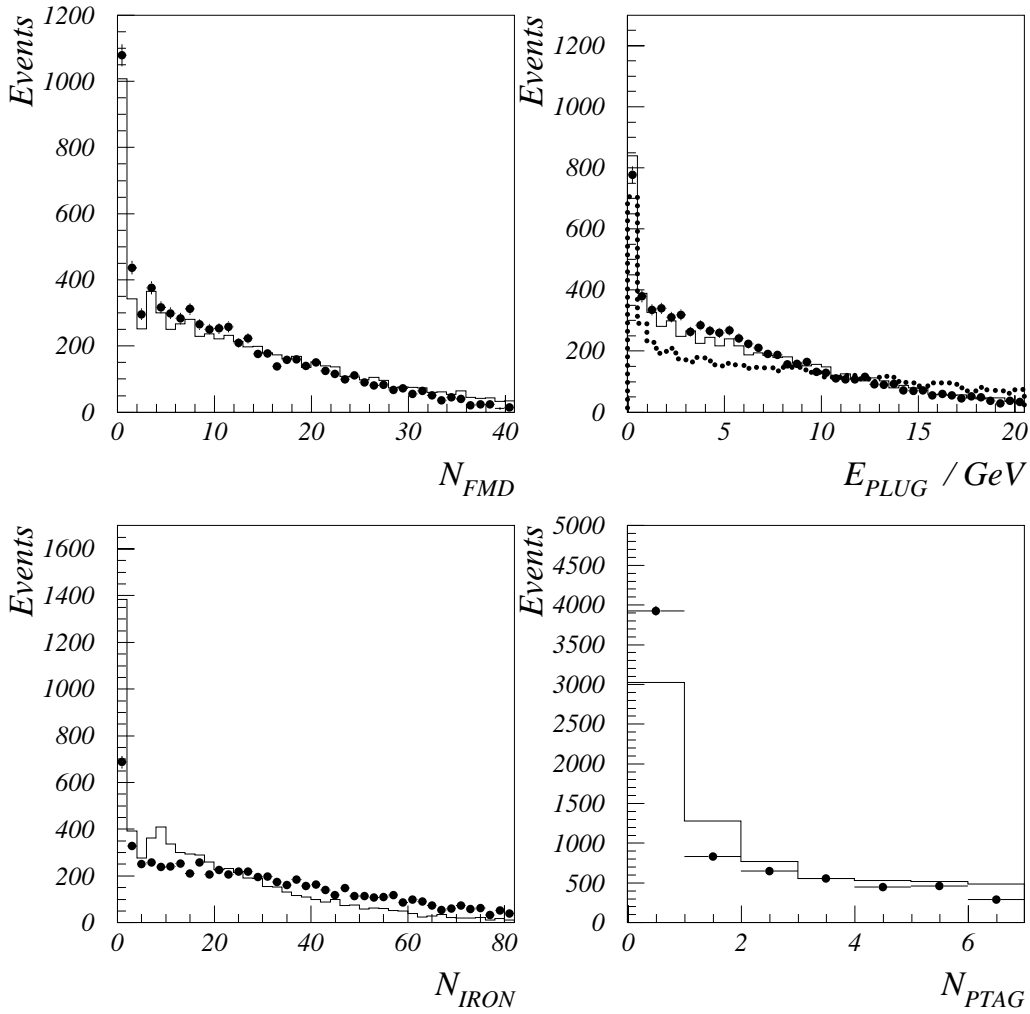


Figure 9.6: Comparison of data with CDM (SIM 3.03). The closed circles are data points. The solid line is Monte Carlo data. The PLUG energy is shown rescaled by a factor of 0.6 (solid line) and not rescaled (dotted line). The data were selected using the sigma method of event selection with the additional cut of $\eta_{max} > 3.2$ to suppress diffractive events

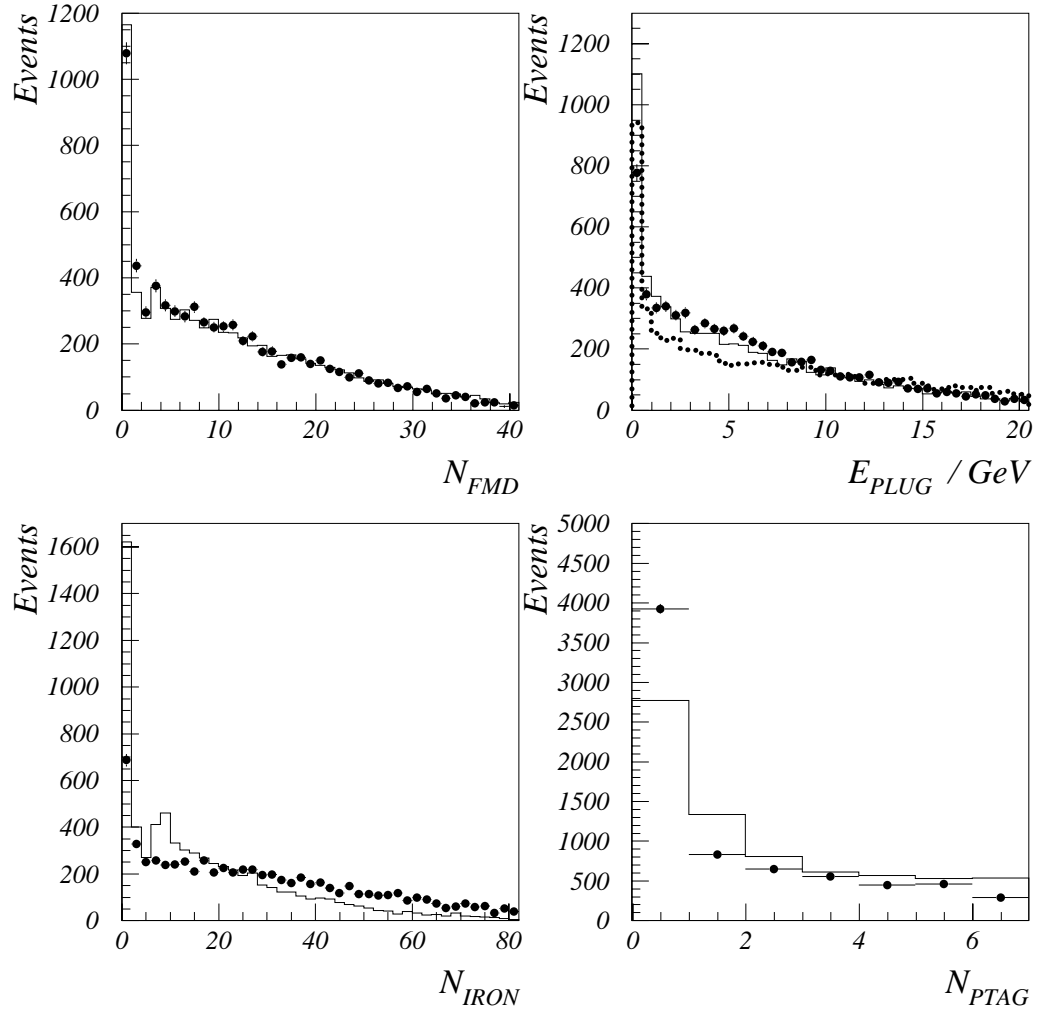


Figure 9.7: Comparison of data with MEPS (SIM 3.03). The closed circles are data points. The solid line is Monte Carlo data. The PLUG energy is shown rescaled by a factor of 0.6 (solid line) and not rescaled (dotted line). The data were selected using the sigma method of event selection with the additional cut of $\eta_{max} > 3.2$ to suppress diffractive events

signals). A procedure has been used to allow the fraction of diffractive events to vary as a free parameter. The method gives several reasonably independent measures of efficiency for each detector. It should be noted that the efficiencies are only valid for the reconstruction cuts given in section 8.4. They will certainly vary with x_{BJ} , Q^2 . Their usefulness lies in that a perfect Monte Carlo would give the same efficiencies as the data. Any disagreements must be put down to Monte Carlo inadequacies.

A full explanation of the technique is described in appendix A. A summary of the results are shown in table A.1. The results show that the method of extraction of the efficiencies is independent of the Monte Carlos used as an input (either the model, the sophistication of the simulation or the diffractive proportion).

The Monte Carlo efficiencies for the PLUG, FMD and LAC are in good agreement ($\leq 5\%$) with the data for all model/simulation combinations. The only exception is the FMD which shows a slightly higher efficiency for SIM 3.01. A separate investigation has shown that this effect is wholly due to the absence of the 10 cm section of beam pipe in SIM 3.01, which gave low energy particles a greater chance of escaping into the FMD. The addition of the collimators makes little difference to the overall efficiency. As indicated by the control plot (figure 9.6) rescaling the PLUG energy by 0.6 gives a better agreement for CDM, although for MEPS the disagreement is worst. The scale uncertainty in LAC (25% at 400 MeV) has little effect on the efficiencies.

The other two detectors (IRON and PTAG) do not seem so well described by the Monte Carlos. As would be expected from observation of the control plot, large differences between the efficiencies for data and Monte Carlo were found. These differences do not significantly alter by a change in DIS model and so would seem to indicate that there is an inadequacy in the simulation of the detectors. This supposition can be further supported for the IRON since it covers a similar rapidity interval as some of the other forward detectors, which do not see any excess. The supposition for PTAG, having no other detector near, is less certain, especially since the theoretical uncertainties are substantial in the target jet region.

9.5 Final Selection

It is now possible to summarise the results of this chapter by giving a set of diffractive event selections. For the reasons given in the previous section the IRON is not well described by the Monte Carlos so is not used in the final selection cuts. PTAG is slightly better described, although not perfectly. It is included in the selections

since it is unique amongst the detectors in allowing a measurement of the fraction of events with proton dissociation. Whenever it is used a systematic uncertainty of 15% in its efficiency should be incorporated into any physics analysis.

Each selection has its advantages and disadvantages and no one is suitable for all types of physics analysis. The variation in the acceptance of each of the cuts as a function of several kinematic quantities is shown in figure 9.8 and the estimated fraction of non diffractive background is shown in table 9.2. The acceptances were estimated using the diffractive Monte Carlo mix of section 10.4. The backgrounds were estimated by taking the fraction of the number of events obtained from data to that obtained from the standard DIS Monte Carlo for each diffractive selection, with the Monte Carlo normalised to the data for $\eta_{max} > 3.2$. It is recommended that CDM should be used to estimate the standard DIS background and the uncertainty in the DIS background estimated by taking the difference between the backgrounds obtained from MEPS and CDM. The selections are as follows:

- ETAM – $\eta_{max} < 1.8$
- FWDA – $\eta_{max} < 3.2$ AND
 $N_{FMD} < 2$ AND
 $E_{PLUG} < 1 (0.6) \text{ GeV}$
- FWDA* – $\eta_{max} < 3.2$ AND
 $N_{FMD} < 2$ AND
 $E_{PLUG} < 1 (0.6) \text{ GeV}$ AND
 $N_{PTAG} < 1 (2)$
- FWDB* – $N_{FMD} < 2$ AND
 $E_{PLUG} < 1 \text{ GeV}$ AND
 $N_{PTAG} < 1 (2)$

where the brackets indicate the values to be taken for Monte Carlo data to partially correct for the apparent scale difference in the PLUG energy and the observed efficiency difference for PTAG. The selections marked with an asterisk (i.e. those including PTAG) are used to anti-select events in which the proton dissociates. The non asterisked selections are used to select a complete sample of diffractive events.

Selection	CDM	MEPS
ETAM	0.07	0.11
FWDA	0.18	0.25
FWDA*	0.17	0.21
FWDB*	0.34	0.40

Table 9.2: The estimated fraction of standard DIS background for the various diffractive selections. Data were selected using the electron method.

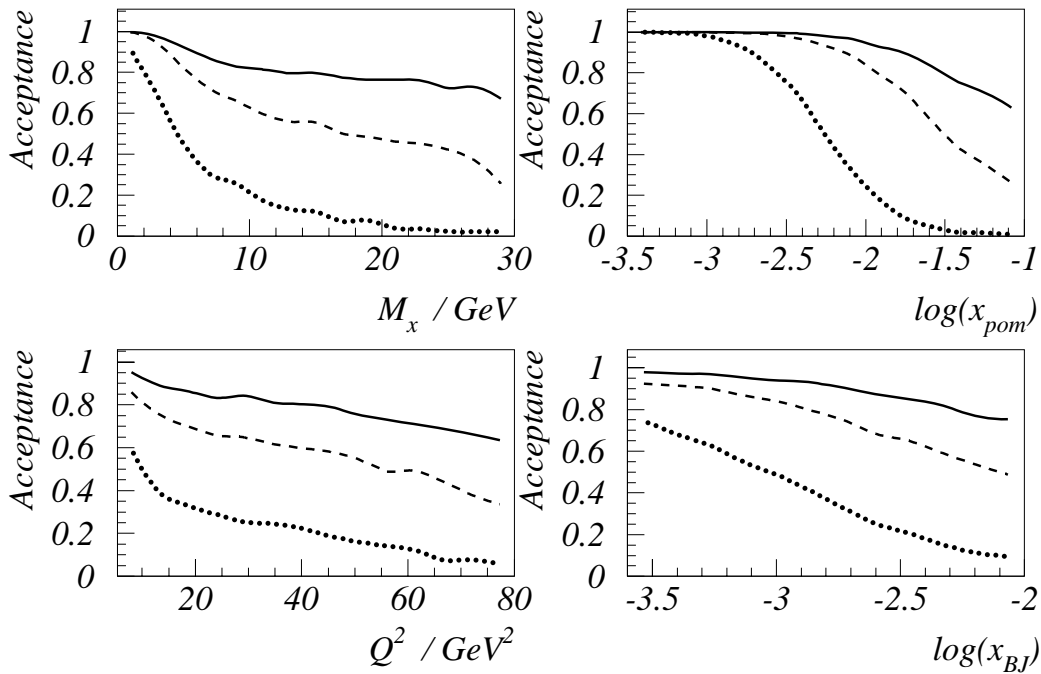


Figure 9.8: Acceptance estimated using a diffractive Monte Carlo mixture without proton dissociation. Solid line is selection FWDB*, dashed line is FWDA, dotted line is ETAM.

Chapter 10

Measurement of the Diffractive Proton Structure Function

10.1 Introduction

The measurement presented in this chapter is not for the full structure function but restricted to $\int F_2^D(x, Q^2; x_P, t) dt$, which for reasons of brevity shall be written as $F_2^D(\beta, x_P, Q^2)$. With the present apparatus it is not possible to detect the elastically scattered proton and so t cannot be determined. It might be suspected that the 4-momentum of the proton could be inferred by a measurement of the remaining system (the scattered electron and hadrons) but, since the energy loss of the proton is generally much less than the energy resolution of the detector, such a measurement gives virtually no information about t .

The structure function is obtained by converting the measured cross section using equation 7.6 which, after integration over t , becomes:

$$\frac{d^3\sigma(x_P, x, Q^2)}{dx_P dx dQ^2} = \frac{4\pi\alpha^2}{xQ^4} \left(1 - y + \frac{y^2}{2(1+R)}\right) F_2^D(\beta, x_P, Q^2) \quad (10.1)$$

or via a Jacobian transformation:

$$\frac{d^3\sigma(\beta, x, Q^2)}{d\beta dx dQ^2} = \frac{4\pi\alpha^2}{\beta^2 Q^4} \left(1 - y + \frac{y^2}{2(1+R)}\right) F_2^D(\beta, x_P, Q^2) \quad (10.2)$$

As yet there is no experimental information or theoretical calculations of R for diffractive DIS. For this reason R is set to zero for all x , Q^2 and β . Once R has been measured or calculated it will be straightforward to convert the measurement presented here. It should be noted that if R turns out to be of the same order as the calculation made for $F_2^P(x, Q^2)$ [6] then the points will not change their value by more than $\simeq 5\%$ i.e. rather small when compared to the statistical errors on the measurement.

The data for this measurement were selected using the FWDB cuts defined in section 9.5 and so the structure function presented represents the total diffractive cross section (elastic proton plus proton dissociation). The data were taken in the 1993 running period for a total integrated luminosity of 271 nb^{-1} and restricted to the low Q^2 (i.e. BEMC selected) data sample.

10.2 Kinematic Variable Reconstruction

Chapter 8 describes how the standard DIS variables x and Q^2 are reconstructed. For this analysis the structure function is calculated with both the electron and sigma methods since each method has rather different systematic errors. The results from the two methods are then compared.

β and $x_{\mathcal{P}}$ are determined from the standard DIS variables and the invariant mass of the hadrons:

$$\beta \simeq \frac{Q^2}{Q^2 + M_X^2}, \quad (10.3)$$

if Q^2 is large ($> 1 \text{ GeV}^2$) and:

$$x_{\mathcal{P}} = \frac{x}{\beta}, \quad (10.4)$$

M_X is determined from information from the calorimeters (LAC, BEMC and TC):

$$M_X^2 = \sum (\mathbf{p}_c)^2 - (\sum \mathbf{p}_c)^2, \quad (10.5)$$

where \mathbf{p}_c is the 3-momentum vector of each calorimeter cluster and the sum is over all clusters apart from that belonging to the scattered electron.

10.3 Bin Selection

The diffractive cross section is determined by finding the number of events in a bin in x , Q^2 and β space. The bin measurement is then converted to a cross section at a point somewhere within the bin using a Monte Carlo with a structure function that is similar to that measured. The bins were selected to be of a sufficient size such that the level of smearing (i.e. reconstruction of the event in the wrong bin due to imperfect detector resolution) was tolerable and that there was a reasonable number of events in most bins.

The accessible range in x and Q^2 is defined by the angular coverage of the BEMC and, as explained in chapter 8, limited to those values where radiative corrections, photoproduction background and resolutions are not too large. The kinematic region is further restricted by placing an upper limit on x_P . This cut is introduced because the acceptance of the forward cuts becomes poor at large x_P as shown in figure 9.8. The complete set of kinematic cuts is as follows:

$$156^\circ < \theta_e < 173^\circ \quad (10.6)$$

$$0.03(0.05) < y < 0.7(0.6) \quad (10.7)$$

$$Q^2 > 7.5 \text{ GeV}^2 \quad (10.8)$$

$$x_P < 0.1 \quad (10.9)$$

for the sigma (electron) method. The projection of the kinematic volume onto the x - Q^2 plane is shown in figure 10.1

The kinematic volume is subdivided into bins defined with x and Q^2 limits shown in table 10.1 and the β limits shown in table 10.2. The kinematic cuts (equations 10.6-10.9) mean that some bins are non rectangular as can be seen in figure 10.1. The bins in x and Q^2 were chosen following closely those used for the 1992 $F_2^P(x, Q^2)$ measurement [6], which had a similar total number of events as the present analysis. The bins in β were chosen so as the effects of smearing were reduced to a minimum. The upper limit on β (0.8) ensures that the majority of direct ($\beta \simeq 1$) vector meson states are not selected. These events are produced as resonances and so, although the total cross section can straightforwardly be calculated, conversion to a structure function at a measured point is problematical. The small number of vector meson states that migrate into the selected bins are accounted for by the smeared acceptance correction as defined in section 10.5.3. With this selection all bins were checked with the diffractive Monte Carlo and found to have adequate resolutions in x , Q^2 and β , which for this analysis is defined to be less than the bin size. Figure 10.2 shows how the average resolutions vary as a function of each of the kinematic quantities.

The point where the structure function is quoted, the ‘bin centre’, is included in tables 10.1 and 10.2. This is chosen for each bin to be far from the bin edges and close to the point where the assumed structure function (i.e. that from the diffractive Monte Carlo) equals its mean value across the bin.

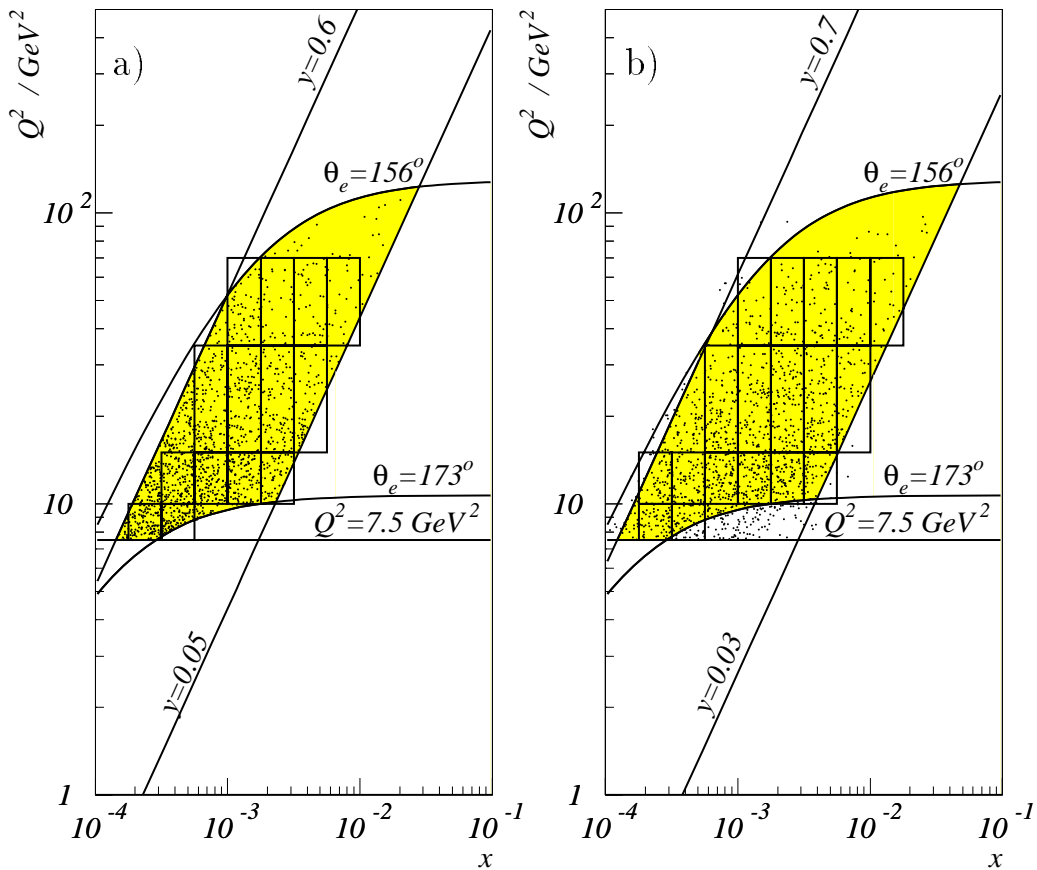


Figure 10.1: A projection of the kinematic volume onto the $x - Q^2$ plane with events selected with: a) the electron method and b) the sigma method. The shaded area is the accessible kinematic region, the boxes mark the boundaries of the chosen bins and the dots are the data points. For the sigma method the y and θ_e boundaries denote the case when the reconstructed initial electron energy is equal to the nominal beam energy.

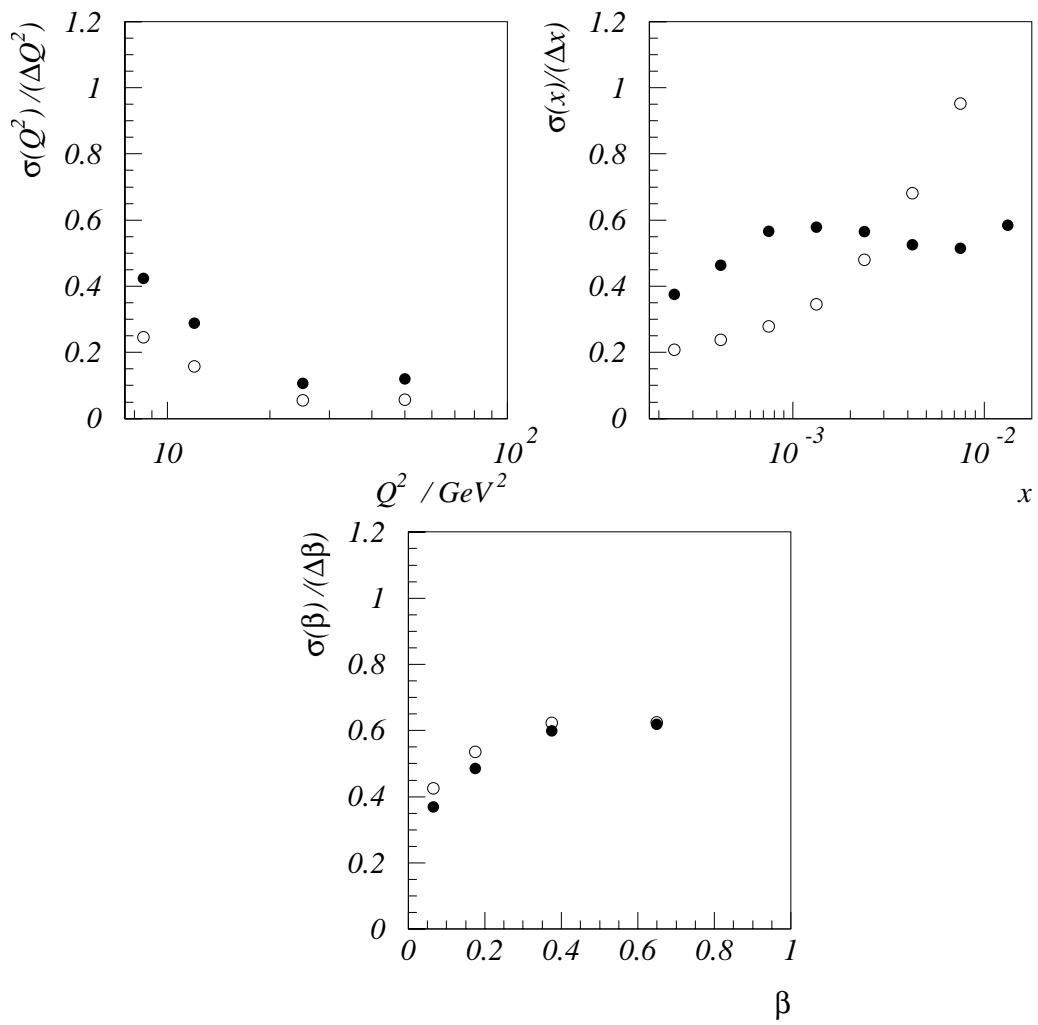


Figure 10.2: Resolutions as a fraction of the bin size. Open circles are for data selected using the electron method and closed circles are for the sigma method. ΔQ^2 , Δx and $\Delta\beta$ denote the size of the bin. The results were obtained from the diffractive Monte Carlo.

Q^2_{centre}	x_{centre}	Q^2_{low}	Q^2_{high}	$\log(x_{\text{low}})$	$\log(x_{\text{high}})$	Method
8.5	0.00024	7.5	10.0	-3.75	-3.50	SE
8.5	0.00042	7.5	10.0	-3.50	-3.25	SE
12.0	0.00024	10.0	15.0	-3.75	-3.50	S
12.0	0.00042	10.0	15.0	-3.50	-3.25	SE
12.0	0.00075	10.0	15.0	-3.25	-3.00	SE
12.0	0.00133	10.0	15.0	-3.00	-2.75	SE
12.0	0.00237	10.0	15.0	-2.75	-2.50	SE
12.0	0.00421	10.0	15.0	-2.50	-2.25	S
25.0	0.00075	15.0	35.0	-3.25	-3.00	SE
25.0	0.00133	15.0	35.0	-3.00	-2.75	SE
25.0	0.00237	15.0	35.0	-2.75	-2.50	SE
25.0	0.00421	15.0	35.0	-2.50	-2.25	SE
25.0	0.00750	15.0	35.0	-2.25	-2.00	S
50.0	0.00133	35.0	70.0	-3.00	-2.75	SE
50.0	0.00237	35.0	70.0	-2.75	-2.50	SE
50.0	0.00421	35.0	70.0	-2.50	-2.25	SE
50.0	0.00750	35.0	70.0	-2.25	-2.00	SE
50.0	0.01330	35.0	70.0	-2.00	-1.75	S

Table 10.1: The bin centres and boundaries in x and Q^2 . The column ‘Method’ refers to which of the two kinematic variable reconstruction methods is used in that bin. ‘E’ is the electron method and ‘S’ is the sigma method. Q^2 values are in GeV^2 .

β_{centre}	β_{low}	β_{high}
0.065	0.03	0.10
0.175	0.10	0.25
0.375	0.25	0.50
0.650	0.50	0.80

Table 10.2: The bin centres and boundaries in β .

10.4 Monte Carlo Selection

Monte Carlos must be used in this analysis to estimate acceptances, backgrounds etc. It is, therefore, important that the Monte Carlos used describe the real data as closely as possible. Out of several available diffractive parameterisations a choice has been made of:

41%	RAPGAP hard gluon,
41%	RAPGAP hard quark,
8%	diffractive VMD.

As can be seen in figure 10.3 this mixture describes the control distributions very well. Of course this prescription will not match the true structure function exactly. Section 10.6 describes the procedure by which the systematic error on the measured structure function due to changes to the input Monte Carlo is calculated. This Monte Carlo has two limitations that must be accounted for separately in the measurement and systematic errors: there is no implementation of QED radiation or proton dissociation.

For non-diffractive background determination a Monte Carlo was used based on the CDM model with a structure function (MRSDH') obtained from a fit to the $F_2^P(x, Q^2)$ using 1993 H1 data [39]. This model has also been shown to describe energy flows in the acceptance region of the main calorimeter very well [40] and so would be expected to reproduce the background well. To assess the effect of a change in DIS model a model which does not describe the energy flows, MEPS (again with MRSDH'), is used [40].

10.5 Determination of $F_2^D(\beta, x_{\mathbb{P}}, Q^2)$

The Born cross section for a bin in Q^2 , x and β can be determined from the measured number of events in the bin, N , by the following equation:

$$\frac{d^3\sigma(x, Q^2, \beta)}{dx dQ^2 d\beta} = (N - N_{BAC}) \cdot \frac{1}{BVO} \cdot \frac{1}{ACC} \cdot \frac{1}{PDI} \cdot \frac{1}{\varepsilon} \cdot \frac{1}{L} \cdot \frac{1}{(1 + \delta)} \quad (10.10)$$

where:

- N_{BAC} — the total number of background events
- BVO — the corrected ‘volume’ of the bin in x - Q^2 - β space. It allows a conversion of the bin measurement to a value at a quoted point.

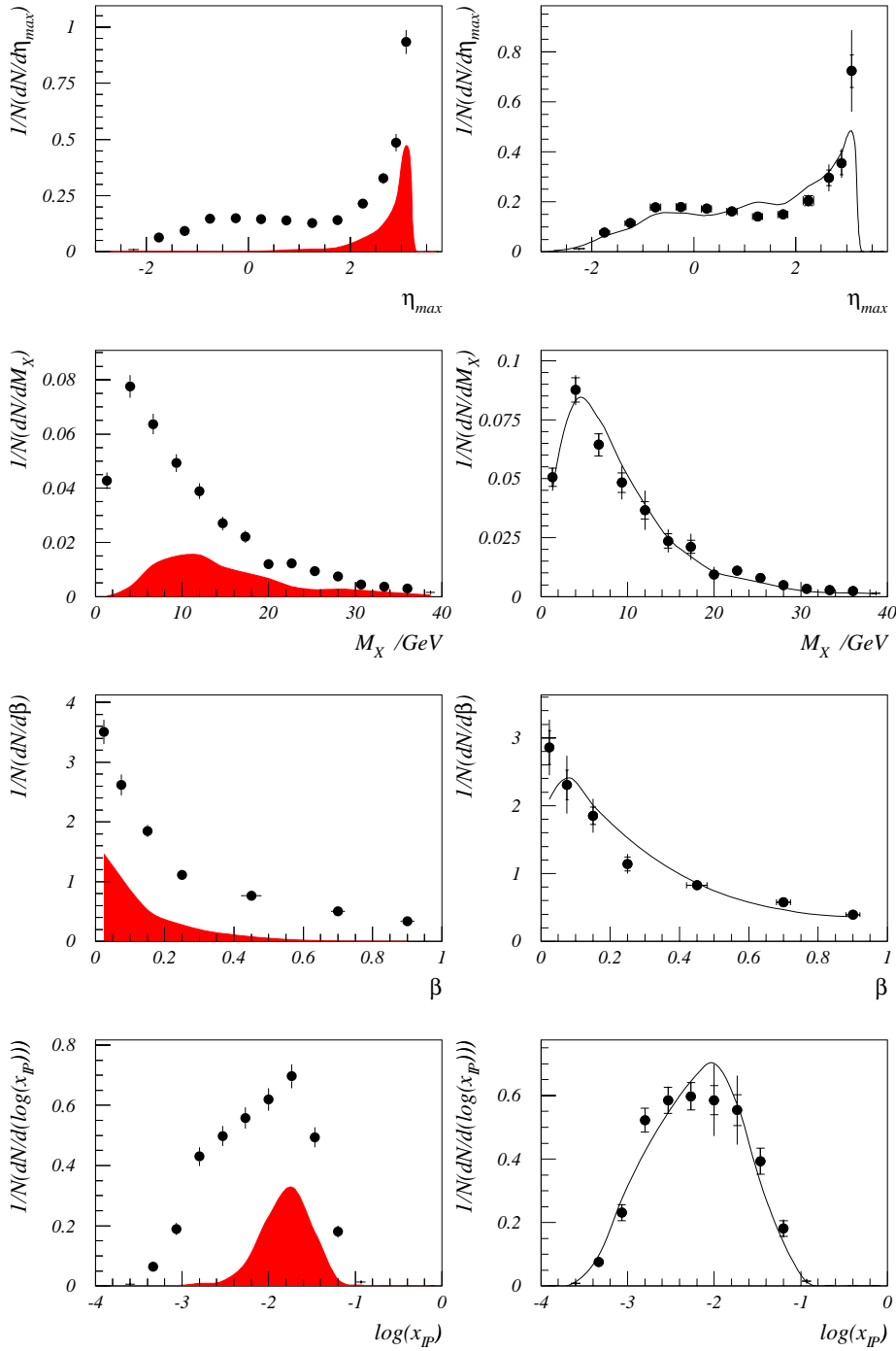


Figure 10.3: Comparison of the diffractive Monte Carlo with uncorrected data. Left is shown the signal obtained without background subtraction (closed circles) and the estimated standard DIS background (shaded). Right is shown the data with the DIS background subtracted (closed circles) and the diffractive Monte Carlo (solid line). The inner error bars represent the statistical error and outer error bars the statistical and the systematic arising from uncertainty in the background subtraction. All data was reconstructed with the sigma method.

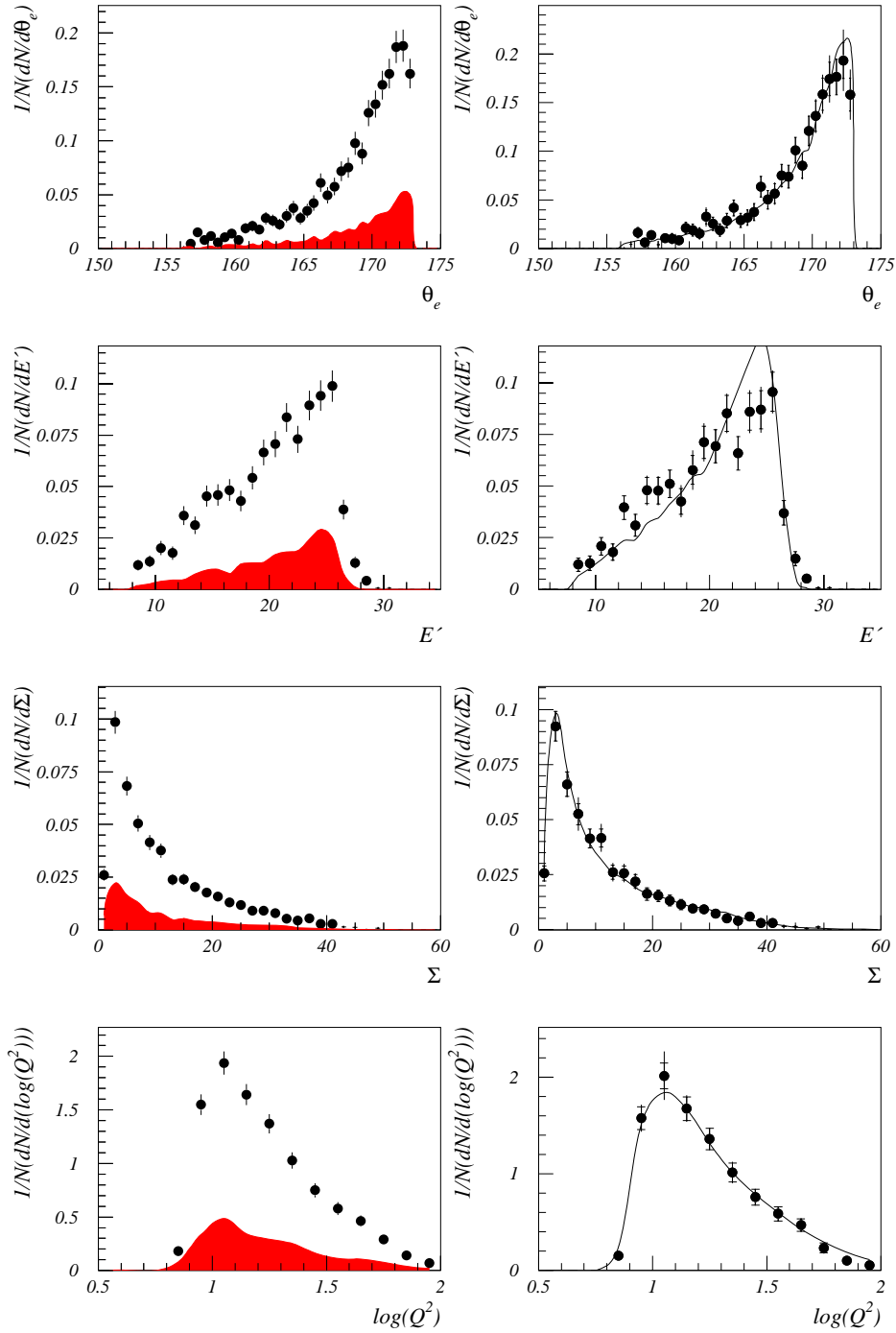


Figure 10.4: Comparison of Monte Carlo with uncorrected data continued. Q^2 is measured in GeV^2

- ACC — the smeared Monte Carlo acceptance correction, made to correct for detector losses and migration of events between bins.
- PDI — the proton dissociation correction, made to correct for events lost due to particles passing into the forward detectors as a result of proton dissociation.
- ε — trigger efficiency.
- L — the integrated luminosity.
- δ — the radiative correction, made to convert the measured radiative cross section into the Born cross section. The Born cross section is that that would be obtained if there were no QED radiation.

The remainder of this section explains how each of these quantities is determined.

10.5.1 N — Number of Diffractive Candidates

The first stage of event selection is a selection of a clean sample of DIS events using either the sigma or electron selections described in chapter 8. The diffractive events are picked out of the DIS selection using the cuts of FWDB (as described in section 9.5). This selection gives a reasonable acceptance and a low non diffractive background level. It cuts few proton dissociation events so the measured number of events can be corrected to the total (proton dissociation plus elastic) cross section.

10.5.2 N_{BAC} — Non Diffractive Background

The primary source of background is standard non diffractive DIS events. An estimate of this contribution is made using the CDM Monte Carlo with the number of events normalised to that found in data after DIS selection cuts and a further cut of $\eta_{max} > 3.0$ to suppress the number of diffractive events. The standard DIS Monte Carlo is then put through the same DIS and diffractive cuts (FWDB) as for the data and the number of events per bin recorded.

The other main sources of background are beam-gas and photoproduction with a faked electron cluster in the BEMC. The number of beam-gas events was estimated from the real data by examination of the electron and proton pilot bunches and that from photoproduction by Monte Carlo simulation. Both were found to be negligible (1 – 2%) when compared to the statistical errors on the measurement. Full details of this analysis can be found in [41].

10.5.3 ACC — Smeared Acceptance

The smeared acceptance is given by:

$$ACC = \frac{N_{rec}^{MC}}{N_{true}^{MC}}, \quad (10.11)$$

where N_{rec}^{MC} is the number of events reconstructed in the bin after all cuts and N_{true}^{MC} is the number of generated events in the bin after the kinematic cuts of equations 10.6-10.9 have been made. Data is taken entirely from the diffractive Monte Carlo. For a perfect detector ACC would take the value of 1. ACC takes into account event losses (i.e. where an event is not reconstructed as a diffractive DIS event at all) and smearing between bins (i.e. where an event is generated in one bin but is reconstructed in another).

10.5.4 PDI — Proton Dissociation Correction

The number of events lost due to proton dissociation was estimated from the data by comparing the total number of diffractive candidates (after background subtraction and a correction made for losses due to noise) obtained with the ETAM selection alone, N_E , and that obtained with the ETAM and FWDB together, $N_{E.F}$, so:

$$PDI = \frac{N_{E.F}}{N_E}. \quad (10.12)$$

Monte Carlos predict that there is only a very small chance of a particle from the dissociated proton reaching the LAC so ETAM has the same chance of selecting a proton dissociation event as an elastic proton event. The value obtained is:

$$PDI = 0.91 \pm 0.05, \quad (10.13)$$

where the systematic error mainly arises from uncertainty in the standard DIS background contamination. There is no experimental or theoretical evidence that PDI varies as a function of the kinematic variables.

10.5.5 BVO — Corrected Bin Volume

BVO is determined entirely from the diffractive Monte Carlo. It is defined as:

$$BVO = \frac{\int_{\text{bin}} \frac{d^3\sigma(\beta, x, Q^2)}{d\beta dx dQ^2} d\beta dx dQ^2}{\frac{d^3\sigma(\beta_c, x_c, Q_c^2)}{d\beta dx dQ^2}}, \quad (10.14)$$

where x_c , Q_c^2 , and β_c are the values at the quoted bin centre.

10.5.6 ε — Trigger Inefficiencies

The Monte Carlo used does not include any losses due to the acceptance of the H1 trigger. The efficiency of the trigger is estimated at 0.88 ± 0.06 , with extra losses of not more than 10 % for $\theta_e > 171.5^\circ$ and $E' < 10.6$ GeV. These extra losses do not change the value of the structure function at any measured point by more than 5 %. Further details of the calculation of the extra losses can be found in [41]

10.5.7 δ — Radiative Corrections

The radiative corrections were calculated using a recent version of the ARIADNE Monte Carlo [42], which includes diffractive event generation, with an interface to HERACLES [43] which generates the radiative events. The calculations were made only for the electron method of event selection, since the radiative corrections for the sigma method are estimated to be less than 3 % i.e. negligible when compared to the statistical errors on the measurement. The calculations were performed by [44].

10.6 Systematic Errors

The various contributions to the systematic error on each data point were estimated as follows:

- BAC — Uncertainty in non diffractive DIS background, found by taking the difference between the structure function obtained with N_{BAC} determined by CDM and MEPS Monte Carlos.
- ACB — Error in acceptance due to uncertainty in the β distribution of the input diffractive Monte Carlo. This is calculated by changing the ‘hardness’ of the Monte Carlo by an amount shown in figure 10.5.a. This is achieved by reweighting the Monte Carlo cross section with the function:

$$\left(\frac{1}{g} - g\right)\beta + g, \quad (10.15)$$

where g is 1 for the default, 0.5 for the harder distribution and 2 for the softer. ACB is taken as half the difference between the structure functions obtained with ACC calculated using the harder and softer input distributions. It should be noted that this error includes any uncertainty in the fraction of direct

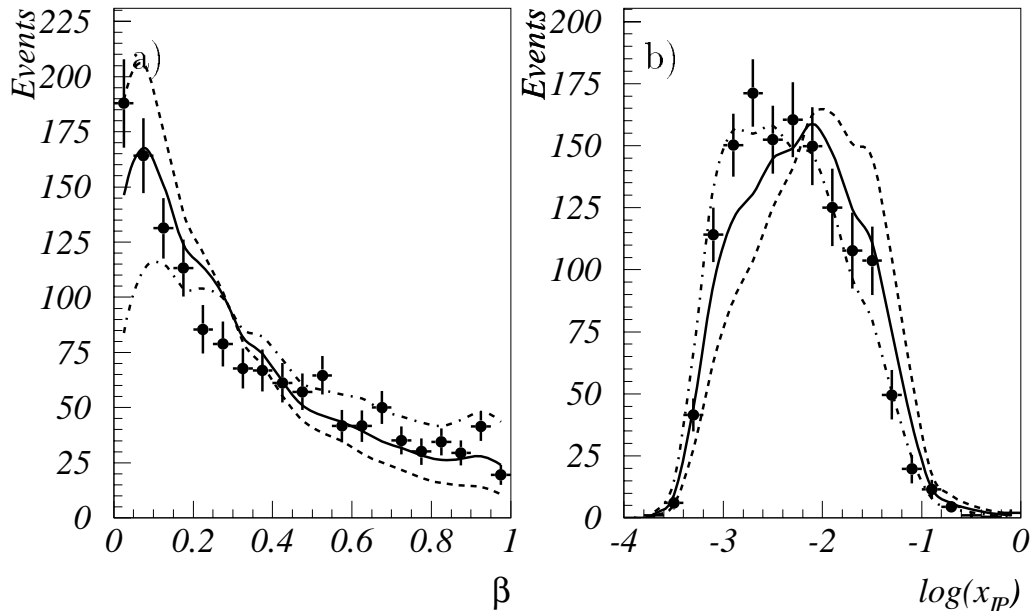


Figure 10.5: A comparison of the data (closed circles) with the diffractive Monte Carlo unweighted (solid line) and reweighted (dotted lines) to reflect the estimated uncertainty in a) the hardness of the β spectrum and b) the x_P dependence.

processes (VMD) in the data since the reweighting will change this fraction in the Monte Carlo by a factor of approximately 2.

- ACX — Error in acceptance due to uncertainty in the x_P distribution of the input diffractive Monte Carlo. This is calculated by changing the slope in the input Monte Carlo by an amount:

$$\frac{1}{x_P^{\pm 0.2}} \quad (10.16)$$

ACX is taken as half the difference between the structure functions obtained from each of the the slope changes.

- ACF — Error in acceptance correction due to uncertainty in the hard subprocesses of the production of the hadronic final state. The number of events estimated to be lost by the FWDB selection can vary depending on the model assumed for the hard subprocesses. ACF is taken as the difference in the obtained structure function if the input Monte Carlo were all gluon initiated or

all quark initiated:

$$ACF = \left| \frac{N_{FWDB}^G}{N^G} - \frac{N_{FWDB}^Q}{N^Q} \right| / \left(\frac{N_{FWDB}^Q}{N^Q} \right) \cdot F_2^D, \quad (10.17)$$

where (for RAPGAP hard gluon) N^G is the number of events per bin reconstructed with DIS cuts but no diffractive selection and N_{FWDB}^G is the number of events per bin reconstructed with DIS and FWDB cuts, and similar definitions for RAPGAP hard quark. This definition of ACF avoids any contributions due to bin smearing, which are accounted for in other systematic errors.

- ACR — Error in acceptance due to uncertainties of the amount of radiative smearing. The diffractive Monte Carlo used in the acceptance calculation does not have an implementation of QED radiation. Events with radiation will not necessarily be reconstructed in the correct bin and so result in a different acceptance correction. The error arising from the absence of radiative events in the Monte Carlo is calculated by comparing the difference in acceptance obtained from two standard DIS Monte Carlos generated with and without radiative events for each x - Q^2 bin. The error is then applied to each of the 4 bins that share the same x and Q^2 .
- ELA — Error due to the 10% energy scale uncertainty of the LAC. This is estimated by finding the fractional change in the number of reconstructed diffractive Monte Carlo events per bin before and after changing the energy scale assumed in the reconstruction.
- EBE — Error due to the 1.6% energy scale uncertainty of the BEMC. Determined in a similar way as for ELA.
- ETH — Error due to uncertainty in the measurement of θ_e of 2 mrad. Determined in a similar way as for ELA.
- ERA — Error due to uncertainty in the radiative correction. This is taken as the difference of the structure function calculated with and without the full radiative correction.
- BSB — Error in the corrected bin volume due to uncertainty in the β distribution. Estimated by taking the difference in the obtained structure function with BVO calculated using a hard quark distribution ($F_2^P \sim \beta(1 - \beta)$) and a flat distribution ($F_2^P \sim 1$) which seems to fit the data better, see figure 10.9.
- BSX — Error in the corrected bin volume due to uncertainty in the x_P slope. Estimated by taking the difference in the obtained structure function with BVO calculated using the Stregng parameterisation (equation 7.9) with $\varepsilon = 0.17$ and $\varepsilon = 0.35$.

- OVE — Overall normalisation uncertainty. Certain systematic affect all points data point equally. The estimated contributions are:
 - 5 % — Uncertainty in the measurement of luminosity,
 - 3 % — Uncertainty in losses due to detector noise,
 - 5 % — Uncertainty in PDI calculation.

10.7 The Diffractive Proton Structure Function

$F_2^D(\beta, x_P, Q^2)$ is shown in figure 10.6, plotted as a function of x_P at 16 different (Q^2, β) combinations for both the electron and sigma analyses. It was observed that in those bins where the acceptance was low a high proportion of points had greater than 100 % systematic error, indicating that with present understanding no useful measurement can be made for bins with low acceptance. For this reason all bins with $ACC < 0.2$ are not shown in figure 10.6 or included in subsequent plots or tables. Also removed from subsequent plots and tables are those points from the $\beta = 0.065, Q^2 = 50 \text{ GeV}^2$ bin. The level of statistics is so low that all points are consistent with zero and no useful structure function measurement can be made.

It can be seen from figure 10.6 that there is very good agreement between the electron and sigma methods. It was observed that in most bins the sigma method had a lower overall systematic error and it also covers a wider kinematic range. There was thus little gain in combining the results. Instead the final set of values (listed in tables 10.3 and 10.4) are those obtained solely from the sigma method.

Figure 10.7 shows a fit to the measured values of the form:

$$F_2^D(\beta, x_P, Q^2) = \frac{A(\beta, Q^2)}{x_P^n} \quad (10.18)$$

where A is allowed to vary as a function of β and Q^2 and n is constrained to be a constant for all β, Q^2 and x_P . This function gives reasonable χ^2 values for all β and Q^2 showing that within the errors F_2^D has the same x_P dependence for any β and Q^2 i.e. the data agree with the ansatz of factorisation. The result of the fit is:

$$n = 1.11 \pm 0.05 \pm 0.12, \quad (10.19)$$

A similar fit to the electron method selected data showed results in good agreement:

$$n = 1.27 \pm 0.07 \pm 0.19, \quad (10.20)$$

The systematic errors on n were estimated by making a remeasurement of the structure function after each of the possible changes described in section 10.6 was

performed and refitting. The total systematic error was found by summing in quadrature the differences between the slope obtained from each change and the value obtained without changes. The value of n obtained is in good agreement with the predictions made from the diffractive models (see section 7.7.1), indicating that the dominant mechanism for the production of the observed rapidity gaps is indeed diffraction.

Since the results show no deviation from factorisation it is possible to extract the pomeron structure function. The theoretical definitions of $F_2^{\mathbb{P}}$ given in section 7.7.1 are not used since they require an assumption of the normalisation of the flux factor. Instead the quantity $\tilde{F}_2^{\mathbb{P}}$ is defined such that:

$$\tilde{F}_2^{\mathbb{P}} = \int_{x_{\mathbb{P}}^{\text{low}}}^{x_{\mathbb{P}}^{\text{high}}} F_2^D(\beta, x_{\mathbb{P}}, Q^2) dx_{\mathbb{P}}, \quad (10.21)$$

so that:

$$\tilde{F}_2^{\mathbb{P}} = \frac{A(\beta, Q^2)}{n-1} \left\{ (x_{\mathbb{P}}^{\text{low}})^{-(n-1)} - (x_{\mathbb{P}}^{\text{high}})^{-(n-1)} \right\}, \quad (10.22)$$

if the structure function is assumed to follow the form of equation 10.18. $\tilde{F}_2^{\mathbb{P}}$ is equal to the theoretical definitions of $F_2^{\mathbb{P}}$ apart from a constant scale factor. The values used for the limits of the integration were chosen so that the $x_{\mathbb{P}}$ range was approximately the same as the range of the data points. The limits are:

$$x_{\mathbb{P}}^{\text{low}} = 10^{-4} \quad (10.23)$$

$$x_{\mathbb{P}}^{\text{high}} = 10^{-1} \quad (10.24)$$

$\tilde{F}_2^{\mathbb{P}}$ is shown plotted as a function of Q^2 in figure 10.8 and β in figure 10.9. The results are consistent with a flat Q^2 dependence i.e. are consistent with scaling and the assumption of a partonic content to the pomeron. The β dependence is flat within errors, but also consistent with a hard pomeron structure function with an indication of an enhancement at lower β . This enhancement could well be due the ‘sea’ produced by QCD pair production diagrams. It can be seen that the data clearly forces the soft pomeron structure function to be rejected.

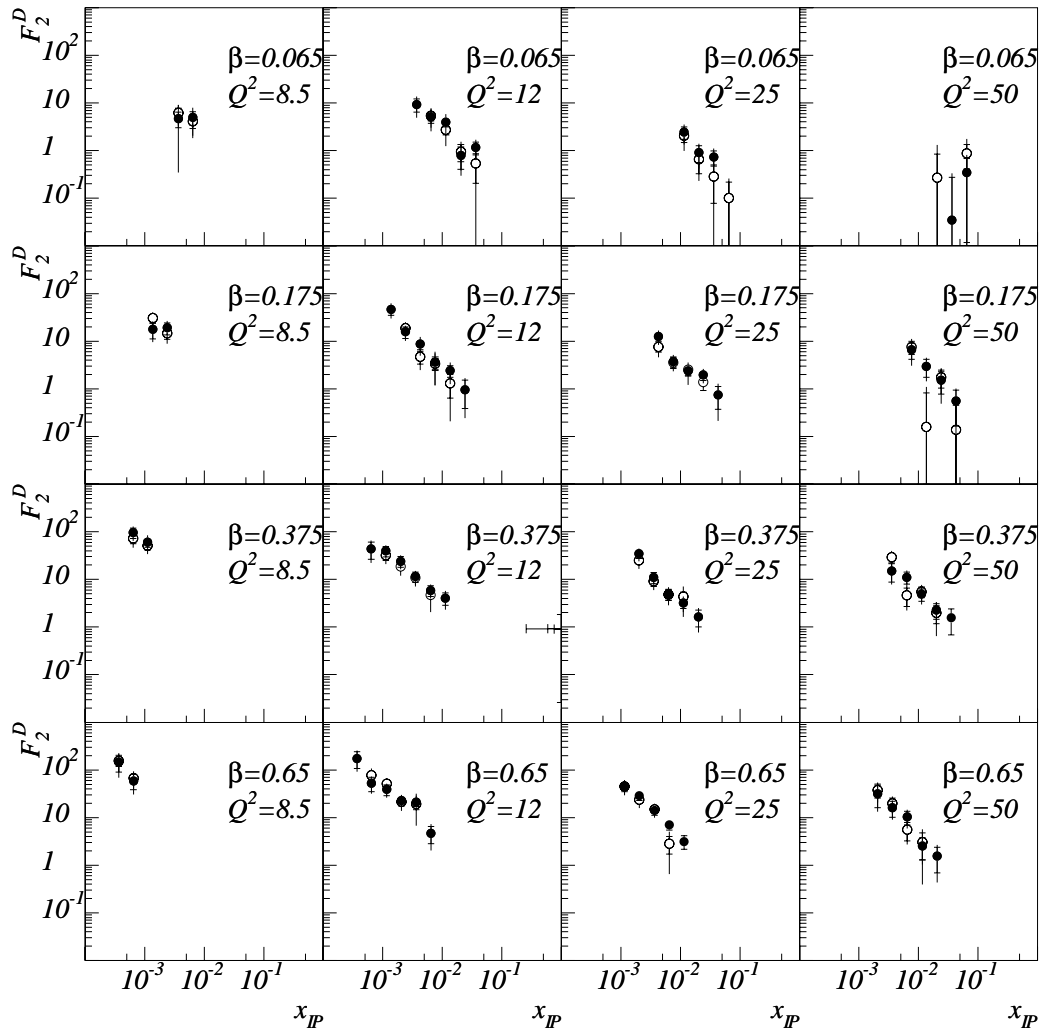


Figure 10.6: $F_2^D(\beta, x_P, Q^2)$ plotted as a function of x_P for various β and Q^2 values. Filled circles correspond to data selected using the sigma method. Open circles correspond to data selected using the electron method. Not included in the errors is an overall normalisation uncertainty of 8 %. Q^2 values are measured in GeV^2 .

Q^2	β	x	F_2^D	ST	SY	N	N_{BAC}	ACC
8.5	.065	.00024	4.72	1.69	4.03	10	1.20	.61
8.5	.065	.00042	5.00	1.59	2.45	18	4.70	.65
8.5	.175	.00024	17.75	6.54	4.92	8	.32	.49
8.5	.175	.00042	19.01	5.37	5.32	15	1.29	.61
8.5	.375	.00024	96.02	24.00	20.80	16	.00	.53
8.5	.375	.00042	60.71	13.74	18.13	21	.76	.78
8.5	.650	.00024	146.10	55.22	54.67	7	.00	.39
8.5	.650	.00042	59.28	20.96	19.81	8	.00	.82
12.0	.065	.00024	9.27	2.80	3.39	15	2.19	.61
12.0	.065	.00042	5.06	1.30	2.18	22	3.73	.60
12.0	.065	.00075	3.99	.87	1.68	37	8.99	.58
12.0	.065	.00133	.80	.39	.31	22	12.50	.51
12.0	.065	.00237	1.17	.35	.40	18	3.90	.29
12.0	.175	.00024	46.36	11.16	12.25	18	.37	.59
12.0	.175	.00042	15.65	4.33	3.44	17	2.08	.56
12.0	.175	.00075	8.66	2.06	3.07	21	1.72	.64
12.0	.175	.00133	3.60	1.06	2.16	24	7.30	.70
12.0	.175	.00237	2.40	.66	.93	29	9.41	.67
12.0	.175	.00421	.96	.57	.43	14	7.74	.46
12.0	.375	.00024	43.60	17.05	13.21	7	.24	.68
12.0	.375	.00042	39.25	9.78	7.75	17	.45	.70
12.0	.375	.00075	24.07	6.01	4.93	18	1.02	.57
12.0	.375	.00133	11.44	2.82	2.48	19	1.32	.65
12.0	.375	.00237	5.90	1.50	1.26	22	3.61	.73
12.0	.375	.00421	4.04	1.20	1.22	19	4.38	.71
12.0	.650	.00024	173.93	66.64	47.28	7	.09	.45
12.0	.650	.00042	52.69	17.37	11.53	10	.41	.76
12.0	.650	.00075	39.00	9.91	7.80	16	.26	.82
12.0	.650	.00133	22.79	5.27	5.11	21	1.18	.93
12.0	.650	.00237	21.30	4.21	5.99	28	1.22	.75
12.0	.650	.00421	4.69	1.87	1.91	9	1.46	.81

Table 10.3: $F_2^D(\beta, x_P, Q^2)$. ST is the statistical error, SY is the total systematic error, N is the number of events in the bin, N_{BAC} is the estimated number of background events in the bin, ACC is the smeared acceptance. Not included in the errors is an overall normalisation uncertainty of 8 %. Q^2 values are in GeV^2 .

Q^2	β	x	F_2^D	ST	SY	N	N_{BAC}	ACC
25.0	.065	.00075	2.43	.70	.82	30	10.92	.65
25.0	.065	.00133	.91	.35	.34	25	12.14	.57
25.0	.065	.00237	.73	.26	.26	20	7.28	.37
25.0	.065	.00421	.10	.12	.11	2	.76	.24
25.0	.175	.00075	12.47	2.47	3.38	31	2.87	.65
25.0	.175	.00133	3.72	.97	1.00	29	8.24	.78
25.0	.175	.00237	2.40	.56	1.06	36	10.12	.80
25.0	.175	.00421	1.95	.46	.47	37	11.16	.52
25.0	.175	.00750	.75	.37	.38	11	4.38	.31
25.0	.375	.00075	34.31	7.03	7.82	25	.60	.58
25.0	.375	.00133	11.01	2.81	1.79	21	3.06	.65
25.0	.375	.00237	4.91	1.23	1.33	25	5.04	.84
25.0	.375	.00421	3.20	.73	.88	34	8.35	.88
25.0	.375	.00750	1.63	.63	.59	20	8.49	.73
25.0	.650	.00075	45.51	10.29	10.65	20	.23	.90
25.0	.650	.00133	29.11	6.29	5.16	23	.82	.78
25.0	.650	.00237	14.05	2.92	2.53	26	1.45	.92
25.0	.650	.00421	6.99	1.53	1.62	27	3.28	.97
25.0	.650	.00750	3.15	1.01	1.53	14	2.29	.96
50.0	.175	.00133	6.57	2.42	2.53	11	2.01	.74
50.0	.175	.00237	2.96	1.21	.94	13	4.20	.67
50.0	.175	.00421	1.54	.75	.73	12	4.95	.52
50.0	.175	.00750	.55	.39	.27	5	1.82	.35
50.0	.375	.00133	15.08	6.23	3.75	7	.59	.64
50.0	.375	.00237	11.11	3.15	2.68	15	1.32	.77
50.0	.375	.00421	4.88	1.42	1.30	16	2.27	.89
50.0	.375	.00750	2.27	.82	.67	16	4.98	.81
50.0	.375	.01330	1.56	.87	.68	10	4.32	.38
50.0	.650	.00133	32.05	15.83	9.85	5	.47	.54
50.0	.650	.00237	16.03	5.84	3.75	8	.24	.77
50.0	.650	.00421	10.33	3.36	2.85	12	1.34	.83
50.0	.650	.00750	2.55	1.27	.82	7	1.71	.88
50.0	.650	.01330	1.54	.86	.70	8	2.91	.87

Table 10.4: $F_2^D(\beta, x_P, Q^2)$ continued.

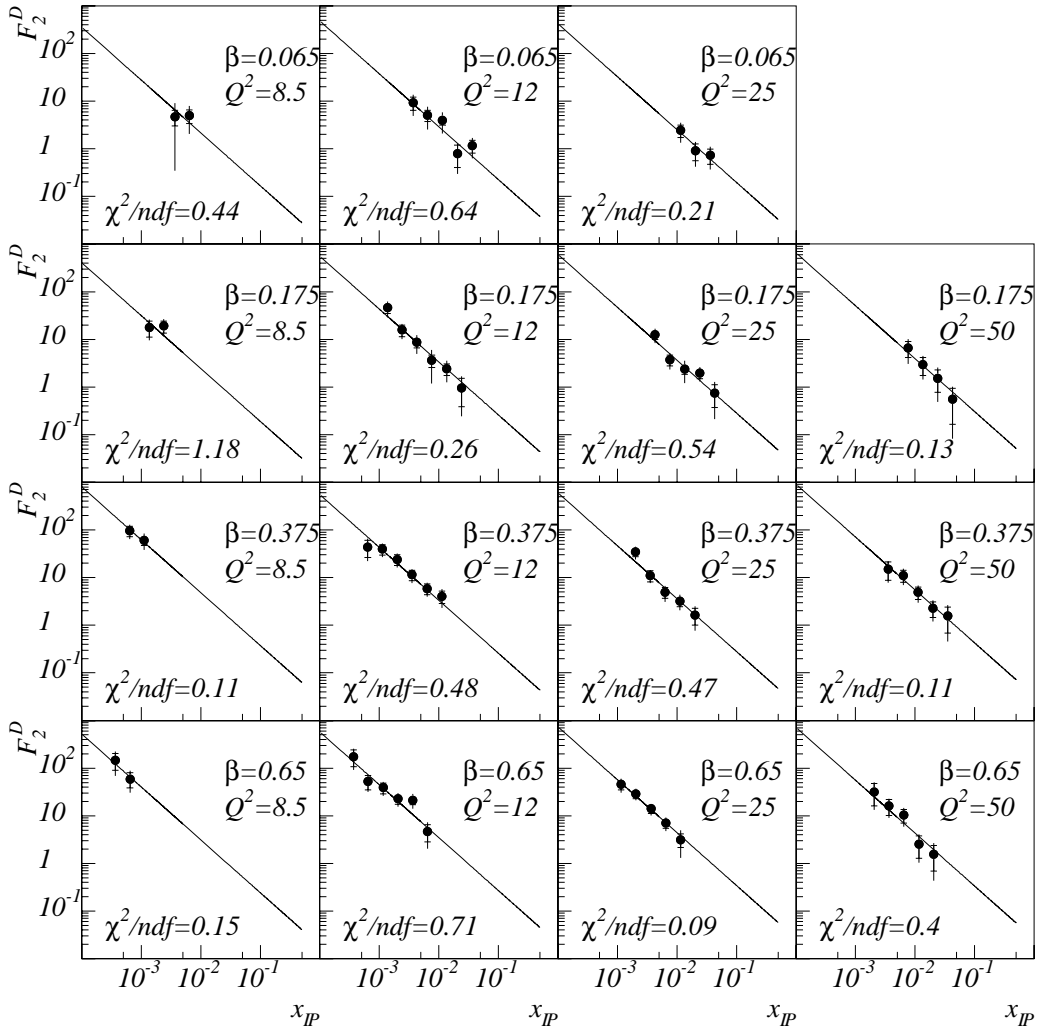


Figure 10.7: $F_2^D(\beta, x_P, Q^2)$ plotted as a function of x_P for various β and Q^2 values. Data is combined electron and sigma methods. Fit is to $A(\beta, Q^2)/(x_P)^{1.11}$. An additional overall normalisation uncertainty of 8 % is not included in the errors. Q^2 values are measured in GeV^2 .

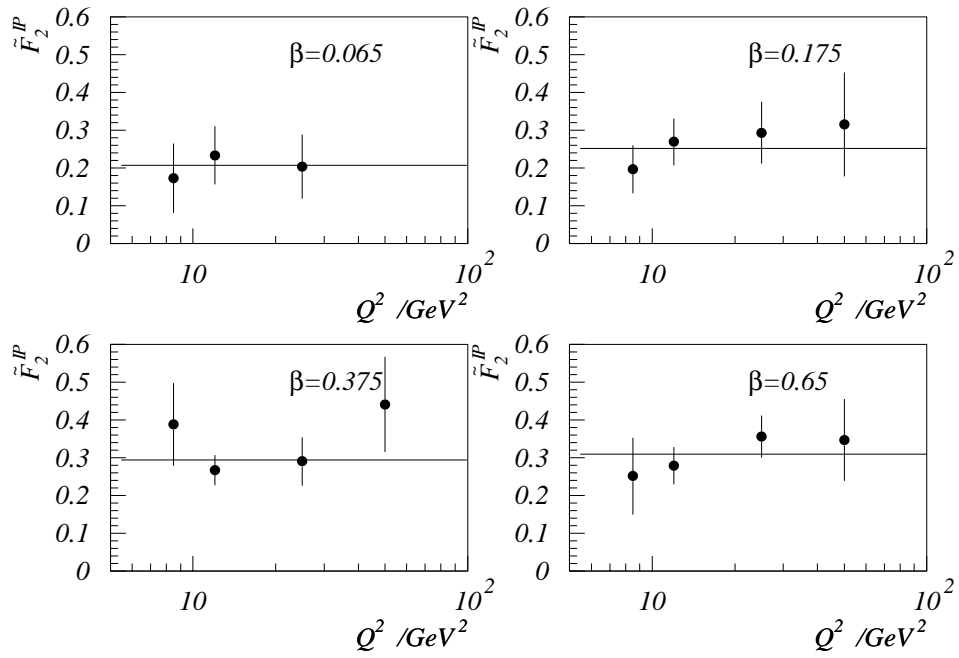


Figure 10.8: $\tilde{F}_2^P(\beta, Q^2)$ plotted as a function of Q^2 for various β values. The error bars represent the statistical and systematic errors added in quadrature. The solid line is a fit to a constant. Not included in the errors is an overall normalisation uncertainty of 8 %. The solid line is a fit to a constant.

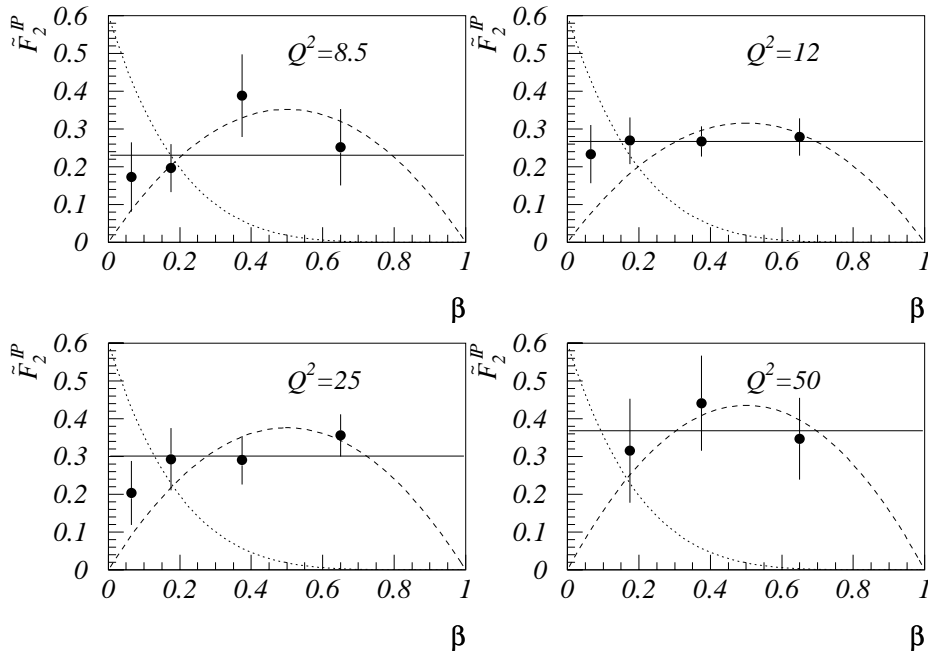


Figure 10.9: $\tilde{F}_2^{IP}(\beta, Q^2)$ plotted as a function of β for various Q^2 values. Not included in the errors is an overall normalisation uncertainty of 8 %. The solid line is a fit to a constant, the dashed line is a fit to a hard distribution ($B(Q^2)\beta(1-\beta)$) and the dotted line is a soft distribution ($0.6(1-\beta)^5$) with an arbitrary overall normalisation. Q^2 values are in GeV^2 .

Summary

It has been shown that the forward muon detector is well understood and capable of performing its required function at H1. Methods have been demonstrated that allow the drift velocity and T_0 of the chambers to be determined. Each quantity was also determined using an independent approach with results in good agreement. The drift chamber layers were aligned by a procedure based upon muons traversing the detector. The spacial resolutions of the chambers were measured and shown to be in good agreement with expectations. The momentum resolution was determined using a Monte Carlo simulation of the detector. Results were presented demonstrating that useful momentum measurement was possible up to 100 GeV.

A new diffractive event selection was introduced utilising information from the forward detectors and main calorimeter. This selection was shown to have a better acceptance and allowed a much greater accessible kinematic range than the previous selection used at H1. A comparison of Monte Carlo predictions of the performance of each subdetector with data was presented.

The new diffractive event selection was used to make a measurement of the diffractive proton structure function, $F_2^D(\beta, x, Q^2)$, over a range $0.00024 < x < 0.133$, $8.5 \text{ GeV}^2 < Q^2 < 50 \text{ GeV}^2$ and $0.065 < \beta < 0.65$. The data were consistent with an $x_{\mathbb{P}}$ dependence independent of Q^2 and β of $x_{\mathbb{P}}^{-1.11 \pm 0.05 \pm 0.12}$ i.e. the data show no deviation from the ansatz of factorisation. The data show an $F_2^{\mathbb{P}}(\beta, Q^2)$ dependence consistent with a hard $(\beta(1 - \beta))$ or flat β dependence. There is strong disagreement with the soft $((1 - \beta)^5)$ dependence.

Appendix A

Forward Detector Efficiencies

A.1 Introduction

This section outlines the method used to extract the efficiency for the rejection of standard DIS for the LAC and each of the forward detectors. The efficiencies can then be compared to Monte Carlo efficiencies and decisions made independently for each subdetector on its suitability as a diffractive tagger and how well it is described by the Monte Carlo. Since it is at present not possible to isolate a sample of DIS events containing no diffractive events a system has been devised which measures the fraction of diffractive events as well as the efficiencies.

A.2 Method

Consider a detector, labelled i , for which a signal is obtained for a fraction, E_i , of standard DIS events, D_i for diffractive DIS events and F_i for the total DIS sample. The detector is considered suitable as a diffractive veto only if:

$$E_i \gg D_i \tag{A.1}$$

If the fraction of standard DIS events in the total event sample is g then:

$$F_i = gE_i + (1 - g)D_i, \tag{A.2}$$

with the same result holding for another detector, j :

$$F_j = gE_j + (1 - g)D_j. \tag{A.3}$$

It should be noted that F_i is directly measurable from the data but E_i and D_i are not.

If it is assumed that the efficiencies of the two detectors are independent (assumption 1) then:

$$F_{ij} = gE_iE_j + (1-g)D_iD_j, \quad (\text{A.4})$$

where F_{ij} is the fraction of events where a signal is obtained in both detectors.

Consider a Monte Carlo made up of a mixture of standard DIS events and diffractive DIS events of proportions g^{MC} and $1-g^{MC}$:

$$F_i^{MC} = g^{MC} E_i^{MC} + (1-g^{MC})D_i^{MC} \quad (\text{A.5})$$

$$F_j^{MC} = g^{MC} E_j^{MC} + (1-g^{MC})D_j^{MC} \quad (\text{A.6})$$

$$F_{ij}^{MC} = g^{MC} E_i^{MC} E_j^{MC} + (1-g^{MC})D_i^{MC} D_j^{MC}, \quad (\text{A.7})$$

where the superscript MC indicates Monte Carlo data. Subtracting equations A.5, A.6 and A.7 from equations A.2, A.3 and A.4 respectively and assuming terms containing D are small and so can be ignored (assumption 2):

$$\Delta F_i \equiv F_i - F_i^{MC} = gE_i - g^{MC} E_i^{MC} \quad (\text{A.8})$$

$$\Delta F_j \equiv F_j - F_j^{MC} = gE_j - g^{MC} E_j^{MC} \quad (\text{A.9})$$

$$\Delta F_{ij} \equiv F_{ij} - F_{ij}^{MC} = gE_iE_j - g^{MC} E_i^{MC} E_j^{MC} \quad (\text{A.10})$$

Now we have 3 equations with three unknowns E_i , E_j and g (F s are measured in the data and all Monte Carlo quantities are known):

$$E_i = \frac{\Delta F_{ij} + g^{MC} E_i^{MC} E_j^{MC}}{\Delta F_j + g^{MC} E_j^{MC}} \quad (\text{A.11})$$

$$(\text{A.12})$$

$$E_j = \frac{\Delta F_{ij} + g^{MC} E_i^{MC} E_j^{MC}}{\Delta F_i + g^{MC} E_i^{MC}} \quad (\text{A.13})$$

$$(\text{A.14})$$

$$g = \frac{(\Delta F_i + g^{MC} E_i^{MC})}{E_i} \quad (\text{A.15})$$

Thus if the assumptions made are valid then this method makes it possible to extract the efficiencies of the two detectors and the fraction of standard DIS events from the data independently of the Monte Carlo efficiencies or the assumed event fraction. If the number of subdetectors investigated is increased the set of equations becomes over constrained: for three subdetectors we get 6 equations with four unknowns, for four subdetectors 10 equations with 5 unknowns and for five subdetectors (the actual case) we get 15 equations with 6 unknowns. It is thus possible to cross check the results obtained.

The assumptions made in the above derivation might seem too simplistic. It would seem obvious, for example, that an event in which a large amount of energy was deposited in the forward LAC would have a much larger chance of also depositing energy in the PLUG than the assumption of independent efficiencies would imply. The problem is dealt with by the subtraction of the corresponding Monte Carlo quantities. If equation A.4 were upgraded by the introduction of extra correlation terms then equation A.7 must also be upgraded. By making the subtraction to produce equation A.10 it would be expected that most of the correlation terms cancel. The same argument is used to justify assumption 2. If the diffractive terms are non negligible for the data equation then they will be very nearly cancelled by the Monte Carlo subtraction. The cross check provides further evidence that the assumptions are valid.

A.3 Results

The data were selected using the DIS cuts described in section 8.4 for the sigma method. There was no anti-selection of diffractive events. The efficiencies and standard DIS fraction were measured using a variety of input Monte Carlos and a range of possible input standard DIS fractions (g^{MC}). The results are shown in table A.1. Each of the quantities shown for real data is the mean of all possible measurements that could be made from the set of over constrained equations. The quoted error on each measured quantity is the r.m.s spread of all the possible measurements and not the error on the mean. The error thus includes the statistical and systematic contributions. Also included in the table are the results obtained by rescaling the PLUG energy in the Monte Carlo by 0.6 and rescaling the LAC energy by 0.75.

Model	CDM	MEPS	CDM	CDM	CDM	CDM	MEPS	CDM
SIM	3.03	3.03	3.01	3.03	3.03	3.03	3.03	3.03
Special						PLUG Rescale	PLUG Rescale	LAC Rescale
g^{MC}	91	91	91	80	100	91	91	91
g	91 ± 2	91 ± 2	90 ± 1	88 ± 3	94 ± 2	—	—	—
E_f^{MC}	79	77	84	79	79	—	—	—
E_f	76 ± 2	77 ± 2	78 ± 1	78 ± 2	75 ± 2	—	—	—
E_p^{MC}	83	78	82	83	83	79	73	—
E_p	80 ± 1	80 ± 1	80 ± 1	81 ± 2	79 ± 1	80 ± 1	80 ± 1	—
E_l^{MC}	89	81	88	89	89	—	—	87
E_l	84 ± 1	84 ± 1	84 ± 1	85 ± 1	84 ± 1	—	—	84 ± 1
E_i^{MC}	70	66	66	70	70	—	—	—
E_i	80 ± 2	80 ± 2	82 ± 1	82 ± 3	78 ± 2	—	—	—
E_t^{MC}	60	63	64	60	60	—	—	—
E_t	48 ± 1	48 ± 1	49 ± 2	49 ± 1	47 ± 1	—	—	—

Table A.1: Efficiencies of the forward detectors. Subscript f refers to the FMD; subscript p refers to the PLUG; subscript l refers to the LAC, subscript i refers to the IRON, subscript t refers to the PTAG. Quantities measured for real data are shown with no superscript. Quantities obtained from the Monte Carlos are shown with superscript MC .

References

- [1] H1 Collaboration, Nucl. Phys. B429, p477 (1994).
- [2] W. Buchmüller, G. Ingelman, *Proc. of the HERA Workshop*, Vol.1–3 (1992).
- [3] H1 Collaboration, Phys. Lett. B324, p241 (1994).
- [4] F. Halzen, A. Martin, *Quarks and Leptons: An introductory Course in Modern Particle Physics*, John Wiley & sons Ltd. (1984).
- [5] W. Krasny et al., in *Proc. of the HERA Workshop*, Vol.2, p787 (1991).
- [6] H1 Collaboration, Nucl. Phys. B407, p515 (1993).
- [7] J. Blümlein, M. Klein, in *Proc. of the HERA Workshop*, Vol.1, p101 (1991).
- [8] H. Jung et al., in *Proc. of the HERA Workshop*, Vol.2, p712 (1991).
- [9] H1 Collaboration, *The H1 Detector* DESY preprint. DESY 93-103, Hamburg (1993).
- [10] C. Hilton, *Thesis: Forward Muon Detection in H1 and Hadronic Energy Flow in Deep Inelastic Scattering*, University of Manchester (1993).
- [11] A. Mehta, *Diploma: Investigation of the Drift Velocity of the Forward Muon Drift Chambers of the H1 Detector*, University of Manchester (1992).
- [12] C. Hilton, *Diploma: Investigations Concerning the Forward Muon Drift Chambers*, University of Manchester (1991).
- [13] J.P. Sutton, *Diploma: The Drift Distance Resolution of the Drift Chambers Used in the H1 Forward Muon Spectrometer*, University of Manchester (1990).
- [14] *MIT8 bank*, H1 database (1994).
- [15] I.P. Duerdoth, *Mopal2: the program used to model the OPAL muon chambers*, University of Manchester.
- [16] *M0AC bank*, H1 database (1994).

- [17] K. Stephens, *Private Communication*.
- [18] P. Biddulph et al. *Internal report: Measurements made on the Forward Muon System to Determine Relative z-positions of Octants*, DESY (1994).
- [19] J.P. Sutton, *Thesis: The H1 Forward Muon Spectrometer*, University of Manchester (1993).
- [20] P. Newman *Mid Term report: First Experiences with the Forward Muon Trigger* Birmingham University (1994).
- [21] R. Barlow, *Statistics* John Wiley & sons Ltd. (1989).
- [22] R. Omnès, *Introduction to Particle Physics* Wiley-interscience (1971).
- [23] G. Ingelman, K. Janson-Prytz *in Proc. of the HERA Workshop*, Vol. 1, p233 (1991).
- [24] E.L. Berger, J.C. Collins, D.E. Soper, G. Sterman, *Nucl. Phys.* B286, p704 (1987).
- [25] K.H. Streng, *in Proc. of the Hera Workshop* Vol. 1 p. 365 (1987).
- [26] G. Ingelman, P.E. Schlein, *Phys. Lett.* B152, p256 (1985).
- [27] A. Donnachie, P.V. Landshoff, *in Proc. of the Hera Workshop* Vol. 1 p351 (1987).
- [28] N.N Nikolaev, B.G. Zakharov, *Zh. Eksp. Teor. Fiz.* 105, p1117 (1994).
- [29] B. List, *Diplomarbeit: Diffraktive J/ψ -Production in Elektron-Proton-Stößen am Speicherring HERA*, H1 note H1-10/93-319 DESY (1993).
- [30] H. Jung, *Preprint: Hard Diffractive Scattering in High Energy ep collisions and the Monte Carlo Generator RAPGAP*, 93-182 DESY (1993).
- [31] L. Lönnblad, *in Proc. of the HERA Workshop*, Vol. 3, p. 1440 (1991).
- [32] T. Sjöstrand, *Phythia 5.6 and JETSET 7.3*, CERN-TH-6488/92 (1992).
- [33] S. Bentvelsen et al. *in Proc. of the HERA Workshop*, Vol.1, p23 (1991).
- [34] A. DeRoeck et al., *H1 note: Analysis II of the 1992 Data of the Structure Function $F_2(x, Q^2)$* , H1-12/93-332 (1993).
- [35] U. Bassler et al., *H1 note: Progress on Kinematic Variable Reconstruction. Consequenses for D.I.S Physics Analysis at low x*, H1-13/93-274 (1993).
- [36] ZEUS Collaboration, *Phys. Lett.* B315, p481 (1993).

- [37] L. Lönnblad, *Computer Phys. Comm.* 71 p15 (1992).
- [38] G. Ingelman, *in Proc. of the HERA Workshop*, Vol. 3, p1366 (1991).
- [39] H1 collaboration *Fit to data presented at the International Conference on High Energy Physics (Rochester Series)*, Glasgow (1994).
- [40] H1 collaboration, *Z. Phys.* C63 p77 (1994).
- [41] J.P. Phillips *Thesis: The Deep Inelastic Structure of Diffraction*, University of Manchester (1994).
- [42] L. Lönnblad, *Talk presented at the School for Deep Inelastic Scattering DESY* (1994).
- [43] A. Kwiatkowski et al., *in Proc. of the HERA Workshop*, Vol. 3, p1294 (1991).
- [44] H. Jung, *private communication*.

Acknowledgements

I would like to thank the many people who have greatly helped with the production of this thesis.

My supervisor, Mike Ibbotson, has supported me throughout my postgraduate studies. He has allowed me the freedom to pursue my own aims but always given guidance and encouragement. I do not think I could have had a better supervisor.

Without the aid of the members of the 'Forward muon team', Phill Biddulph, Chris Hilton, Paul Sutton, Lee West, Joe Foster, Paul Newman, Gareth Noyes and others my task would have been impossibly difficult. I am indebted to the work they did prior to my own and to their assistance to me.

The diffractive working group has been both open and friendly. I feel privileged to be working in a group of such clever and knowledgeable people. Particular thanks go to Julian Phillips for imparting some of his immense knowledge to me and help with the difficult bits of the structure function measurement, Professor John Dainton for his good ideas (some of which do actually turn out to be fruitful) and Hannes Jung for his clear explanations of difficult theory.

I must also thank the members of the H1 collaboration and all the other people at DESY and Manchester I have had the good fortune to meet.